

See discussions, stats, and author profiles for this publication at: <https://www.researchgate.net/publication/331562177>

The Coordination Dynamics of Multiple Agents

Thesis · December 2018

DOI: 10.13140/RG.2.2.23571.12320

CITATIONS

0

READS

40

1 author:



Mengsen Zhang

Florida Atlantic University

10 PUBLICATIONS 11 CITATIONS

SEE PROFILE

Some of the authors of this publication are also working on these related projects:



Coordination Dynamics: Bidirectional Coupling of Bodies, Brains, Babies and Machines [View project](#)



Multiscale Neuroscience: from Biological networks to Social interaction [View project](#)

THE COORDINATION DYNAMICS OF MULTIPLE AGENTS

by

Mengsen Zhang

A Dissertation Submitted to the Faculty of
The Charles E. Schmidt College of Science
in Partial Fulfillment of the Requirements for the Degree of
Doctor of Philosophy

Florida Atlantic University

Boca Raton, FL

December 2018

ProQuest Number: 10979968

All rights reserved

INFORMATION TO ALL USERS

The quality of this reproduction is dependent upon the quality of the copy submitted.

In the unlikely event that the author did not send a complete manuscript and there are missing pages, these will be noted. Also, if material had to be removed, a note will indicate the deletion.



ProQuest 10979968

Published by ProQuest LLC (2019). Copyright of the Dissertation is held by the Author.

All rights reserved.

This work is protected against unauthorized copying under Title 17, United States Code
Microform Edition © ProQuest LLC.

ProQuest LLC.
789 East Eisenhower Parkway
P.O. Box 1346
Ann Arbor, MI 48106 – 1346

Copyright 2018 by Mengsen Zhang

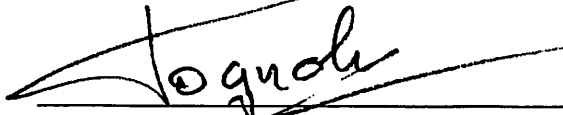
THE COORDINATION DYNAMICS OF MULTIPLE AGENTS

by

Mengsen Zhang

This dissertation was prepared under the direction of the candidate's dissertation co-advisors, Dr. Emmanuelle Tognoli and Dr. J. A. Scott Kelso, Center for Complex Systems and Brain Sciences, and has been approved by the members of her supervisory committee. It was submitted to the faculty of the Charles E. Schmidt College of Science and was accepted in partial fulfillment of the requirements for the degree of Doctor of Philosophy.

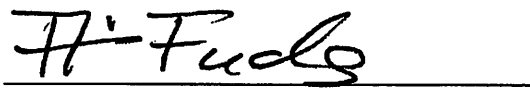
SUPERVISORY COMMITTEE:



Emmanuelle Tognoli, Ph.D.
Dissertation Co-Advisor



J. A. Scott Kelso, Ph.D.
Dissertation Co-Advisor



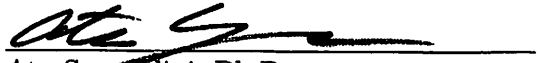
Armin Fuchs, Ph.D.



Christopher Beetle, Ph.D.



Steven Bressler, Ph.D.
Interim Director, Center for Complex
Systems and Brain Sciences



Ata Sarajedini, Ph.D.
Dean, The Charles E. Schmidt College of
Science



Khaled Sobhan, Ph.D.
Interim Dean, Graduate College

October 12, 2018
Date

ACKNOWLEDGEMENTS

I must thank my dear advisors, Drs. Emmanuelle Tognoli and J. A. Scott Kelso, for years of rigorous and broad scientific training, as well as personal guidance and conversations on philosophy, whiskey, and occasionally coffee roasting. I want to thank Dr. Armin Fuchs for being a great teacher of Physics, who reignited my interest in Physics and Mathematics, and Dr. Christopher Beetle for guiding me through my modeling work and taught me enough Differential Geometry to make it through the first few chapters of René Thom’s “Structural Stability and Morphogenesis”. In addition to members of my dissertation committee, I want to thank Drs. William Kalies and Erik Lundberg for providing feedback on part of this dissertation, and Dr. Roxana Stefanescu for assisting during the data collection. I am forever in debt to innumerable professors from the Center for Complex Systems and Brain Sciences, Department of Mathematics, Department of Physics, Department of Psychology, College of Medicine and College of Engineering for imparting your knowledge, and providing me with necessary technical skills and intellectual stimulations for completing this dissertation. As the Chinese saying goes, “a teacher for one day is a parent for life”. Speaking of which, I must also thank my parents who have been the most important teachers in my life and have supported me with unconditional love. I want to thank all my agonists and antagonists over the years, who are all part what I have become today. Last but not least, research presented in this dissertation was supported by the National Institute of Mental Health (MH080838). Travel supports were received from Florida Atlantic University Brain Institute, and National Science Foundation (ID: 1543122; PI: Dr. Stephanie Cacioppo).

ABSTRACT

Author: Mengsen Zhang
Title: The Coordination Dynamics of Multiple Agents
Institution: Florida Atlantic University
Dissertation Co-Advisors: Dr. Emmanuelle Tognoli
Dr. J. A. Scott Kelso
Degree: Doctor of Philosophy
Year: 2018

A fundamental question in Complexity Science is how numerous dynamic processes coordinate with each other on multiple levels of description to form a complex whole – a multiscale coordinative structure (e.g. a community of interacting people, organs, cells, molecules etc.). This dissertation includes a series of empirical, theoretical and methodological studies of rhythmic coordination between multiple agents to uncover dynamic principles underlying multiscale coordinative structures. First, a new experimental paradigm was developed for studying coordination at multiple levels of description in intermediate-sized ($N = 8$) ensembles of humans. Based on this paradigm, coordination dynamics in 15 ensembles was examined experimentally, where the diversity of subjects movement frequency was manipulated to induce different grouping behavior. Phase coordination between subjects was found to be metastable with inphase and antiphase tendencies. Higher frequency diversity led to segregation between frequency groups, reduced intragroup coordination, and dispersion of dyadic phase relations (i.e. relations at different levels of description). Subsequently, a model was developed, successfully capturing these observations. The model reconciles the Kuramoto and the extended Haken-Kelso-Bunz model (for large-

and small-scale coordination respectively) by adding the second-order coupling from the latter to the former. The second order coupling is indispensable in capturing experimental observations and connects behavioral complexity (i.e. multistability) of coordinative structures across scales. Both the experimental and theoretical studies revealed multiagent metastable coordination as a powerful mechanism for generating complex spatiotemporal patterns. Coexistence of multiple phase relations gives rise to many topologically distinct metastable patterns with different degrees of complexity. Finally, a new data-analytic tool was developed to quantify complex metastable patterns based on their topological features. The recurrence of topological features revealed important structures and transitions in high-dimensional dynamic patterns that eluded its non-topological counterparts. Taken together, the work has paved the way for a deeper understanding of multiscale coordinative structures.

*In memory of Dr. Raymond Paternoster, whose lectures and mentorship nudged me
into the basin of attraction of Complexity Science.*

THE COORDINATION DYNAMICS OF MULTIPLE AGENTS

List of Figures	xi
1 Introduction	1
1.1 Complex systems and multiscale structures	2
1.2 Large-scale coordination.....	4
1.3 Small-scale coordination.....	6
1.4 Mid-scale coordination	9
2 The Human Firefly experiment	11
2.1 Introduction	11
2.2 Results.....	13
2.2.1 Spontaneous phase coordination and spatiotemporal metastability	14
2.2.2 Dominant patterns of coordination.....	17
2.2.3 Segregation and integration of groups: critical diversity.....	21
2.2.4 Segregation and transitions of spatial order	23
2.3 Disucssion	26
2.3.1 Integration and segregation in a diverse group	26
2.3.2 The patterns of coordination	28
2.4 Conclusions.....	30
2.5 Materials and Methods	31
2.5.1 Participants	31
2.5.2 Experimental setup.....	31
2.5.3 Procedures	33

2.5.4	Statistical analyses	34
3	A cross-scale model of coordination dynamics.....	36
3.1	Introduction	36
3.2	Results.....	38
3.2.1	Human coordination at intermediate scales.....	38
3.2.2	A minimal experiment-based model	43
3.2.3	Weak coupling captures human behavior	44
3.2.4	The necessity of second-order coupling	47
3.2.5	The effect of non-uniform coupling.....	48
3.2.6	Metastable coordination between more than two agents.....	50
3.3	Discussion	58
3.4	Materials and Methods	61
3.4.1	Methods of the human experiment	61
3.4.2	Estimating the distribution of natural frequencies	62
3.4.3	Phase-locking value and level of integration	63
3.4.4	Method of simulation.....	65
4	Topological analysis of multiagent metastable coordination.....	66
4.1	Examples of coordination dynamics	67
4.2	Method of topological analysis.....	71
4.2.1	Coordination patterns as point clouds	71
4.2.2	Multiscale topological portraits and their dynamics	74
4.3	Results.....	80
4.4	Discussion	86
5	Toward understanding multiscale coordinative structures	92
Appendices.....		98
A	Supplementary information for the human experiment	99

A.1	Preprocessing of recorded signals	99
A.2	Multivariate analysis of variance (MANOVA)	100
A.3	Linear regressions and critical frequency identification	100
A.4	Distributional comparison.....	101
A.5	Long time-scale behavior in human coordination	102
B	Supplementary information for the model	103
B.1	Choosing the appropriate coupling strength	103
B.2	Empirical distribution of tapping frequency around metronome frequency	105
B.3	Examples of dynamics with intergroup coupling removed	107
B.4	Effect of reduced intragroup variability	109
B.5	Random coupling	110
B.6	Intergroup relation without second order coupling	111
B.7	Dynamics and stability of relative phases.....	114
B.8	Additional triadic dynamics	117
B.9	Additional triadic metastable patterns.....	119
	Bibliography	123

LIST OF FIGURES

2.1	Coordination dynamics of phase relations among multiple agents.....	16
2.2	Aggregate distributions of phase relations.	19
2.3	Multifrequency coordination.	21
2.4	Diversity parametrically controls integration segregation of groups within ensembles.	22
2.5	Frequency diversity contributes to spatial organization and reorganization.	25
2.6	Experimental Setup.	33
3.1	Experimental setup for multiagent coordination.....	38
3.2	Examples of frequency dynamics and aggregated relative phase distributions for three diversity conditions.	40
3.3	Intergroup relations and average inter/intragroup coordination.	42
3.4	Examples of frequency dynamics and aggregated relative phase distributions for simulated data.....	46
3.5	The effect of non-uniform coupling on coordination dynamics.....	50
3.6	Basic forms of triadic metastable coordination.	53
3.7	Extended forms of triadic metastable coordination.	56
3.8	An example of eight-agent metastable coordination.	57
4.1	An example of triadic coordination dynamics.....	68
4.2	An example of eight-agent coordination dynamics.	69
4.3	Recurrence plots of relative phase dynamics.	70
4.4	Decomposition of absolute phase dynamics.	72
4.5	A letter B made up of many A's.....	75
4.6	Simplices and a simplicial complex.	75

4.7	Persistence of topological features.	77
4.8	Recurrence plots of topological features versus states.	82
4.9	Breaking down the frequency, relative phase and topological dynamics of the eight-agent coordination.....	85
A.1	Multiagent coordination exhibits slow dynamics.....	102
B.1	The effect of diversity and coupling strength on the level of integration between groups.....	104
B.2	Distribution of human movement frequency around metronome fre- quencies and its estimation.....	106
B.3	Intragroup dynamics without intergroup coupling	108
B.4	Dynamics of intragroup phase-locking value (PLV) with and without intergroup coupling	109
B.5	Intragroup and intergroup phase-locking for simulated data with iden- tical natural frequency within groups.....	110
B.6	Level of integration between groups by δf and a , with $b = 0$	112
B.7	Intragroup, intergroup coordination and the relationship between them for $a = 0.154$ and $b = 0$	113
B.8	Simulated triadic coordination as a pair of relative phases.	118
B.9	Additional examples of simulated triadic metastability.	120
B.10	Sequence production in triadic metastable coordination.	121

CHAPTER 1

INTRODUCTION

How multiple interacting components generate complex behavior at multiple levels of description is one of the most fundamental problems of Complexity Science. The present work probes for general principles of multiagent coordination dynamics in complex systems, by means of experimental investigation of rhythmic coordination between multiple people (Chapter 2), theoretical modeling of these experimental data (Chapters 3) and developing a topology-based method for characterizing complex dynamic patterns (Chapter 4). While preexisting studies primarily focused on systems of very many or only a few components (large- vs. small-scale), the present analyses are grounded on intermediate-sized ensembles (mid-scale), which are large enough to be examined on multiple levels of description and small enough to yield to systematic experimental manipulations. In the following chapters, we show how the study of mid-scale coordination connects phenomena and theories of coordination dynamics across scales.

Specific backgrounds for individual studies are supplied in their respective chapters (Chapter 2-4), each of which can be read as a stand-alone piece. The present chapter provides a general context and motivation. We first clarify what kind of complex systems we are talking about (as a colleague once said “1000 Complex System scientists have 1000^α definitions of Complexity, with $\alpha > 1$ ”) and what kind of principles the present work aims to, ultimately, provide a window into (Section 1.1). We then review key phenomena and theories of large- (Section 1.2) and small-scale (Section 1.3) coordination pertinent to the present work. Finally, we explain why the study of mid-scale coordination is necessary and what we aim to accomplish with it.

1.1 COMPLEX SYSTEMS AND MULTISCALE STRUCTURES

Living animals are constantly on the move. It is one of the most characteristic things about them. Often we can see them running about, breathing, catching food and eating it, and so on. If we look closer we find that an animal is made up of different organs, and in all of them there is something going on all the time. On an even smaller scale, the organs are built out of cells, little lumps of living matter, each containing a special kernel or *nucleus*. And each cell is always full of activity. [...] there are incessant chemical actions and reactions.

In a living organism these changes are not isolated but are adjusted to one another so that the right operations are carried out to produce the right quantities of the various products. It is because we are so impressed at the way in which all the separate processes work together harmoniously that we call animals “organisms”. [...] If there is a “secret of life”, it is here we must look for it, among the causes which bring about the arrangement of innumerable separate processes into a single harmonious living organism.

– C. H. Waddington [1]

These two paragraphs summarize nicely all central characteristics of the type of complex systems relevant to our inquiry. First, such a system is *dynamical*, and its dynamics is organized in *multiple*, nested levels of descriptions. Second, such organization comes from certain non-trivial *coordination* between many separate processes. We may call such a complex system a multiscale coordinative structure.

Living animals are perhaps the most prominent examples of multiscale coordinative structures as here suggested by Waddington [1], but similar properties are also exhibited by complex social systems [2, 3], which can be thought of as an extension to the levels of living animals. Moreover, what is most intriguing is that there are such shared organizational principles across physical, biological, social, and artificial systems [4, 5].

The question is what kind of coordination, under what conditions, make multiple separate processes one single multiscale structure, i.e. unifying them but without losing complexity. One observation is that individual participants at a given level of a multiscale coordinative structure behave in a qualitatively different and often more

sophisticated manner than when they are outside of such a structure (i.e. emergent behavior [6–8]). For example, four elements – O, C, H, N – make up 96% of human body mass [9], but their daily activities can be vastly different depending on whether they are in an living animal or in a soup. The same can be said about human behavior in a civilization [10] or organized crime [11] compared to what it is outside of such social institutions. This means that multiple interaction patterns of lower-level components can all be stable (in the real world of course, what is stable always depends on the time scale at which stability is defined). But once certain patterns are formed (those that lead to a multiscale coordinative structure), the resulting higher-level structures must provide additional guidance to the behaviors at lower levels to the extent that, in return, they themselves are reinforced.

To study this problem theoretically, one first needs sufficiently general mathematical models of coordination dynamics that are restricted to neither a single level of description nor the type of behavior of a specific constituting substance. One would also want those models to be, in principle, able to capture some of the qualitative features above in more definite terms. Most importantly, one would not want such models to be detached from reality so that they could never be tested in, or provide understanding of, any specific system. There is likely to be a family of models satisfying these criteria. If that is the case, we can proceed to find even more general mathematical principles that define this family of models.

One easy way to start is to model a general behavior (behavior that can be observed in many systems) based on empirical observations of such behavior in a specific system. This is exactly what we have done in this dissertation. The general behavior is rhythmic coordination (see Section 2.1), and the specific system to provide empirical data is an ensemble of humans (Chapter 2). Subsequently, we captured empirically observed behavior on multiple levels of description with a single model (equation 3.1 of Chapter 3). This model also reconciled two preexisting and well-known models of

coordination, namely, the Kuramoto model [12] (devised to capture gross-level statistical features in large-scale coordination) and the extended Haken-Kelso-Bunz (HKB) model [13] (devised to capture finer dynamics in small-scale coordination), which were developed independently from each other. Nevertheless, both models share a conceptual origin in *Synergetics* [14–17], “the science of cooperation”, founded by Hermann Haken (the connection is evident in the Preface of [12] and the name HKB), which specifically deals with collective pattern generation in multi-component systems via self-organization processes. In the following sections of this Chapter, we briefly review these two preexisting models (the Kuramoto model in Section 1.2; the extended HKB in Section 1.3), and discuss the key features of coordination phenomena they capture, what is still missing, and the implications for our experimental design (Section 1.4).

1.2 LARGE-SCALE COORDINATION

Large-scale synchronization is among the most fundamental forms of collective behavior (synchronized flashing of fireflies, clapping of humans, firing of heart cells etc.) [18, 19], where diverse rhythmic processes coordinate into an coherent whole. The Kuramoto model provides a simple mathematical description of how a large number of diverse processes become one through an incoherence-to-coherence phase transition [12]. The model (equation 5.4.5 of [12]) takes the form

$$\dot{\varphi}_i = \omega_i - \frac{K}{N} \sum_{j=1}^N \sin(\varphi_i - \varphi_j) \quad (1.1)$$

where φ_i is the phase of the i^{th} oscillator, ω_i the natural frequency of the i^{th} oscillator (the frequency of the oscillator when it is left alone), N the total number of oscillators, and $K \geq 0$ the coupling strength (how much each oscillator is influenced by its relative phase to other oscillators). To represent (uncoupled) diversity in the population, the natural frequencies ω_i follow a random distribution with probability density function $P(\omega)$ symmetric around zero. Collective behavior is described by a complex order

parameter (mean field of all oscillators),

$$Z = r e^{i\Psi} = \frac{1}{N} \sum_{j=1}^N e^{i\varphi_j} \quad (1.2)$$

which can be thought of as a macro oscillator with amplitude r and phase Ψ . After a change of variable, equation (1.1) becomes

$$\dot{\varphi}_i = \omega_i - Kr \sin(\varphi_i - \Psi) \quad (1.3)$$

which states that each oscillator is entrained by the macro oscillator toward phase-locking (i.e. to be in a constant relative phase to the order parameter). It is apparent that whether the population behaves coherently will depend on how strong the entrainment is, determined by the percentage of oscillators that has already become phase-locked (reflected by r) and the coupling strength K . In fact, K must surpass a critical value for coherent behavior at a macro level to occur,

$$K_c = \frac{2}{\pi P(0)} \quad (1.4)$$

which marks the incoherence-to-coherence transition of the population.

Comparing this type of collective behavior to a multiscale coordinative structure (Section 1.1), one immediately notices a problem – once oscillators are absorbed into the whole, they behave identically and therefore are no longer separate processes. Synchronization as described here produces order without complexity, and what we need is order *with* complexity.

There are at least two ways to mitigate this loss of behavioral complexity at the micro level. One is to consider a more complex coupling function, e.g., to include more Fourier modes,

$$\dot{\varphi}_i = \omega_i - \frac{K}{N} \sum_{j=1}^N \sum_{k=1}^M c_k \sin k(\varphi_i - \varphi_j) \quad (1.5)$$

with integer $M > 1$ and c_k the coefficient for the k^{th} Fourier mode. This allows multiple phase clusters to coexist in the coherence regime [20]. Another is to look

into the incoherence regime itself ($K < K_c$), i.e. coordination without phase-locking, which may sound like an oxymoron but the reason will become clear later on (e.g. in Section 1.3 and Chapter 3).

Now that one is faced with infinitely many options as to what M , c_k and K should be, it is time to consult empirical data. One problem is that once we allow the behavior of individual oscillators to diversify, the micro-level patterns are no longer uniquely determined by this particular definition of order parameter in equation (1.2) (e.g. [21–23]) (given that the coupling strength K and coefficient c_k are unknown *a priori* in empirical data). Meaning, one cannot rely on the macro statistics (i.e. equation 1.2) alone to infer all necessary details of the coupling function. A systematic study of micro-level dynamics will certainly help, but this is not very practical for a large-scale system (N too big). Thus, when people want to model the micro-level dynamics in empirical observations, they usually turn to small-scale systems. The extended HKB [13] is an example of such small-scale models, which as we shall see is well-grounded in empirically observed coordination phenomena.

1.3 SMALL-SCALE COORDINATION

Rhythmic coordination at a small scale is perhaps best manifested in animal locomotion (e.g. swimming, walking, flying). Animals often have multiple stable gait patterns [24–26] and are able to switch between them (e.g. walk, trot, and gallop of a horse), which may be conceived as a kind of order-to-order phase transitions. The Haken-Kelso-Bunz (HKB) model [27] was initially developed to capture such a transition in human bimanual coordination (using finger coordination as a proxy to gait patterns, i.e. “let your fingers do the walking” [28]). If one moves two index fingers up and down rhythmically, it is easy to coordinate them inphase (up together, down together; synchronization) or antiphase (one up, the other down). The relative phase here is the collective variable or order parameter for the collective of two.

Interestingly, if the tempo of movement is increased, there will be a point where antiphase coordination is no longer stable [29]. This leads to a bistable-to-monostable transition, which can be observed as an antiphase-to-inphase transition if two fingers initially coordinated antiphase.

To capture these phenomena, the HKB model describes the coordination dynamics in the form

$$\dot{\phi} = -a \sin \phi - 2b \sin 2\phi \quad (1.6)$$

where ϕ is the relative phase between two oscillators, a the first order coupling strength, and b the second order coupling strength (i.e. coefficients of first two Fourier modes). It is the ratio between the second to first order coupling $k = b/a$ that determines whether the system is bistable or monostable. When the coupling ratio is greater than a critical value $k > k_c = 1/4$, the system has two stable fixed points, one at inphase $\phi = 0$ (in radian throughout this Chapter) and the other at antiphase $\phi = \pi$; when $k < k_c$, the system only has one stable fixed point at inphase. The critical coupling ratio k_c hence marks the bistable-to-monostable transition, capturing key observations in human behavior [29].

The existence of an order-to-order transition is an important distinction between the HKB (equation 1.6) and the Kuramoto model (equation 1.1), as the latter only accommodates disorder-to-order or order-to-disorder transitions. On the other hand, the HKB model does not actually have a disorder regime. Why? This has to do with the left-right symmetry of the bimanual coordination task used in the human experiment [29] – the natural movement frequency of the two fingers are very similar. The extended HKB [13] was then put forward to address the situation where the symmetry is broken,

$$\dot{\phi} = \delta\omega - a \sin \phi - 2b \sin 2\phi \quad (1.7)$$

where a term $\delta\omega$ was added denoting the difference between the natural frequency

of two oscillators. For a small increase of $\delta\omega$ (from zero), the two oscillators remain phase-locked, but the two fixed points are shifted away from being exactly inphase and antiphase. A further increase of $\delta\omega$ destabilizes the near-antiphase fixed point first, and eventually the near-inphase fixed point as well. After all fixed points are gone, the system is said to be *metastable*. This metastable regime of the extended HKB model corresponds to the incoherence regime of the Kuramoto model in the sense that there is no phase-locking. But a closer examination of the dynamics [13] shows that in this regime components can still be highly coordinated but in a recurrent rather than constant fashion, i.e. every time the two come close to certain phase relations (near the old attractors inphase and antiphase) they dwell there for a while (spending more time near old attractors than elsewhere; the time can be arbitrarily long depending on a , b and $\delta\omega$) and then escape from that relation until they meet again at another favorable relation. This phenomenon was first observed in fish by von Holst [24], who referred to it as *relative coordination*. After the proposal of metastability in the extended HKB, this type of relative coordination has been confirmed in further experiments (see [30–36]). Importantly, metastability allows integration and segregation to complement each other in the dynamics of coordination such that two oscillators can be coordinated without losing individuality [37].

In short, small-scale coordination observed in living systems exhibits more complexity, in the sense of multistability (multiple stable ordered patterns) and metastability (coordination without loss of separability), both captured by the extended HKB model. In other words, the extended HKB model captures order with complexity, which seems more suitable for describing the micro-level dynamics in multiscale coordinative structures as discussed in Section 1.1. But we still have a problem – the extended HKB is restricted to dyadic coordination, whereas a multiscale coordinative structure requires more separate processes at the micro level to accommodate multiple levels of description. Extensions to the case of $N = 4$ (to capture quadrupedal

gaits in humans and animals [30, 38, 39]) have been made (equation 17 of [38] and equation 1 of [39]), but the scale remains too small to be analyzed at multiple levels of description. To have a mathematical model that is corroborated by experimental evidence at multiple levels of description, we found it inevitable to turn to “midscale” experiments (i.e. experiments on systems with neither too few nor too many agents).

1.4 MID-SCALE COORDINATION

In the next few chapters, we present a series of studies based on a mid-scale human experiment ($N = 8$, eight-agent coordination, with a total of 120 subjects; see Chapter 2) [35]. An ensemble of eight is just large enough to form higher-level structures (e.g. grouping of agents) and small enough for lower-level details to be systematically examined (without combinatoric explosion). The goal is to study the coordination dynamics of eight people on multiple levels of description and to find an appropriate model that captures experimental observations on all those levels.

We also want to control and manipulate the boundary conditions of the system to see how they affect coordinative behavior. But what quantities to use to measure coordinative behavior and define boundary conditions? From what is common between the phenomena and models reviewed in Section 1.2 and 1.3, it is easy to see that the variable most relevant to the coordination dynamics is relative phase (ϕ for the HKB model, or $\phi_{ij} := \varphi_i - \varphi_j$ for the Kuramoto model), and what constrain the dynamics are natural frequencies ($\delta\omega$ the difference between natural frequencies in the HKB model, ω_i in the Kuramoto model) and coupling strength (a, b in the HKB model, K in the Kuramoto model). We therefore designed a new experimental paradigm, which can be considered as a physical realization of the system

$$\dot{\varphi}_i = \omega_i - \sum_{j=1}^N e_{ij} \Gamma(\varphi_i, \varphi_j) \quad (1.8)$$

where we can measure φ_i the phase of each subject’s movement (the time derivative

of phase $\dot{\varphi}_i = d\varphi_i/dt$, and relative phase $\phi_{ij} = \varphi_i - \varphi_j$ can be derived from phase dynamics), and manipulate ω_i the movement frequency of each subject (by metronome pacing) and coupling strength $e_{ij} \in \{0, 1\}$ (considered as connectivity). Here Γ is the unknown coupling function to be found.

Following this paradigm, a human experiment was conducted where we manipulated the natural frequencies (ω_i) of subjects to induce different grouping behavior at the macro level. Coordinative behavior was examined at intergroup, intragroup, and interpersonal levels. Detailed methods and results of this experimental study are shown in Chapter 2, which is reproduced from the published version [35] with minor modifications. In Chapter 3, we developed a model that successfully captured the experimental observations on multiple levels of description, effectively by adding the second order coupling of the HKB model to the Kuramoto model (or equation 1.5 with $M = 2$). Chapter 3 is a partial reproduction of the submitted version [40], with an added section on metastability (Section 3.2.6). By studying the behavior of the model, we found that metastable coordination between multiple agents produces both ordered and complex dynamic patterns. These metastable patterns can be classified based on the geometrical and topological features of their corresponding frequency graphs (each graph contains frequency time series of all agents). However, conventional tools are not designed for analyzing the geometric features of such graphs. Hence in Chapter 4, we developed a new technique for studying multiagent metastable coordination, using tools from computational algebraic topology. In this proof-of-concept study, we successfully captured, using this new technique, collective phase transitions in real data, which were difficult to detect by more traditional means. The combination of midscale experimentation, theoretical modeling and new data analytical methods constitute the initial steps that we found necessary to take toward a better understanding of multiscale coordinative structures.

CHAPTER 2

THE HUMAN FIREFLY EXPERIMENT

2.1 INTRODUCTION

The function of living systems (e.g. brain, human society, ecosystem) depends on the coordination of multiple components and processes. Such coordination depends on intrinsic characteristics of the interacting entities as well as the form of interaction between them [8, 16, 28, 41]. Living systems exhibit a myriad of rhythmic behaviors [42], e.g. humans with their daily, weekly, monthly routines [43] and physiological rhythms [44]; brains with their waves [45]; and species with their life-cycles [46]. By virtue of its temporal symmetry (i.e. translational symmetry in time), rhythmic coordination serves as a fine soil for experimental and theoretical study of laws of interaction between components of dynamical systems. The study of two interacting entities has laid experimental and theoretical foundations for addressing how coordinative structures form, adapt and change. Whether it is humans coordinating with sensory stimuli [13, 47], coordinated movements within the same person [29, 48–50], between two persons [51–57], two neuronal populations [31, 58], humans and machines [59–61], or humans and other species [62, 63], similar tendencies to form or learn certain relative phase and frequency patterns have been observed. Essential phase patterns, their stabilities and transitions have been well described mathematically in terms of informationally coupled dynamical systems [27, 38, 64, 65]. A little beyond dyads, triadic and tetradic coordination have been studied mainly in animal gaits or multilimb movements with a richer repertoire of patterns – combinations of dyadic patterns satisfying certain symmetry constraints [25, 30, 66–68]. Beyond sys-

tems with a relatively small number of interacting components, the focus of interest leaps toward systems of much larger scales – e.g. flashing fireflies [69], neuronal populations [70], or the clapping of an ardent audience [71] – whose sheer size eludes detailed investigational techniques but favors low-dimensional measures at coarser scales (e.g. collective synchronization). Such synchronization has been reproduced in various coupled oscillator models, e.g. [12, 72–74].

Despite this gap between systems of very few and very many components (with rare exceptions, [75]), daily social interaction often unfolds in the middle, for example, coordinating with a group of colleagues at work, or afterwards engaging in a variety of gatherings with friends and families, or various forms of folk dancing and Ceilidhs. The choice of the number of independently manipulatable components goes hand in hand with available paradigms for approaching coordination phenomena. With very few components, the repertoire of collective patterns and phase transitions can be fully explored with the help of experimental manipulation and theoretical models, but the limited size may curtail the complexity of spatial organizations. With very many components, possible coordination patterns (described at a microlevel) become too numerous to be studied exhaustively (due to high dimensionality of the phase space); the large number of components also makes it difficult to utilize systematic manipulations to carry the system through its repertoire of possible patterns. Instead, low-dimensional (macro) measures such as the overall level of synchronization can serve as an order parameter to capture collective states of the system [12, 16]. As important as such descriptions of coordination are, macro measures meet their limit when one attempts to characterize the system’s organizational complexity. Under the broad umbrella of “incoherent” states, what are the possible organizations? How can we explore such organizations systematically in the laboratory? To answer these kinds of questions, a way is needed to experimentally manipulate the system’s coordination dynamics on multiple spatial and temporal scales of description. We chose an

ensemble of intermediate size ($N = 8$ people) operating under the assumption that this is big enough to reveal the system’s organizational complexity, yet small enough to yield to experimental manipulation. Our strategy was to bridge this two-fold gap of system size and experimental control.

We studied rhythmic movement coordination in ensembles of eight people who were predisposed to move at the same or different frequencies. Existing empirical findings and theories suggest that the form and stability of coordination varies with the strength of coupling and the difference in natural frequency (frequency predisposition) between components, e.g. [13, 64, 76]. On this basis, we hypothesized that manipulating the distribution of frequency predispositions and coupling strength should produce different propensities for coordination, and induce different forms of collective behavior. Because it is possible to control systematically and measure quantitatively, frequency difference was chosen as a parameter to manipulate diversity within and between group members. We wanted to know how different diversity conditions favor the formation, persistence and change of multiple groups that are potentially integrated within themselves but segregated between each other.

2.2 RESULTS

Fifteen independent ensembles of eight people ($N=120$) participated in the study (for details see Section 2.5 Materials and Methods). All were instructed to tap rhythmically on a touchpad. At the beginning of each trial, members of an ensemble were each paced with a metronome; after the pacing period, they were able to see each other’s taps as flashes (dubbed “human fireflies”) on an array of LEDs situated at eye height in front of them. The task was to keep tapping at one’s own metronome frequency (tempo) throughout the entire trial. No instructions were given to coordinate with others.

To study how patterns of coordination among participants may form or dis-

solve, we introduced different levels of diversity by manipulating the assignment of metronomes to each participant. The metronomes divided the participants into two groups of four with frequency difference (δf , also referred to as level of diversity below) of either 0 Hz (1.5 vs. 1.5 Hz), 0.3 Hz (1.35 vs. 1.65 Hz), or 0.6 Hz (1.2 vs. 1.8 Hz). Within each group the four participants were paced at the same frequency. Overall, participants followed the metronome frequency during both pacing and interaction phases, in accord with instructions (see Section E in S1 file of [35]). In the following sections, we demonstrate the main findings, which may be best read along with the extended quantitative and theoretical analyses provided in the Supporting Information (S1 File) of [35] (the Sections A-D of the Supporting Information in [35] are reproduced in Appendix A for Methods-related references).

2.2.1 Spontaneous phase coordination and spatiotemporal metastability

The dynamics of relative phase between participants revealed that the participants spontaneously coordinated in various phase patterns and switched between them, despite not being given any instruction to do so. Such dynamic patterns are exemplified in Figure 2.1 A1-A3 which shows a trial of interaction among three persons (labeled with numbers 1, 3 and 4, reflecting spatial location on LED arrays, see legends under A2). The evolution of their relations is shown in (A1) as trajectories of dyadic relative phase (ϕ , reported in radians throughout this text) for pairs 3-4 (orange) and 1-3 (magenta). When a trajectory is horizontal, the pair is strongly coordinated by holding an (almost) constant phase relation (termed phase locking or dwell); when the trajectory is tilted, the pair is uncoordinated (phase wrapping). Dyad 3-4 (orange) engaged in a long dwell at inphase ($\phi \approx 0$, 10-35s in A1, largest peak in A2), then switched to a near antiphase pattern ($\phi \approx \pi$, 40s onward in A1, small peak in A2). Such near inphase/antiphase patterns are signs of bistability widely observed in biological coordination [32]. Dyad 1-3 (magenta) also coordinated near inphase but

in much briefer and recurrent dwells (around 10, 20, 30s in A1, largest magenta peak in A2), interleaved with escapes from it. This type of intermittent or relative coordination [24] characterized by consecutive epochs of dwells and escapes corresponds to the metastable regime in models of coordination dynamics [28, 33]. Evidence for metastability was often seen in single trial dynamics (see Section J in S1 file of [35] for a statistical approach). Besides bistable and metastable coordination observed within specific pairs of participants, a higher level interaction becomes apparent when we examine the two pairs together: during the long dwell of Dyad 3-4, three epochs of phase shift (bumps in orange curve at 15, 25, 35s in A1) followed precisely after each dwell of Dyad 1-3 (magenta). Moreover, as each dwell of Dyad 1-3 became longer than the previous one, the phase shift in Dyad 3-4 became bigger, to the point where the shift was so big (38s) that Dyad 3-4 broke up their predominant inphase pattern and switched to antiphase. This finding indicates that the joining of a new member (e.g. person 1) induced changes in preexisting coordinative relations (e.g. Dyad 3-4), strongly suggesting that multiagent coordination is more than the sum of isolated dyads (see Section H in S1 file of [35] for a statistical analysis). As an aid to visualization, the spatial arrangement corresponding to the foregoing temporal changes are illustrated in A3.

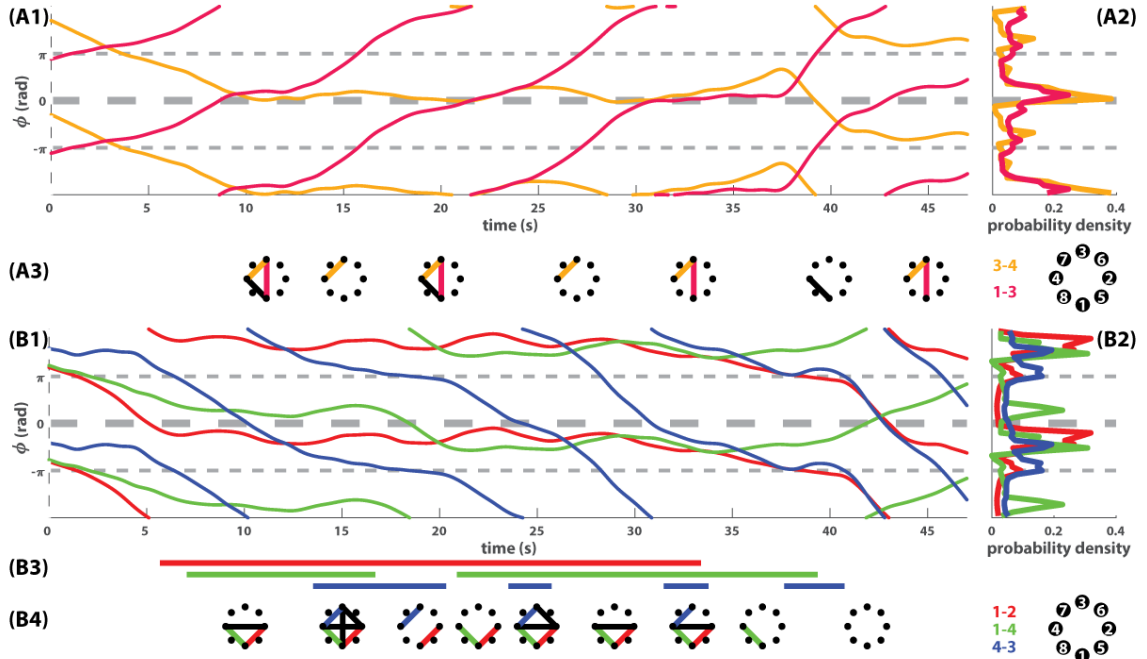


Figure 2.1: Coordination dynamics of phase relations among multiple agents. (A1) Exemplary relative phase trajectories show the metastable phase coordination of three persons (dynamics in $\phi \in [0, 2\pi]$) was repeated in $\phi \in [-2\pi, 0]$ for visual continuity). Shortly into the interaction stage (10s), dyad 3-4 coordinated near inphase for 25s (relative phase $\phi \approx 0$ orange, flattening of ϕ trajectories indicates phase coordination, or dwells), then switched into a pattern near antiphase ($\phi \approx \pm\pi$ orange, 40-47s). Dyad 1-3 also dwelled around inphase but for shorter durations (A1, magenta curve flattening around 12, 22, 32s). The interaction shows tendencies for bistability (inphase and antiphase), as also seen in the histograms of the relative phase (A2), with the orange distribution more pronounced at antiphase than the magenta. (A3) shows the spatial organizations of phase coordination among agents 1, 3, and 4 at moments corresponding to the time-axis in (A1; for interpretation see B4 below). (B1-4) shows an example of four-person interaction in similar format to the above. Dynamics of ϕ (B1) reveals phase coordination on various time scales, visualized in (B3) where the length of a bar annotates the duration of phase dwell between a pair of participants. Dyad 1-2 (red) showed the longest dwell, Dyad 1-4 (green) a bit shorter, and Dyad 4-3 (blue) the shortest. The coexistence of multiple timescales of coordination gives rise to a constantly evolving spatial organization of the group, shown as a sequence of graphs in (B4) where each node presents a participant and an edge indicates phase dwell (color coding corresponds to B1-3, black edges are dyadic dwells whose dynamics are not shown in B1-2; coordination within the other group, i.e. agents 5, 6, 7, 8, is not shown for reasons of clarity).

In the experiment, epochs of phase coordination were mostly transient or intermittent (i.e. metastable dwells), covering a wide range of time scales, with a mean

duration of 4.64s (± 4.04 s) and a long tail of more persistent phase patterns up to the entire duration of interaction, about 50s (See Fig B in S1 file of [35] for distribution). The confluence of metastability and multiple coupled agents allows the coexistence of multiple time scales of coordination in a group, as Figure 2.1 A1-A3 already hinted (orange – long dwell, magenta – short dwells with more frequent recurrence). Multiple coordinative time scales allow different members of a group to come together at different times, thus allowing the group to visit a variety of spatial patterns at different times. An example of four-person interaction is given in Figure 2.1 B1-B4 illustrated as three dyadic relative phases (dynamics in B1, distributions in B2). The duration of phase dwells is marked in (B3): red dyad with a long dwell, green dyad a bit shorter, and blue dyad even shorter. Such multiplicity in the time scale of metastable coordination led the four-person group through a variety of spatial patterns from moment to moment (B4) rather than to persist as a static structure (which would be the case if, e.g., phase coordination were absolutely stable). Thus, in the present case of intermediate sized group arrangements, spatiotemporal metastability – coexisting tendencies for integration and segregation – is rather more characteristic of coordination than collective synchronization [33, 77].

2.2.2 Dominant patterns of coordination and their relation to diversity

When all phase relations were considered in aggregate, we found that inphase coordination was clearly a dominant phase pattern (central peaks in distributions of relative phase ϕ in Figure 2.2). Yet this dominance of inphase depended on both local and global diversity. Inphase was more dominant locally within a group (participants paced at the same frequency) than between groups (where diversity was introduced by δf ; Figure 2.2, A1, probability density for within-group ϕ significantly above chance from 0 to 0.24π , A2, for between-group ϕ significantly above chance from 0.05π to 0.08π , at $\hat{p} < 0.05$, where ‘hat’ denotes Bonferroni correction for mul-

tiple comparison throughout the text; see Section G in S1 file of [35] for confidence intervals of chance level distribution). Globally, the dominance of inphase in the entire ensemble decreases as diversity increases (B1-3 for $\delta f = 0, 0.3, 0.6$ Hz respectively: B1 significantly above chance from 0 to 0.14π , B2 from 0 to 0.09π , $\hat{p} < 0.05$; B3 n.s.). This suggests that inphase coordination is an important characteristic for the formation and maintenance of coordinative structures regardless of group size, especially when diversity is low. A much weaker preference for antiphase can also be seen, primarily when the diversity is low (i.e. in Figure 2.2 A1 for within-group relative phase and B1 for $\delta f = 0$; based on bin-wise statistics, the antiphase is signified by the separatrix between inphase and antiphase near $\pi/2$ whose probability density is significantly lower than chance level, more specifically with $\hat{p} < 0.05$ at 0.48 to 0.5π and 0.54 to 0.58π for A1, 0.4π for A2, $0.58\pi, 0.62\pi$ and 0.65π for B1). Considering only epochs of strong coordination (dwells), we found a wide range of phase relations, where antiphase, along with inphase, was also a preferable phase relation (for details see Section F in S1 file of [35]).

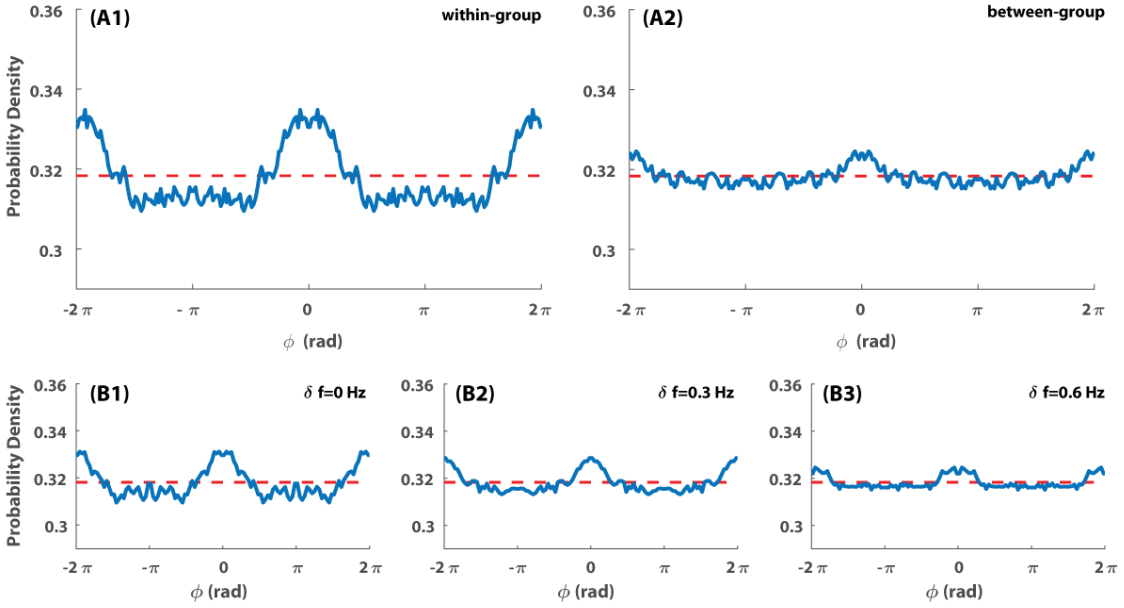


Figure 2.2: Aggregate distributions of phase relations. Blue solid lines are distributions of relative phases in the experiment (histograms were computed and statistically tested in the interval $[0, \pi]$ then repeated in the interval $[-2\pi, 2\pi]$ for visualization). Red dashed lines correspond to chance level (uniform) distribution. (A1) shows relative phase between members within the same frequency group, (A2) between different groups, (B1-3) for ensembles with diversity level $\delta f = 0, 0.3, 0.6$ Hz respectively. Inphase (central peak) is clearly a dominant pattern throughout, but its dominance diminishes with the diversity parameter displayed in (B1-3). Inphase preference was more pronounced within-group (A1), where participants shared the same initial frequency, than between-group, where frequency diversity was introduced (A2).

Beyond patterns of phase relations, other types of coordination were observed. One of them is a form of multifrequency coordination that binds behavior at different frequency ratios [49, 50, 78, 79]. We studied which frequency ratios constitute preferred coordination patterns by comparing their probability density to chance levels (computed from randomly permuted taps, see Section D in S1 file of [35] for details). Chance level distributions reflect expected occurrence of different frequency ratios as a result of participants' maintaining metronome frequencies without interacting with each other. Hence, we expected chance level distributions to peak around ratios corresponding to the three diversity conditions, i.e. 1:1 ($\delta = 0$ Hz), 9:11 ($\delta f = 0.3$

Hz), and 2:3 ($\delta f = 0.6$ Hz). Figure 2.3 shows the distribution of instantaneous frequency ratios in terms of within-group (Figure 2.3A) vs. between-group (Figure 2.3B) coordination for different levels of diversity (blue $\delta f = 0$ Hz, red $\delta f = 0.3$ Hz, yellow $\delta f = 0.6$ Hz). A frequency ratio is a preferred coordination pattern if its probability density (solid lines) is above chance level (light-color bands). Within-group participants coordinated primarily at 1:1 ratio (Figure 2.3A, all $\hat{p}'s < 0.05$), which is consistent with the high level of phase-locking reported above. For between-group coordination (Figure 2.3B), 1:1 was still the preferred ratio when there was no diversity ($\delta f = 0$ Hz, $\hat{p} < 0.05$); a higher order ratio near 2:3 was preferred when the diversity was large ($\delta f = 0.6$ Hz; $\hat{p} < 0.05$). For intermediate diversity ($\delta f = 0.3$ Hz), the between-group frequency coordination was barely above chance at metronome ratio 9:11 (for metronomes at 1.35 Hz and 1.65 Hz), but significantly more concentrated than chance near 1:1 ($\hat{p} < 0.05$). In short, under appropriate diversity conditions, lower order (1:1) and higher order (e.g. $\sim 2:3$) frequency coordination can coexist – a basis for complex spatiotemporal coordination. Furthermore, this type of coordination with frequency ratios (one which is less straightforward to detect and less studied) is specific to between-group interactions.

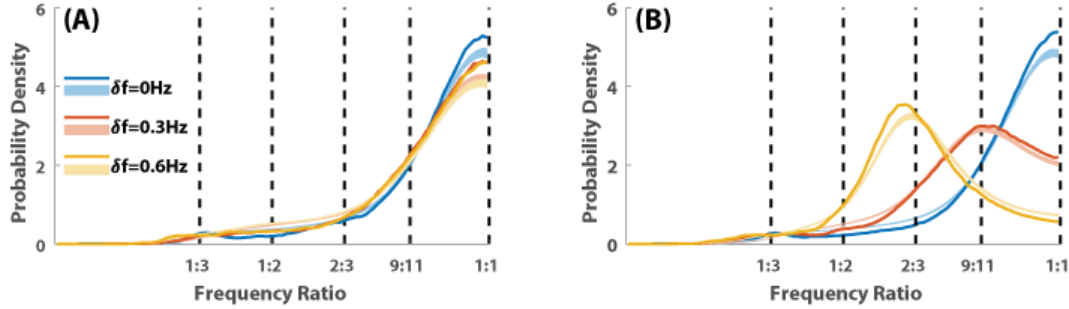


Figure 2.3: Multifrequency coordination. Ensembles with low diversity were dominated by 1:1 coordination, while ensembles with high diversity also steered towards higher-order ratios. Solid lines show the probability density of frequency relations within- (A) and between-group (B) for the 3 diversity conditions (color coded). Thin shaded areas (with corresponding colors) are confidence intervals for null distributions ($p < 0.0005$ for each of 100 bins, corresponding to $\hat{p} < 0.05$ for an entire distribution using Bonferroni Correction; generated from randomly permuted taps, which represent the expected distribution from non-interacting agents tapping at required frequencies). For within-group relations (A), the peaks at 1:1 are far above chance, indicative of stabilizing phase relations at the same frequency. For between-group relations (B), low to moderate diversity (blue, red, $\delta f = 0, 0.3$ Hz) led to above-chance coordination at 1:1; in contrast, for high diversity (yellow, $\delta f = 0.6$ Hz, corresponding to metronome ratio 2:3), coordination was below chance at 1:1 but far above chance at a higher order ratio near 2:3.

2.2.3 Segregation and integration of groups: critical diversity

Having studied coordination at the micro level (person to person), we now turn to the macro level of integration and segregation between groups. In order to do so, we first quantified coordination as the level of phase locking between individuals from the same and different initial groups (i.e. within- and between-group coordination respectively). Figure 2.4A shows the average results. We found that as initial frequency difference between groups (δf) increased, phase-locking between groups weakened dramatically (Figure 2.4A, right cluster). Interestingly, phase-locking within groups (no diversity within-group by design) was also weakened by virtue of the difference with the other group (Figure 2.4A, left cluster, notice orange and yellow bars significantly shorter than blue; MANOVA, interaction effect, $F(2, 7246) = 198.2, p < 0.001$; see S12 for MANOVA main effects analysis; see Section A.5 for a dynamic view).

That is, local coordination (e.g. within group) was influenced by the larger context (difference with other groups), as exemplified also in Figure 2.1A.

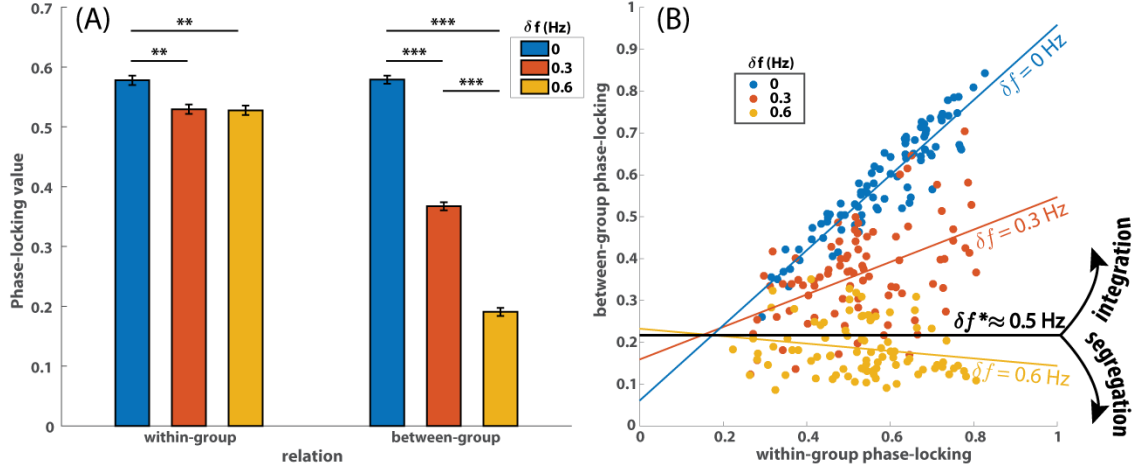


Figure 2.4: Diversity parametrically controls integration~segregation of groups within ensembles – the emergence of spatial scales. (A) Phase locking between groups decreased monotonically when between-group δf increased (A, right). Within groups however (A, left), where agents' initial frequencies were uniform, phase locking was still affected by the presence of another group of a different frequency (red, yellow bars significantly lower than blue bar), demonstrating that interactions are sensitive to the multiagent context in which they are embedded. (** $p < 0.01$; *** $p < 0.001$; error bars represent standard errors) (B) A scatterplot reveals linear associations between phase locking within- and between-group (each point represents a trial), whose slopes were modulated by the diversity parameter δf (denoted by color, see legend). Linear regressions had positive slope for lower diversity (blue and red colored lines) indicating integration of initial groups into larger coordinative structures, while a negative slope was found for the largest diversity (yellow line), indicating intergroup segregation. A critical parameter of diversity (δf^*) was identified that borders the regimes of integration and segregation (black line).

Next, we quantified group-level segregation~integration by studying the relation between within-group and between-group coordination. If more within-group coordination leads to more between-group coordination, the groups may be said to become integrated. If more within-group coordination leads to less between-group coordination, the groups may be said to become segregated. In Figure 2.4B, for the zero intergroup difference ($\delta f = 0$ Hz, blue dots), a large value of within-group phase-locking is paired with a large value of between-group phase-locking, indicating that

the initial groups have merged. The same is true, though to a lesser extent, for $\delta f = 0.3$ Hz. For $\delta f = 0.6$ Hz, however, a larger value of within-group phase-locking is associated with a smaller value of between-group phase-locking, suggesting that stronger coordination within the group prevents coordination with members of the other group, or conversely, switching to another group reduces the coordination with one's original group. Quantitatively, for small diversity ($\delta f = 0, 0.3$ Hz), initial groups integrated into one supergroup, as seen from the positive slope of regression lines (Figure 2.4B, blue, red; $\beta_1^{0Hz} = 0.88$, $t(84) = 20.0$, $p < 0.001$; $\beta_1^{0.3Hz} = 0.31$, $t(84) = 3.94$, $p < 0.005$). For larger diversity ($\delta f = 0.6$ Hz), the groups became more segregated (negative slope; Figure 2.4B, yellow; $\beta_1^{0.6Hz} = -0.14$, $t(85) = -2.83$, $p < 0.01$).

To estimate the critical diversity that marks the boundary between integration and segregation, we regressed the degree of integration $\beta_1^{\delta f}$ against the intergroup difference δf . We found a significant negative linear relation between those variables (linear regression, $\alpha_0 = 0.86$, $t(1) = 20.5$, $p < 0.05$; $\alpha_1 = -1.70$, $t(1) = -15.7$, $p < 0.05$). By finding when integration vanishes ($\beta_1^{\delta f} = 0$), we identified a critical frequency difference (δf^*) of 0.5 Hz as a boundary between the two different macro-organizations, i.e. a critical value that distinguishes segregation and integration.

2.2.4 Segregation and transitions of spatial order

We now return to real time dynamics to unpack the meaning of macro-level “segregation” in the foregoing statistical conclusion. In an example shown in Figure 2.5, the ensemble was initially divided into two frequency groups (early on in Figure 2.5A; faster group of agents 1 to 4, slower group of agents 5 to 8), thanks to the large difference between their metronome frequency ($\delta f = 0.6$ Hz). Soon the ensemble developed into multiple local structures which were coordinated within and segregated between each other (three pairs 3-2, 5-7, 6-8, and two individuals 1, 4; this spatial

order can be easily seen in D, first two graphs, 10-25s). The large initial diversity allowed the coexistence of multiple segregated groups and enabled the ensemble to form a sustained spatial order by providing sufficient frequency isolation between local structures (in contrast to the low diversity scenario where spatial patterns go through constant reorganization, e.g. Figure 2.1, Fig S8). However, a segregated spatial order does not have to be static. To the contrary, there was a sudden transition from one segregated spatial order (A1 and 2nd graph in D) to another, also segregated, spatial order (A2 and 3rd graph in D, a period marked with multiple partner exchanges), then back to the original (A3, and 4th graph in D). This kind of micro-level exchange of members across frequency groups has been observed in 77% of the trials in segregated condition ($\delta f = 0.6$ Hz). It suggests that segregation is a macro property of ensembles, and sustaining despite the coexistence of dynamical exchanges at micro level.

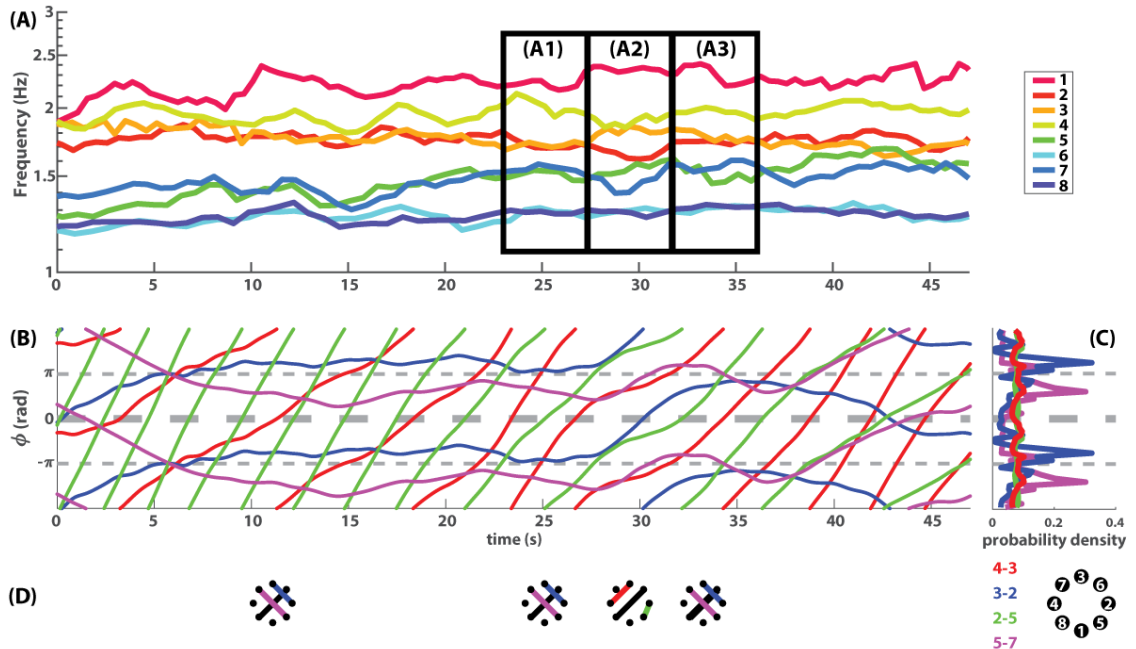


Figure 2.5: Frequency diversity contributes to spatial organization and reorganization. (A) Instantaneous frequencies of an ensemble of eight interacting agents (smoothed by averaging four consecutive taps). Agents 1 to 4 (warm colors) were paced with the same metronome frequency 1.8 Hz, and similarly agents 5 to 8 (cold colors) were paced at 1.2 Hz, (i.e. $\delta f = 0.6$ Hz), which helped create two initial frequency groups. Soon after the beginning of the interaction (~ 12 s, corresponding to the first graph in D), initial groups divided into five local structures: three pairs (3-2, 5-7, 6-8) and two individuals (agent 1 largely independent, agent 4 oscillating between agent 1 and pair 3-2). The frequency pairing held up to the time of (A1), then a sudden reorganization occurred from (A1) to (A2) – an exchange of partners (3-2 broke up and recoupled into 4-3, 2-5; 7 left alone; corresponding to the 3rd graph in D). The new pairing lasted a few seconds then returned to a similar organization to (A1) at the time of (A3). Phase relations of the pairs involved in the reorganization (A1-3) are illustrated in (B) as time series and in (C) as distributions of four dyadic relative phases. The new organization at A2 lasted exactly the time for pair 3-2 (blue) to break up an antiphase relation (27s) then return to it (33s) after phase wrapping for one cycle. This transition in phase relations corresponds closely to the transitions of frequency grouping. To visualize the spatial consequences of such phase/frequency regrouping, graphs in (D) were used as representations of the coordinative structure. Each node represents a participant at the actual location of the LED representing that participant (up to rotation). Each edge represents the existence of strong phase coordination between two participants at the time (aligned with x-axis in B). The spatial reorganization is apparent from the 2nd and 3rd graph aligned to (A1) and (A2) respectively. Interestingly, the 3rd graph, albeit distinct from the rest, is in fact isomorphic to the other graphs.

2.3 DISUCCSION

2.3.1 Integration and segregation in a diverse group

Rhythmic coordination is ubiquitous in natural systems from the cells of the heart to the neurons of the brain, from fireflies to people [18, 19, 28, 69, 71, 75, 80–82]. The convergence of multiple interacting elements to global synchronization has been the focus of experimental and theoretical studies [12, 71–74, 83, 84]. Behavioral synchronization is known to facilitate social communication and the development of social affection or bonding [85–89], and is important to understanding social coordination dynamics [90, 91]. Nevertheless, within a community, people coordinate in multiple social groups at various spatiotemporal scales – a complex organization that is far from uniform synchronization [92–94]. In fact, the components of living systems often compartmentalize into distinct communities or modules, highlighted by dense interactions within communities and loose interactions between communities [95, 96]. This form of organization, embracing both integration and segregation among its elements, can lead to greater persistence and robustness of the system [97–100], and influence structural and functional complexity depending on the scale of integration [101–103]. Investigation of the conditions leading to the formation, change, and dissolution of segregated structures is a necessary step to understanding and controlling complex systems.

We demonstrated experimentally how coexisting groups integrated and segregated in an ensemble of eight interacting people. Each half of the ensemble was predisposed to move at a distinct frequency prior to social interaction, thereby creating two initial frequency groups with a controllable parameter of diversity between them (δf). People engaged in more phase coordination with those who were predisposed to move at the same frequency than with those who performed at a different frequency (Figure 2.4A; Fig S11 left). This is a form of “homophily” – people prefer interacting with

those who are similar to themselves than with those who are different [104] – known to contribute to segregation in diverse communities [105–108]. Indeed, the integrating force of sameness is complemented by the segregating force of difference [37].

To what extent do quantitative changes in intergroup diversity induce a qualitative change in intergroup relationships? We have shown that low-to-moderate diversity led to integration of the groups ($\delta f = 0, 0.3$ Hz; Figure 2.1B): more coordination within-group was associated with more coordination between-group. High intergroup diversity led to segregation ($\delta f = 0.6$ Hz; Figure 2.1B): more coordination within-group was associated with less coordination between-group. Parametrically varying diversity made it possible to estimate the critical value of diversity (δf^*): exceeding this critical value led to macro-level segregation; remaining below the critical value led to macro-level integration. Identifying the critical values of a dynamical system empirically proves to be a valuable step in many situations, not only to provide essential information on the organizing principles and potential behaviors of the system, but also to serve as key phenomena to be reproduced in theoretical models [109, 110].

A complex system consists of interactions at multiple spatial scales, where activities at one scale are connected with those of another scale [4, 111]. How the macro environment constrains micro activities was illuminated by comparing dyadic interactions embedded in a group with expected behavior of dyads in isolation. If dyads (micro) were not influenced by the larger environmental context (macro), the same amount of coordination would be observed within groups at all three levels of intergroup diversity. The data say otherwise: phase locking within a group was in fact weakened by intergroup diversity (Figure 2.4A, left). This shows that when a system has multiple components, dyadic interactions may not be fully understood without taking into account the larger environment or context they are embedded in [8, 112, 113].

2.3.2 The patterns of coordination

To further understand the micro dynamics of social interaction, we identified the specific phase patterns people adopted. Overall, we found that inphase was visited significantly more often than other phase relation, yet its prominence diminished with increasing diversity (Figure 2.2). That is, diversity induced a dispersion of phase patterns. Absolute synchronization between components’ behavior is not always desirable: excessive synchrony may induce pathological collective dynamics [114] or impede complex functions [103, 115]. Diversity may come to the rescue. Besides inphase, a weaker preference of antiphase over various other phase relations also appeared (Figure 2.2; antiphase stood out more in episodes of strong interactions, see Fig C in S1 File of [35]). The present results resonate with existing studies of human rhythmic coordination [27, 28]. When coupling was sufficiently strong, the tendency for two oscillatory components to coordinate inphase or antiphase was found across scales, particularly when the components have similar frequency predispositions [116]. When coupling was sufficiently weak, however, the antiphase pattern was more susceptible to natural frequency differences (see e.g. [13, 64, 76]). Both diversity in frequency predispositions [13] and multiagent environment [25, 67, 117–119] help engender a variety of phase relations that are neither inphase nor antiphase. The agreement between the statistical properties of the interactive behaviors in an ensemble of eight persons and the dynamic properties of dyadic coordination suggests that dyads remain the most stable unit of spontaneous coordination. Yet how can group coordination be achieved with primarily dyadic interactions? This led us to explore the dynamics of phase relations.

Phase relations do not have to be static, as social coordination often evolves on multiple time scales [92, 93, 120]. Over the course of interaction, we found that most phase relations only lasted a short period of time (4-5s, Fig B in S1 File of [35]). Two partners dwell in a phase relation for a few seconds before a “breakup” or “es-

cape” from that relation, and then re-engage the next time they come across a favorable phase relation (e.g. Figure 2.1). The recurrent relation embodied by a series of dwells and escapes is characteristic of metastable coordination dynamics [33,116,121]. Theoretically and empirically, metastability occurs in weakly coupled dynamical systems when there is sufficient difference in the components’ frequency predispositions. The combination of symmetry breaking and weak coupling eliminates perfectly stable phase relations which are replaced by intermittent or recurrent phasing. In the present study, quantitative analysis confirms that metastability prevails in all conditions of interaction (Fig SJ in S1 File of [35]). Notice that, the sequence of dwells and escapes of phase relations also manifests as oscillations in movement frequency (e.g. Fig G in S1 File of [35]). In contrast with stable coordination in which components eventually converge to the same frequency, metastability allows components to visit a range of frequencies while still maintaining “social bonds” via intermittent dwells. When multiple metastable relations coexist in the same group, it becomes possible for a person’s transient escape from an existing relation to be at the same time a dwell in a new relation. This chimeric feature (c.f. [77]) allows members of a community to participate in multiple segregated substructures (e.g. a reading club, and a hiking team) while maintaining both the separability of those substructures and communication between them. Such continuous change of membership helps large communities to persist [122] and increase global level of cooperation [123]. Spatiotemporal metastability in multiple-component systems suits both the intuition of daily social interaction, as well as the dynamic patterns observed in large scale social networks [92].

Phase-locking constitutes a rather strong form of coordination. Such coordination comes at a cost in both time and energy if the partners possess different frequency predispositions: the chasm of frequency difference, jointly or unilaterally, must somehow be crossed. In the present experiment, not all forms of coordination required such

costly crossovers. As diversity increased, people from different groups were found to adopt particular frequency relations (or ratios) of higher order (e.g. near 2:3, Fig 3B, yellow) as opposed to converging to a single frequency (1:1). Frequency relations appear in the more familiar context of music as polyrhythms. Theoretical and experimental studies have shown the viability of different frequency ratios: higher order ratios (e.g. 2:5, 3:5) are more difficult to maintain (less stable) than lower order ratios (e.g. 1:3, 2:3) in accordance with so-called Arnold tongue and Farey tree principles [50, 79, 124, 125]. Such frequency relations enable segregated groups to maintain communication between each other, without sacrificing within-group cohesion, thus allowing complex coordinative structures to form. Such cross-frequency communication may serve to integrate local activities over long distance and time scales in complex systems, including the brain [4, 126, 127].

2.4 CONCLUSIONS

Our goal was to elucidate the coordination dynamics of ensembles of eight people, where the ensemble is small enough for systematic manipulation in the laboratory, but not too small as to prevent the unfolding of complex social dynamics (i.e., simple, but no simpler). At the macro level, we studied the integration and segregation of groups and how it affects, at the micro level, dyadic interactions embedded within. A novel finding was that the domains of integration and segregation between groups are demarcated by a critical level of intergroup diversity. Diversity across groups also affected the strength and forms of dyadic coordination within groups. In particular, a metastable form of phase coordination was revealed in which phase relations were intermittent rather than stable, thereby allowing people to switch flexibly between partners as a means of maintaining both diversity and unity. When groups were segregated and phase coordination became difficult, social coordination also took the form of cross-frequency coupling. The present work provides a multiscale portrait

of the coordination dynamics among multiple agents, and thereby offers quantitative details and reality checks for modelling social dynamics. The analytical methods used here can be extended to study segregation and integration in larger systems, where an abundance of scales of interaction is likely to further unveil the complexity and stability of large scale networks or coordinative structures.

2.5 MATERIALS AND METHODS

2.5.1 Participants

120 participants (76 female, age 24 ± 8 yrs.) participated in the experiment, making up 15 independent ensembles of eight. All participants were right-handed except 4, who were all able to complete the tasks without difficulty. The protocol was approved by Florida Atlantic University Institutional Review Board and in agreement with the Declaration of Helsinki. Informed consent was obtained from all participants prior to the experiment.

2.5.2 Experimental setup

For each ensemble of eight, participants were randomly seated in booths around an octagonal table. They did not have direct visual contact with each other. Each participant was equipped with a touchpad (green rectangle in Figure 2.6) and an array of eight light-emitting photodiodes (LEDs; yellow in Figure 2.6). Each tap of a participant was broadcast to all participants (including self) in real time as a single flash of an assigned LED (hand contacts touchpad, light on; hand leaves touchpad, light off). The tap flash signals were converted and transmitted through a signal processing pipeline consisting of a PC flanked by two microcontrollers (MCs; one for input, one for output; communicates with the PC through serial port at 57600 bps). The input MC samples movement data from the touchpads at 250 Hz (1=touch, 0=leave) and sends data to the PC. Dedicated software (written in C++) runs on the PC, which

receives tapping data from the input MC, and controls the spatial configuration of LEDs and the network connectivity among participants. The spatial configuration map assigns each LED on each array to represent a particular participant. The spatial configuration map was randomized across different ensembles of eight, but fixed for each ensemble throughout an experimental session. In this particular experiment, the network connectivity map determines whether a particular participant can see (1) only self-produced flashes; (2) self-produced flashes and a metronome (computer generated flashes, see Procedures); or (3) self- and other-produced flashes. After the spatial and network mapping are completed, the PC sends 64 bit data to 8 LED arrays via the output MC, synchronized to each sample from the input MC (tap-to-flash latency 2.5-4.5 ms, less than 1% of the shortest period of metronomes).

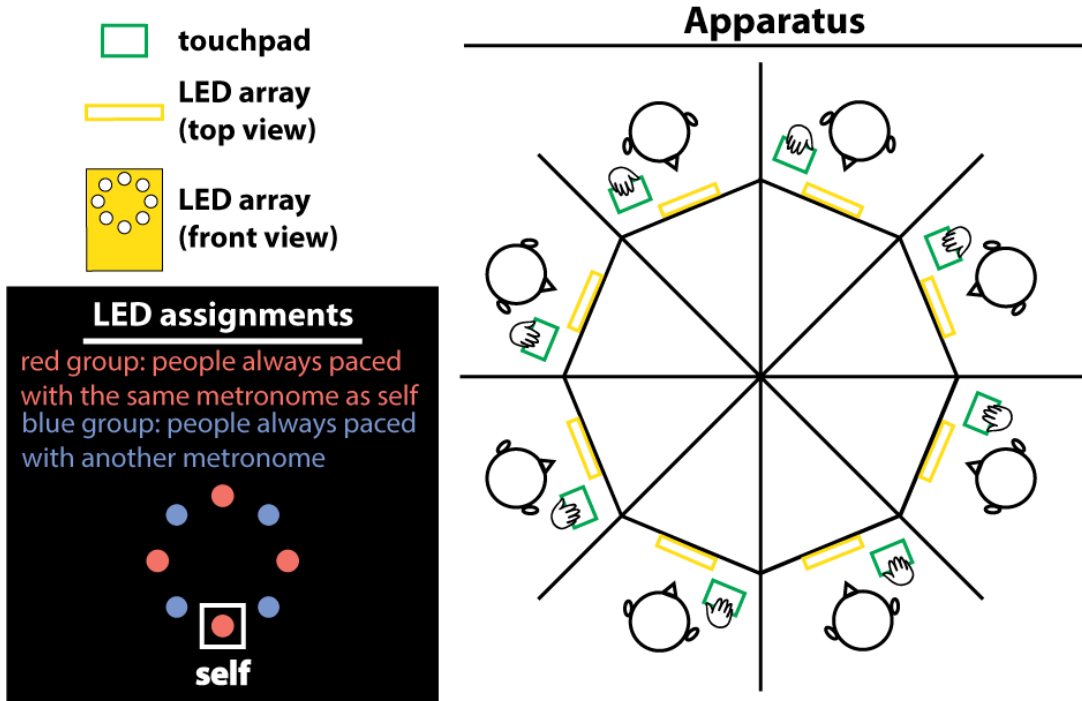


Figure 2.6: Experimental Setup. Eight participants are seated around an octagonal table; they do not have direct vision of each other. Rather, they are exposed to each other's tapping behavior through touchpads (record tapping; green) and arrays of LEDs (display self and others' taps as flashes; yellow). On each LED array, there is a one-to-one correspondence between LEDs and participants. (black panel) The mapping was rotated for each array so that a participant always saw self-behavior at the lowest LED (white box). All LEDs labeled red represent people who were paced by metronomes of the same frequency as for self. LEDs labelled blue represent people paced to metronomes at another frequency (actual LEDs were all in the same color). By such metronome assignment, participants of the same ensemble were split into two initial frequency groups. By manipulating the metronome difference between the two groups, we created different levels of diversity, thereby inducing integration~segregation at different spatial scales.

2.5.3 Procedures

Each trial of the experiment lasted 68s and consisted of three stages. In Stage 1 (5s), participants tapped rhythmically at their own comfortable frequency, only seeing self-produced flashes (Figure 2.6, black inset “self”). In Stage 2 (10s), all the non-self LEDs started to flash in synchrony at a preassigned frequency, basically a metronome (initial phase randomized between trials and subjects). Participants were instructed to match their own tapping frequency to the metronome frequency,

and remain tapping at that frequency throughout the rest of the trial even after the metronome disappeared. Following a 3s transient, subjects were exposed to each other's rhythmic behavior (Stage 3, 50s), each LED flashed corresponding to a particular participant's taps.

We manipulated intergroup behavior by assigning metronomes of different frequencies to different participants. In order to emphasize frequency diversity, spatial symmetry was imposed as follows: from each participant's perspective, persons presented at the north, west, and east of the center of the LED array were always paced with the same metronome as self (south to center), whilst the others were paced with another metronome. Thus, metronome assignment was designed to split eight people into two initial frequency groups (red group and blue group in Figure 2.6, black inset). Frequency diversity thus appears across groups not within groups. Specifically, for each trial, group metronomes were assigned following one of the three conditions: (1) 1.5 Hz vs. 1.5 Hz, (2) 1.65 Hz vs. 1.35 Hz, and (3) 1.8 Hz vs. 1.2 Hz. With the same mean frequency (1.5Hz), the three conditions correspond to three levels of between-group metronome difference (δf) which we term a diversity parameter: $\delta f = 0$ Hz, $\delta f = 0.3$ Hz, $\delta f = 0.6$ Hz.

Each ensemble of eight participants completed 24 trials in random order, including 6 trials in which participants were only connected to people within their own group (results not reported in this paper) and 18 trials in which every participant was connected to every other participant. In the present paper, we consider the effect of different levels of between-group difference on fully connected ensembles of eight people.

2.5.4 Statistical analyses

Distributions of relative phase (ϕ) and frequency ratio (FR) were compared to chance level using permutation tests. Ten thousand randomly permuted time series were used

for constructing the confidence intervals of chance level distributions. The significance level was chosen to be $\hat{p} = 0.05$ (with Bonferroni correction). Computational details are shown in Section A.1 and A.4 in Appendix A.

To compare the level of phase-locking in different conditions, two-way ANOVA was used (2×3 for *relation* \times δf) with Type III Sums of Squares; Tukey Honest Significant Difference tests were used for post hoc comparisons (see Section A.2 for details).

To measure the level of integration between groups, we regressed the level of within-group phase locking against between group phase-locking separately for 3 diversity levels. The slopes of the regression lines ($\beta_1^{\delta f}$) reflect the level of integration (positive slope = integration, negative slope = segregation). The critical level of diversity (δf^*), corresponding to zero-slope ($\beta_1 = 0$), was found through linear interpolation (see Section A.3 for details).

CHAPTER 3

A CROSS-SCALE MODEL OF COORDINATION DYNAMICS

3.1 INTRODUCTION

Coordination is central to living systems and their complexity, where the whole can be more than and different from the sum of its parts. Rhythmic coordination [44] is of particular interest for understanding the formation and change of spatiotemporal patterns in living systems, including e.g. slime mold [128], fireflies [129], social groups [71], and the brain [28, 33]. Theoretical formulations of coordination problems are often in terms of coupled oscillators, whose behavior is constrained by their phase relations with each other [12, 18, 38]. Existing studies of phase coordination often focus on systems of either very few oscillators (small-scale, mostly $N = 2$) [28, 39, 118], or very many oscillators (large-scale, $N \rightarrow \infty$) [130–132]. The in-between is barely covered. In the present work, we take an experiment-theory combined approach to show how coordination in-between helps us connect small-scale and large-scale theories of coordination.

But first, how are they different? Small-scale models were usually developed to capture empirically observed coordination patterns, as in animal gaits [66], bi-manual movement coordination [27, 29], neuronal coordination [133], interpersonal coordination [53, 134], human-animal coordination [62] and human-machine coordination [59, 60]. They describe multiple stable coordination patterns (multistability) and the transitions between them (order-to-order transitions), e.g. from a trot to a gallop for a horse [135]. In humans, dyadic coordination patterns like inphase and antiphase (synchronization, syncopation) were found across neural, sensorimotor, and

social levels (see [28, 33] for reviews), well captured by the Haken-Kelso-Bunz (HKB; for two identical components) [27] and extended Haken-Kelso-Bunz (HKB) model (extending the HKB to capture how phase relations are affected by the difference between two components; the extended HKB includes the HKB as a special case) [13, 64]. However, the extended HKB, while deeply grounded in empirical observations, was restricted to coordination problems of $N = 2$. In contrast, large-scale models are more concerned about statistical features like the overall level of synchrony, disorder-to-order transitions, but not so much about micro-level patterns. As a representative, the classical Kuramoto model [12] is applicable to describing a wide range of large-scale coordination among, e.g., people [73, 132], fish [136], and neural processes [131], often studied analytically for its incoherence-to-coherence transition (for $N \rightarrow \infty$; see [72, 137] for reviews).

Although the extended HKB and the classical Kuramoto model emerged separately, they connect to each other by an interesting difference: the Kuramoto model with $N = 2$ is *almost* the extended HKB model except that the former lacks the term responsible for antiphase coordination in the latter (more accurately, the bistability of inphase and antiphase). Bistability of inphase and antiphase coordination, with associated order-to-order transitions and hysteresis, happens to be a key observation in small-scale human experiments [29, 32]. This begs the question of whether there is a fundamental difference between large-scale and small-scale coordination phenomena. Does the existence of antiphase, multistability, and order-to-order transitions depend on scale N ? With these questions in mind, we recently conducted a human experiment [35] at an intermediate scale ($N = 8$), such that the system is large enough for studying its macro-level properties, yet small enough for examining micro-level patterns. In the present work, we developed a theoretical model that successfully captures key observations in this experiment at multiple levels of description, and at the same time connects small-scale and large-scale coordination.

3.2 RESULTS

3.2.1 Human coordination at intermediate scales

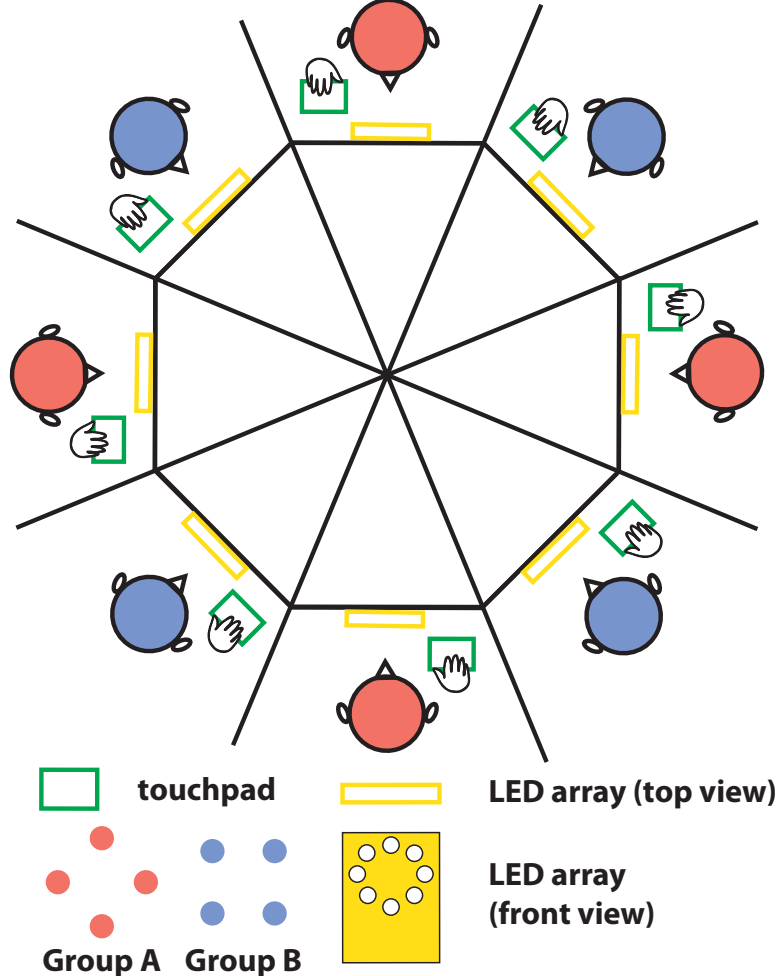


Figure 3.1: Experimental setup for multiagent coordination. In the Human Firefly experiment [35], eight subjects interacted simultaneously with each other via a set of touchpads and LED arrays. In each trial, each subject was paced with a metronome prior to interaction. The metronome assignment split the ensemble of eight into two frequency groups of four (group A and B, colored red and blue respectively). The frequency difference δf between group A and B were systematically manipulated to induce different grouping behavior. See text for details.

Before getting into the model, we briefly review the mid-scale experiment and key results [35]. In the experiment (dubbed the “Human Firefly” experiment), ensembles of eight people ($N = 8$, total 120 subjects) spontaneously coordinated rhythmic movements in an all-to-all network (via 8 touchpads, and 8 ring-shaped arrays of 8

LEDs as in Figure 3.1; see Materials and Methods for details). To induce different grouping behavior, subjects were paced with different metronomes prior to interaction such that each ensemble was split into two frequency groups of equal size with inter-group difference $\delta f = 0, 0.3$, or 0.6 Hz (referred to as levels of “diversity”), and were asked to maintain that frequency during interaction after the metronome was turned off. Subjects’ actual frequencies from three example trials (Figure 3.2A-C) show intuitively the consequences of frequency manipulations: from (A) to (C) a supergroup of eight gradually split into two frequency groups of four as diversity increased from $\delta f = 0$ Hz to 0.6 Hz.

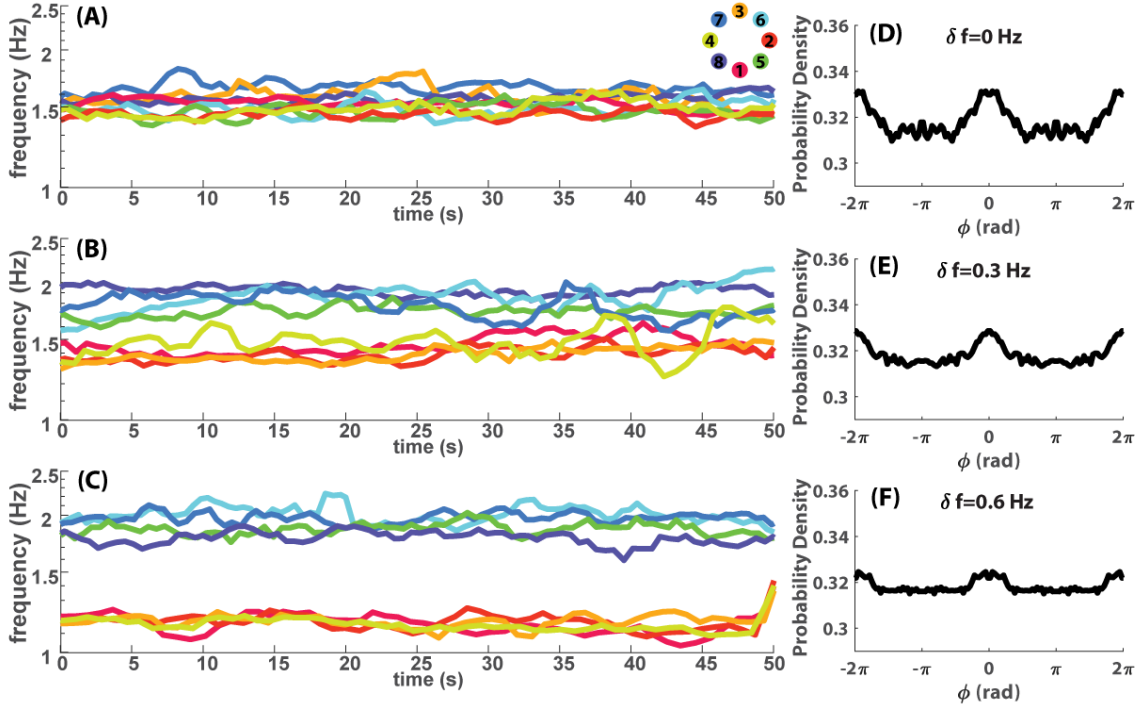


Figure 3.2: Examples of frequency dynamics and aggregated relative phase distributions for three diversity conditions. (A-C) shows instantaneous frequency (average over four cycles) from three trials with diversity $\delta f = 0, 0.3, 0.6$ Hz respectively. Viewed from bottom to top, in (C), two frequency groups of four are apparent and isolated due to high intergroup difference (low-frequency group, warm colors, paced with metronome $f_A = 1.2$ Hz; high-frequency group, cold colors, paced with metronome $f_B = 1.8$ Hz). As the two groups get closer (B), more cross-talk occurred between them (note contacting trajectories especially after 30s). Finally when the intergroup difference is gone (A), one supergroup of eight formed. (D-F) show relative phase ϕ distributions aggregated from all trials for $\delta f = 0, 0.3, 0.6$ Hz respectively (histograms computed in $[0, \pi]$, plotted in $[-2\pi, 2\pi]$ by symmetry and periodicity). When diversity is low (D), the distribution peaks near inphase ($\phi = 0$) and antiphase ($\phi = \pi$), separated by a trough near $\pi/2$, with antiphase weaker than inphase. The two peaks are diminished as δf increases (E,F), but the weaker one at antiphase becomes flat first (F).

Key results involve multiple levels of description, in terms of intergroup, intragroup and interpersonal relations. The level of intergroup integration is defined as the relation between intragroup and intergroup coordination (β_1 , slope of regression lines in Figure 3.3A; see Materials and Methods). Two frequency groups are integrated when diversity is low or moderate ($\delta f = 0, 0.3$ Hz, blue and red lines, slope $\beta_1 > 0$) and segregated when diversity is high ($\delta f = 0.6$ Hz, yellow line, slope $\beta_1 < 0$). A critical

level of diversity demarcating the regime of integration and segregation was estimated to be $\delta f^* = 0.5$ Hz. At the interpersonal level, inphase and antiphase were preferred phase relations (inphase much stronger than antiphase; distributions in Figure 3.2D-F), especially when the diversity was very low (Figure 3.2D, peaks around $\phi = 0, \pi$, in *radians* throughout this paper), but both were weakened by increasing diversity (Figure 3.2EF; in episodes of strong coordination, antiphase is greatly amplified, and much more susceptible to diversity than inphase, see [35]). Notice that subjects did not lock into these phase relations but rather engaged and disengaged intermittently (two persons dwell at and escape from preferred phase relations recurrently, a sign of metastability; see Figure 3.5A red trajectory for example), reflected also as “kissing” and “splitting” of frequency trajectories (e.g. in Figure 3.2B).

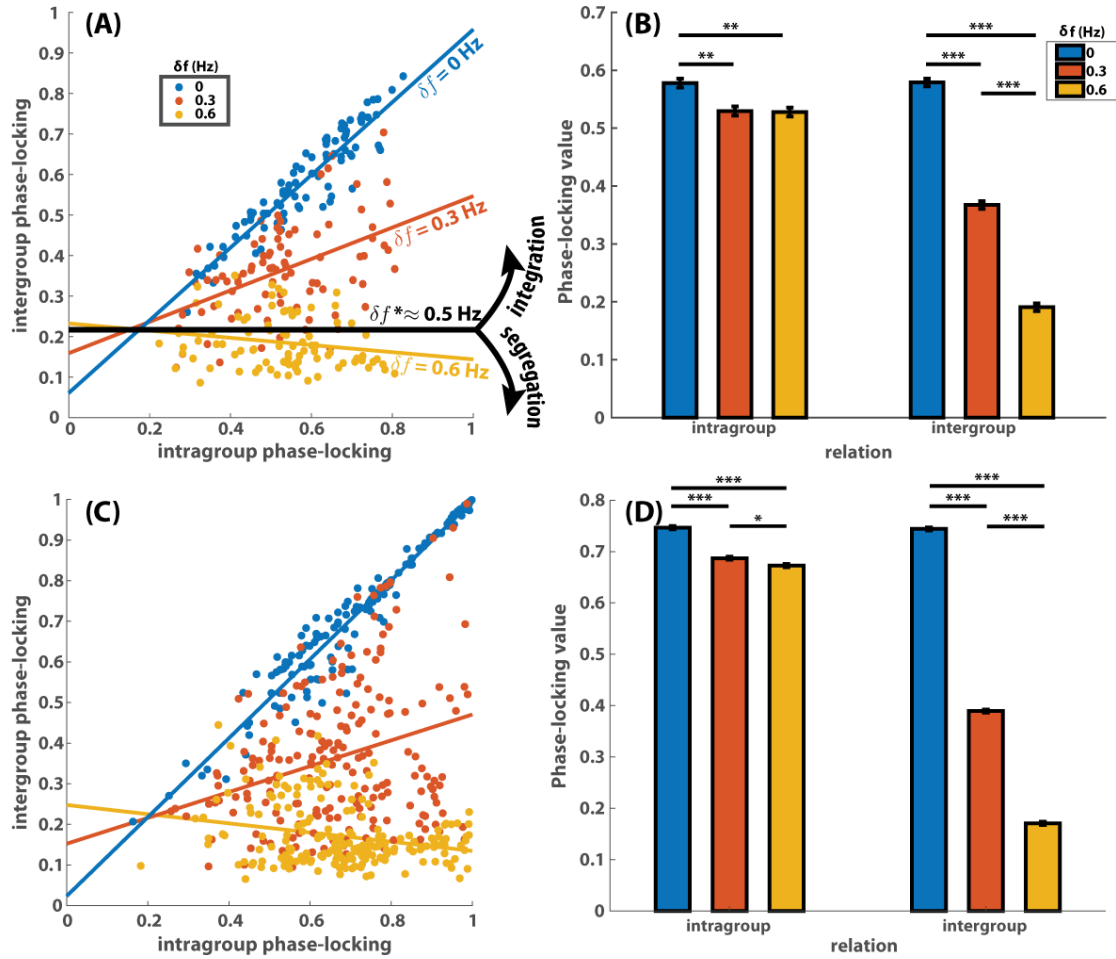


Figure 3.3: Intergroup relations and average inter/intragroup coordination. (A) shows how intragroup coordination relates to intergroup coordination for different levels of diversity (δf , color-coded) in the “Human Firefly” experiment [35]. Each dot’s x- and y-coordinate reflect the level of intragroup and intergroup coordination respectively (measured by phase-locking value). Lines of corresponding colors are regression lines fitted for each diversity condition (slope β_1 indicates the level of integration). With low and moderate diversity (blue and red), two frequency groups are integrated (positive slopes); and with high diversity (yellow), two frequency groups are segregated (negative slope). Black line (zero slope) indicates the empirically estimated critical diversity δf^* , demarcating the regimes of integration and segregation. The exact same analyses were applied to the simulated data (200 trials per diversity condition) and the results are shown in (C), which highly resemble their counterparts in (A). (B) shows a break-down of the average level of dyadic coordination as a function of diversity (color) and whether the dyadic relation was intragroup (left) or intergroup (right). Intragroup coordination was reduced by the presence of intergroup diversity ($\delta f \neq 0$; left red, yellow bars shorter than left blue bar); intergroup coordination dropped rapidly with increasing δf (right three bars; error bars reflect standard errors). Results of the same analyses on simulated data are shown in (D), which again highly resembles the human data in (B).

In the following sections, we present a model that captures these key experimental observations at both macro (intergroup) and micro (interpersonal) levels of descriptions.

3.2.2 A minimal experiment-based model of multiagent coordination

Our model of coordination is based on a family of N oscillators, each represented by a single phase angle φ_i . We will show that a pair-wise phase coupling [12, 27, 66] of the form

$$\dot{\varphi}_i = \omega_i - \sum_{j=1}^N a_{ij} \sin(\varphi_i - \varphi_j) - \sum_{j=1}^N b_{ij} \sin 2(\varphi_i - \varphi_j) \quad (3.1)$$

suffices to model the key features of the experimental data identified above. The left side of this equation is the time derivative of φ_i , while the constant $\omega_i > 0$ on the right is the natural (*i.e.*, uncoupled) frequency of the i^{th} oscillator. The coefficients $a_{ij} > 0$ and $b_{ij} > 0$ are parameters that govern the strength of coupling.

The equations (3.1) include a number of well-studied models as special cases. For instance, setting $\phi := \varphi_1 - \varphi_2$, $\delta\omega := \omega_1 - \omega_2$, $\tilde{a} := a_{12} + a_{21}$, and $2\tilde{b} := b_{12} + b_{21}$ for $N = 2$, the difference of the two resulting equations (3.1) yields the relative phase equation

$$\dot{\phi} = \delta\omega - \tilde{a} \sin \phi - 2\tilde{b} \sin 2\phi \quad (3.2)$$

of the extended HKB model [13]. The HKB model was originally designed to describe the dynamics of human bimanual coordination, and has since been shown to apply to a broad variety of dyadic coordination phenomena in living systems (see [28, 138] for details). Equations (3.1) generalize the extended HKB model to N oscillators in a straightforward way. It is quite remarkable that such a straightforward generalization can reproduce key features of the collective rhythmic coordination among *groups* of human subjects, who moreover couple to one another experimentally through a rudimentary, visual stimulus.

Another well-studied special case of equations (3.1) is the Kuramoto model [12], which has $b_{ij} = 0$ (and typically $a_{ij} = a$, independent of i and j). We will see below, however, that the Kuramoto model cannot exhibit at least one feature of the experimental data. Namely, the data show a secondary peak in the pairwise relative phase of experimental subjects at antiphase, along with a major peak at inphase (see Figure 3.2D-F above). Simulations using the Kuramoto model do not reproduce this effect, while simulations of equations (3.1) model do (compare Figure 3.4 D-F and G-I below). We give additional analytical support for this point by studying relevant fixed points of both models in the Appendix B (Section B.7).

3.2.3 Weak coupling captures human behavior

Given the spatially symmetric setup of the “Human Firefly” experiment (all-to-all network, visual presentation at equal distance to fixation point), it is reasonable to further simplify equations (3.1) by letting $a_{ij} = a$ and $b_{ij} = b$ ($a, b > 0$),

$$\dot{\varphi}_i = \omega_i - a \sum_{j=1}^N \sin \phi_{ij} - b \sum_{j=1}^N \sin 2\phi_{ij} \quad (3.3)$$

where $\phi_{ij} = \varphi_i - \varphi_j$ is the relative phase between oscillators i and j (henceforth we use the notation ϕ_{ij} instead of the subtraction, since relative phase is the crucial variable for coordination [27]).

At the level of intergroup relations, model behavior (Figure 3.3C; under weak coupling $a = b = 0.105$, which was chosen after a comprehensive study of the parameter space, see Section B.1 in Appendix B on parameter choices) successfully captures human behavior (Figure 3.3A) at all levels of diversity. Similar to the human experiment, low diversity ($\delta f = 0$ Hz) results in a high level of intergroup integration in the model (blue line in Figure 3.3C slope close to 1; $\beta_1 = 0.972$, $t(199) = 66.6$, $p < 0.001$); high diversity ($\delta f = 0.6$ Hz) comes with intergroup segregation (yellow line slope negative; $\beta_1 = -0.113$, $t(199) = -3.56$, $p < 0.001$); and in between, moderate diversity ($\delta f = 0.3$ Hz) is associated with partial integration (red line positive

slope far less than 1; $\beta_1 = 0.318$, $t(199) = 4.23$, $p < 0.001$). Here we did not estimate the critical diversity δf^* the same way as for the human data (by linear interpolation), since we found theoretically that the level of integration depends nonlinearly on diversity δf (see Figure B.1), and as a result the theoretical δf^* is 0.4 Hz (see Figure B.1D). This prediction can be tested in future experiments by making finer divisions between $\delta f = 0.3$ and 0.6 Hz.

In the human experiment, not only did we uncover the effect of diversity on intergroup relations, but also, non-trivially, on intragroup coordination (outside affects within, a sign of complexity). Statistically, this is shown in Figure 3.3B (three bars on the left): with the presence of intergroup difference ($\delta f > 0$), intragroup coordination was reduced (red, yellow bars significantly shorter than blue bar). This is well captured by the model as shown in Figure 3.3D (2-way ANOVA interaction effect, $F(2, 19194) = 3416$, $p < 0.001$; the simulated data also capture the rapid decline of intergroup coordination with increasing δf in human data, shown in Figure 3.3BD, right). To see what this means dynamically, three simulated trials are shown in Figure 3.4A-C as examples (same initial conditions and intragroup frequency dispersion). The phase-locked state within groups (when $\delta f = 0$ Hz; Figure 3.4A) is lost and replaced by metastable coordination (intermittent convergence, marked by black triangles in Figure 3.4BC) as soon as two groups begin to differentiate from each other ($\delta f = 0.3, 0.6$ Hz). In fact, the statistical result (Figure 3.3B, left) reflects how two groups collaboratively increased each other's intragroup coordination (see Section B.3 for baseline dynamics when intergroup coupling is removed, where intragroup coordination is always metastable, and Section B.4 in Appendix B for statistics when intragroup variability is removed). Comparing Figure 3.4B with C, we see the time scale of metastable convergence is also altered by intergroup difference δf (longer inter-convergence interval for C) - intergroup difference changes not only the overall *level* of coordination within groups, but also the *patterns* of coordination.

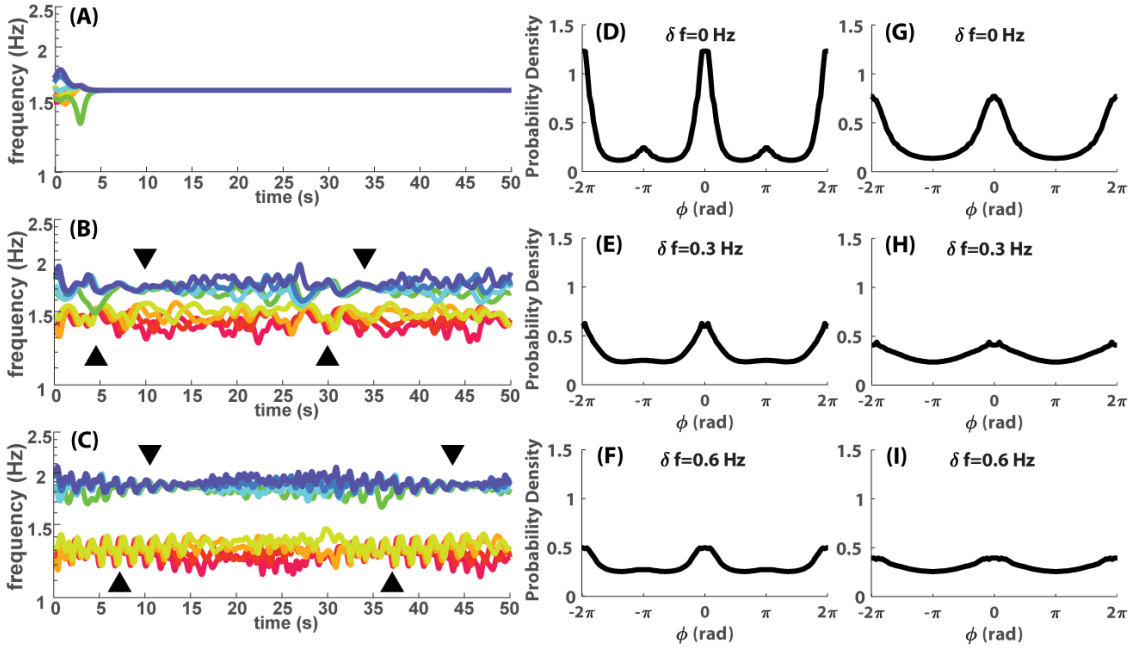


Figure 3.4: Examples of frequency dynamics and aggregated relative phase distributions for simulated data. (A-C) show frequency dynamics of three simulated trials ($a = b = 0.105$) with the same initial phases and intragroup frequency dispersion but different intergroup difference i.e. $\delta f = 0, 0.3, 0.6$ Hz respectively. When intergroup differences are introduced (BC), not only is intergroup interaction altered but intragroup coordination also loses stability and becomes metastable (within-group trajectories converge at black triangles and diverge afterwards). The time scale of metastable coordination also changes with δf , i.e. the inter-convergence interval was shorter for (B) than (C). (D-F) show relative phase distributions, aggregated over 200 trials ($a = b = 0.105$) for each diversity condition ($\delta f = 0, 0.3, 0.6$ respectively). At low diversity (D), there is a strong inphase peak and a weak antiphase peak, separated by a trough near $\pi/2$. Both peaks are diminished by increasing diversity (EF). These features are qualitatively the same as the human experiment. (G-I) show the same distributions as (D-F) but for $a = 0.154$ and $b = 0$ (i.e. the classical Kuramoto model). There is a single peak in each distribution at inphase $\phi = 0$, and a trough at antiphase $\phi = \pi$.

At interpersonal level, human subjects tended to coordinate with each other around inphase and antiphase, especially when the diversity is low ($\delta f = 0$ Hz; Figure 3.2D, peaks around $\phi = 0, \pi$ separated by a trough near $\phi = \pi/2$); and the preference for inphase and antiphase both diminishes as diversity increases ($\delta f = 0.3, 0.6$, Figure 3.2EF). These aspects are well reproduced in simulations of the equation (3.3) (Figure 3.4D-F). Note that these model-based distributions are overall less dispersed

than the more variable human-produced distributions (Figure 3.2D-F), likely due to the deterministic nature of the model (i.e. no stochastic term).

3.2.4 The necessity of second-order coupling

Equation (3.3) becomes the classical Kuramoto model [12] when $b = 0$. We follow the same analyses as in the previous section but now for $a = 0.154$ and $b = 0$ (see Section B.6 in Appendix B on parameter choices). The relationship between intragroup and intergroup coordination (Figure B.7A; $\beta_1(0Hz) = 0.974$, $t(199) = 53.2$, $p < 0.001$; $\beta_1(0.3Hz) = 0.292$, $t(199) = 4.52$, $p < 0.001$; $\beta_1(0.6Hz) = -0.011$, $t(199) = -0.41$, $p > 0.05$) resembles the case of $b \neq 0$ ($a = b = 0.105$, Figure 3.3C). A difference remains that for $b = 0$, $\beta_1(0.6Hz)$ is not significantly less than zero ($p = 0.68$) when $b = 0$. The average level of intragroup and intergroup coordination also varies with diversity in the same way as the case of $b \neq 0$ (Figure B.7B for $b = 0$, interaction effect $F(2, 19194) = 3737$, $p < 0.001$, compared to Figure 3.3D for $b \neq 0$). In short, group-level statistical features are mostly preserved without second order coupling (i.e. $b = 0$).

However, this is no longer the case when it comes to interpersonal relations. The distributions of dyadic relative phases are shown in Figure 3.4G-I. Without second order coupling, the model does not show a preference for antiphase in any of the three diversity conditions, thereby missing an important feature of human social coordination. Analytically, we find that the coupling ratio $\kappa = 2b/a$ determines whether antiphase is preferred (for the simple case of identical oscillators, in Section B.7 in Appendix B). A critical coupling ratio $\kappa_c = 1$ demarcates the regimes of monostability (only all-inphase is stable for $\kappa < 1$) and multistability (any combination of inphase and antiphase is stable for $\kappa > 1$). The critical ratio is identical to the critical coupling of the extended HKB model [13], where the transition between monostability (inphase) and multistability (inphase and antiphase) occurs (equation 3.2, parameters

in the two equations map to each other by $a = \tilde{a}/2$ and $b = \tilde{b}$). This shows further how equation (3.3) is a natural N-dimensional generalization of the extended HKB model, in terms of multistability and order-to-order transitions.

3.2.5 The effect of non-uniform coupling

So far, our model has captured very well experimental observations with the simple assumption of uniform coupling. However, loosening this assumption is necessary for understanding detailed dynamics. Here is an example from [35] (Figure 3.5A), where coordination among three agents (1, 3, and 4, labels of locations on LED arrays) is visualized as the dynamics of two relative phases (ϕ_{13} red, ϕ_{34} yellow). Agents 3 and 4 coordinated inphase persistently (10-40s yellow trajectory flat at $\phi_{34} \approx 0$), while agents 3 and 1 coordinated intermittently every time they passed by inphase (red trajectory ϕ_{13} becomes flat, i.e. dwells, near inphase around 10, 20 and 35s). Curiously, every dwell in ϕ_{13} (red) was accompanied by a little bump in ϕ_{34} , suggesting ϕ_{34} was periodically influenced by ϕ_{13} . In the framework of our model, we can approximate the dynamics of ϕ_{34} from equation (3.1) by assuming $\phi_{34} = 0$ (thus $\phi_{13} = \phi_{14}$),

$$\dot{\phi}_{34} = f(\phi_{34}) + \underbrace{(a_{31} - a_{41}) \sin \phi_{13} + (b_{31} - b_{41}) \sin 2\phi_{13}}_{=:K(\phi_{13})} \quad (3.4)$$

where $f(\phi_{34})$ is the influence of ϕ_{34} on itself, $K(\phi_{13})$ the influence of ϕ_{13} on ϕ_{34} . From $K(\phi_{13})$ we see that ϕ_{13} has no influence on ϕ_{34} if the coupling is completely uniform (i.e. $K(\phi_{13}) \equiv 0$ if $a_{31} = a_{41}$ and $b_{31} = b_{41}$). To break the symmetry between agent 3 and 4, we “upgrade” equation (3.3) to the system

$$\dot{\phi}_i = \omega_i - a_i \sum_{j=1}^N \sin \phi_{ij} - b_i \sum_{j=1}^N \sin 2\phi_{ij} \quad (3.5)$$

where each oscillator can have its own coupling style (oscillator specific coupling strength a_i and b_i). In the present case, we are interested in what happens when $a_3 \neq a_4$ for $i \in \{1, 3, 4\}$. Two simulated trials are shown in Figure 3.5BC, using the same initial conditions and natural frequencies estimated from the human data. The bumps in ϕ_{34} , accompanying dwells in ϕ_{13} , are reproduced when $a_3 \gg a_4$ (Figure 3.5B) but not when $a_3 = a_4$ (Figure 3.5C; see Section B.8 in Appendix B for more analyses). This example shows that to understand interesting dynamic patterns in specific trials, non-uniform coupling strength is important.

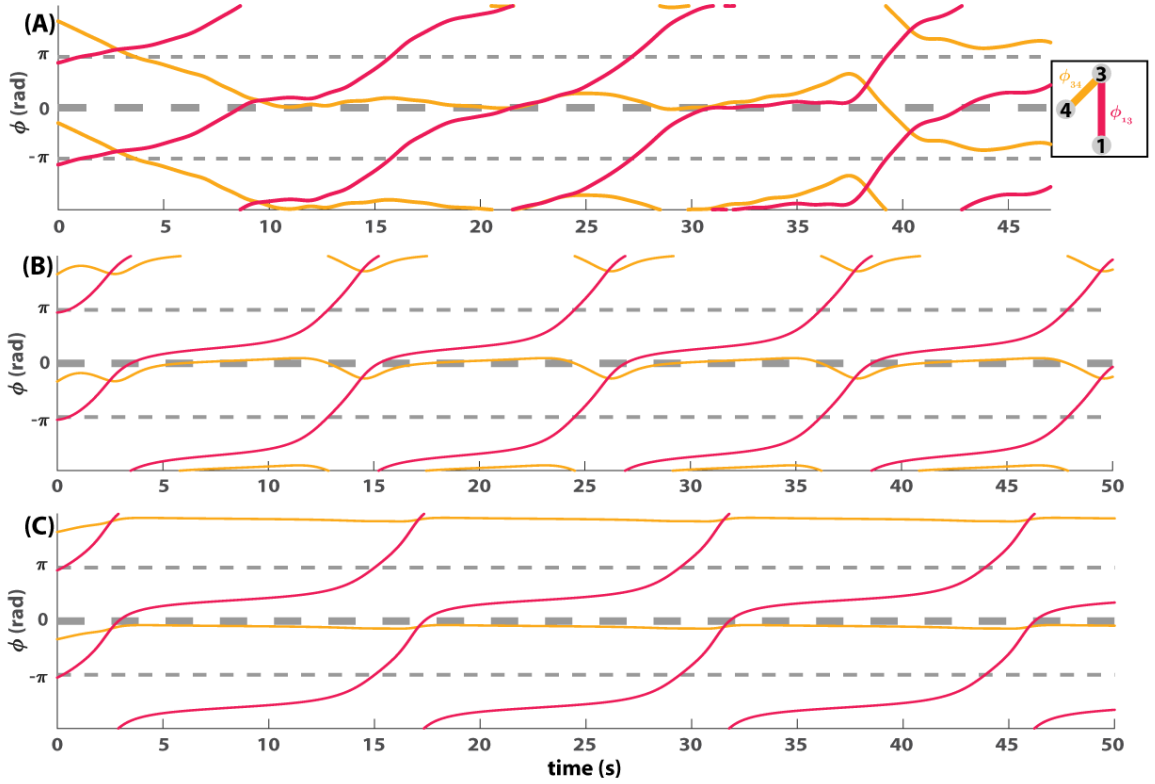


Figure 3.5: The effect of non-uniform coupling strength on coordination dynamics. (A) shows the evolution of the relationship between three persons (agent 1, 3, 4, spatially situated as in legend) in terms of two relative phases (ϕ_{13} , ϕ_{34}). ϕ_{34} (yellow) persisted at inphase for a long time (10–37s trajectory flattened near $\phi = 0$) before switching to antiphase (40s). ϕ_{13} (red) dwelled at inphase intermittently (flattening of trajectory around 10, 20, and 35s). Three bumps appeared in ϕ_{34} during its long dwell at inphase (near 15, 25, 37s), which followed the dwells in ϕ_{13} , indicating a possible influence of ϕ_{13} on ϕ_{34} . (B,C) show two simulated trials with identical initial conditions and natural frequencies, estimated from the human data. In (B), agent 3 is more “social” than agent 4 ($a_3 > a_4$). More precisely, agent 3 has a much stronger coupling ($a_3 = 1$) than all others ($a_1 = a_4 = b_1 = b_3 = b_4 = 0.105$, as in previous sections). The recurring bumps in ϕ_{34} are nicely reproduced. In (C), agent 3 and 4 are equally “social” ($a_3 = a_4 = 0.5525$, keeping the same average in (B)). ϕ_{34} is virtually flat throughout the trial.

3.2.6 Metastable coordination between more than two agents

In the preceding sections, we have shown how the model captures specific experimental observations at various levels of description. In this section, we further probe the model’s behavior for a better theoretical understanding of metastable coordination in the multiagent scenario (i.e. spatiotemporal metastability which few work has studied

in detail, e.g. [33]).

First, we show how metastable coordination between three oscillators is different from that of two. Between two oscillators (as studied in [13, 64]), coordination can be described as the dynamics of a single relative phase, which is confined to the underlying state space S^1 , i.e. a circle. For sufficiently large difference between the natural frequency of two oscillators (e.g. $\delta\omega$ in equation 3.2), all fixed points of the system (i.e. phase-locked solutions) are gone and a single periodic orbit emerges covering S^1 , at which point the system is said to be metastable. But so long as the system is metastable, manipulation of $\delta\omega$ will not create any qualitative change in the metastable dynamics – the relative phase orbit has a unique topology, identical to that of S^1 . This is no longer the case when a third oscillator is added into the system, as we will show next.

The coordination dynamics of three oscillators can be described by two phase relations. If one relation is metastable while the other is not (i.e. phase-locked), we may say the collective pattern is partially metastable. Since either one can be metastable, there are at least two partially metastable patterns. More concretely, consider a system of three oscillators (seen uncoupled in Figure 3.6 A1-3), two of which have fixed natural frequencies of 0 and 1 Hz (red, blue lines in Figure 3.6 A1 show their uncoupled frequency dynamics, i.e. time derivatives of their absolute phases φ_0 and φ_1). The third one has a variable natural frequency λ Hz (absolute phase φ_λ), where $\lambda \in [0, 1]$ (e.g. black line in Figure 3.6 A1 with $\lambda = 0.5$). If they are coupled (coupling strength $a = b = 1$ with respect to equation 3.3, which is just small enough such that the three are never all phase-locked), two partially metastable patterns are apparent – φ_λ is only phase-locked to either φ_1 (e.g. when $\lambda = 1$, relative phase $\phi_{1-\lambda} \equiv 0$; seen in Figure 3.6 B1 as black completely overlaps with the oscillator at 1 Hz on top) or φ_0 (e.g. when $\lambda = 0$, relative phase $\phi_{\lambda-0} \equiv 0$; seen in Figure 3.6 C1 as black completely overlaps with the oscillator at 0 Hz at the bottom). These

two patterns can be represented as two different loops (periodic orbits of relative phases $(\phi_{1-\lambda}(t), \phi_{\lambda-0}(t))^\top$ with $t \in [0, T]$ for an orbit of period T) on a torus $S^1 \times S^1$ (Figure 3.6 BC2-3) – a meridian loop (B3) and a longitudinal loop (C3) respectively. They are topologically distinct in the sense that you cannot continuously deform one into another (i.e. not homotopy equivalent). We can classify these two types of patterns by a pair of winding numbers (p, q) denoting how many times the loop wraps around the longitude and meridian circle respectively, i.e. $(0, 1)$ for (B3) and $(1, 0)$ for (C3). From this topological classification of metastable patterns, an interesting problem arises: how the transition between topologically distinct patterns (from C3 to B3) occurs under a continuous change of λ (from 0 to 1), or what types of, if any, metastable pattern exist in between. We address this question next by varying λ .

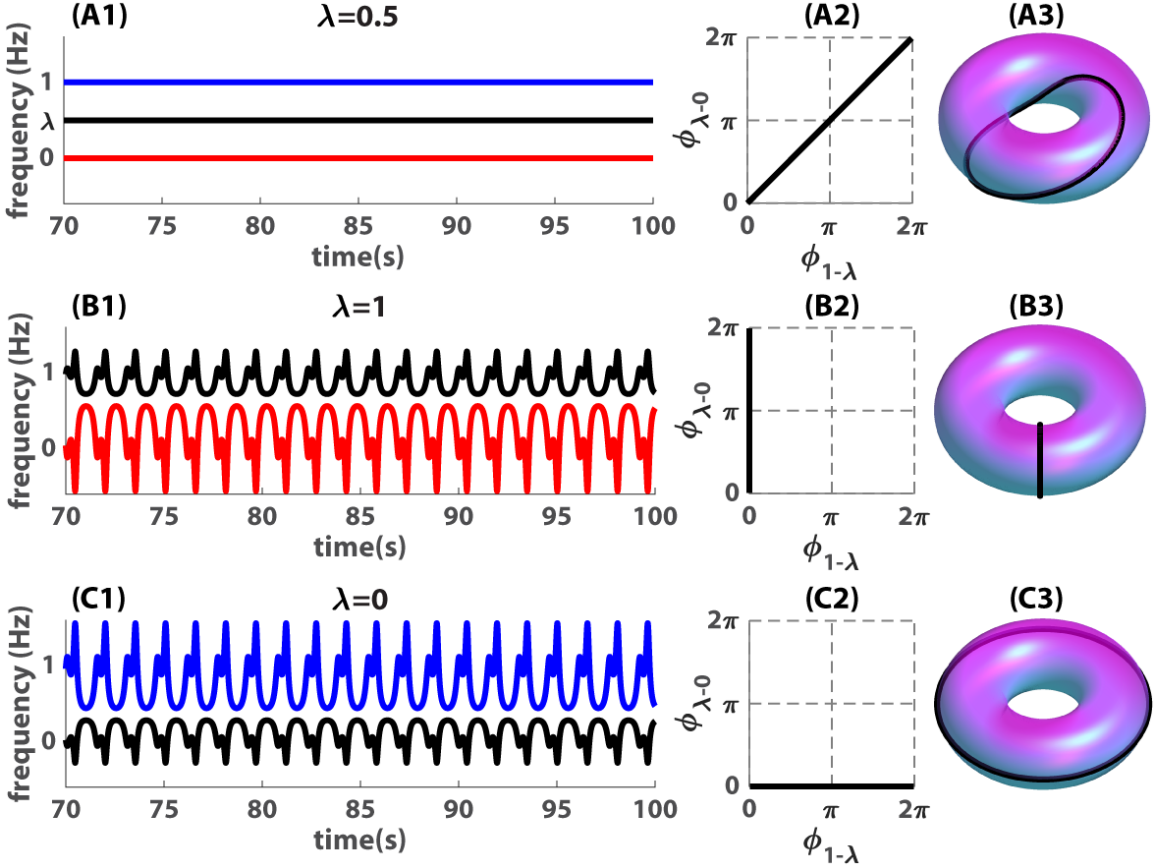


Figure 3.6: Basic forms of triadic metastable coordination. (A1-3) shows the behavior of three *uncoupled* oscillators ($a = b = 0$) with natural frequency 0, $\lambda = 0.5$, and 1 Hz and initial phase $\varphi_i = 0$ for all i 's, as the dynamics of instantaneous frequency (red, black, blue lines in A1; all are constant at their natural frequencies due to the lack of interaction) and the corresponding periodic orbit of relative phases as a loop on a torus (A2-3; the space in A2 has periodic boundaries, i.e. $\{\phi_{1-\lambda} = 0\} \sim \{\phi_{1-\lambda} = 2\pi\}$ and $\{\phi_{\lambda-0} = 0\} \sim \{\phi_{\lambda-0} = 2\pi\}$; A3 is simply a rolled-up version of A2 with the origin in front to better visualize the topology and continuity, but the exact distance in A2 is not preserved). Here two relative phases $\phi_{1-\lambda}$ and $\phi_{\lambda-0}$ increase linearly with time at the same rate because λ is in equal distance with the other two oscillators, resulting in a loop of type (1,1) on the torus (see text). (B1-3) and (C1-3) show corresponding information regarding three *coupled* oscillators with $a = b = 1$, $\lambda = 1$ (B1-3) and $\lambda = 0$ (C1-3). For $\lambda = 1$, the black oscillator (in B1) is completely locked to the oscillator at 1 Hz while coordinating metastably with the red oscillator (trajectories have minimal distance when two oscillators dwell at certain phase relations), with corresponding relative phase orbit of type (0,1) (B2-3); for $\lambda = 0$, the black oscillator is locked to the oscillator at 0 Hz (C1), with corresponding relative phase orbit of type (1,0) (C2-3).

For most values of λ , the relative phase orbit still belongs to the two types above (for $\lambda \in [0.52, 1]$, type (0,1), see Figure 3.6 B2-3 and 3.7 A2-3; for $\lambda \in [0, 0.48]$, type

$(1, 0)$, see Figure 3.6 C2-3 and 3.7 E2-3) despite the deformation and a change in period (seen as fewer cycles in Figure 3.7 A1 and E1 than in Figure 3.6 B1 and C1). Near $\lambda = 0.5$ however, a purely metastable pattern appears, where φ_λ is not phase-locked to either φ_0 or φ_1 (i.e. both relations $\varphi_{1-\lambda}$ and $\varphi_{\lambda-0}$ are metastable; Figure 3.7 C1-3 for $\lambda = 0.5$). The topology of the corresponding relative phase orbit is of type $(1, 1)$ (Figure 3.7 C2-3; one may notice the similarity to Figure 3.6 A2-3. The difference is that only the orbit in Figure 3.7 C2-3 is structurally stable. See Appendix B.9), which is not homotopic to the pattern of either type $(0, 1)$ (A2-3) or $(1, 0)$ (E2-3) studied above, but rather the composition of both (correspondingly, the types follow the relation $(1, 1) = (0, 1) + (1, 0)$). One would immediately ask inductively, whether there is yet another pattern of type $(1, 2) = (0, 1) + (1, 1)$ for some value of λ between 0.52 and 0.5. Such a pattern can indeed be found around $\lambda = 0.5184$ as shown in Figure 3.7 B2-3, which can be easily seen as a composition of (A2-3) and (C2-3) (and symmetrically, for $\lambda = 0.4816$ shown in Figure 3.7 D2-3, a composition of C2-3 and E2-3; see Figure B.10 for more examples of composition). While a formal proof is beyond the scope of the present text, it is reasonable to conjecture that for $\lambda \in (0, 1)$, there are infinitely many purely metastable patterns as structurally stable periodic orbits in $S^1 \times S^1$ with distinct pairs of winding numbers $(p, q) \in \mathbb{Z}^+ \times \mathbb{Z}^+$, belonging to the fundamental group of $S^1 \times S^1$, generated by partially metastable patterns of type $(0, 1)$ and $(1, 0)$ (Figure 3.6 B2-3 and C2-3). This amounts to showing that the Poincaré map associated with this three-oscillator system depends continuously on λ , which connects the conjecture to known results on the rotation number of circle maps (see [139]). In any case, we see multiple types of purely metastable patterns packed within a narrow range of parameter values $\lambda \in [0.48, 0.52]$, where the three oscillators are nearly equidistant to each other in natural frequency (how narrow the range is depends on the coupling strength – greater coupling makes the range narrower until the system is no longer metastable; see Appendix B.9). This ability to reach various

complex metastable patterns under small parameter change is in stark contrast with metastable coordination between two oscillators – more is different [140].

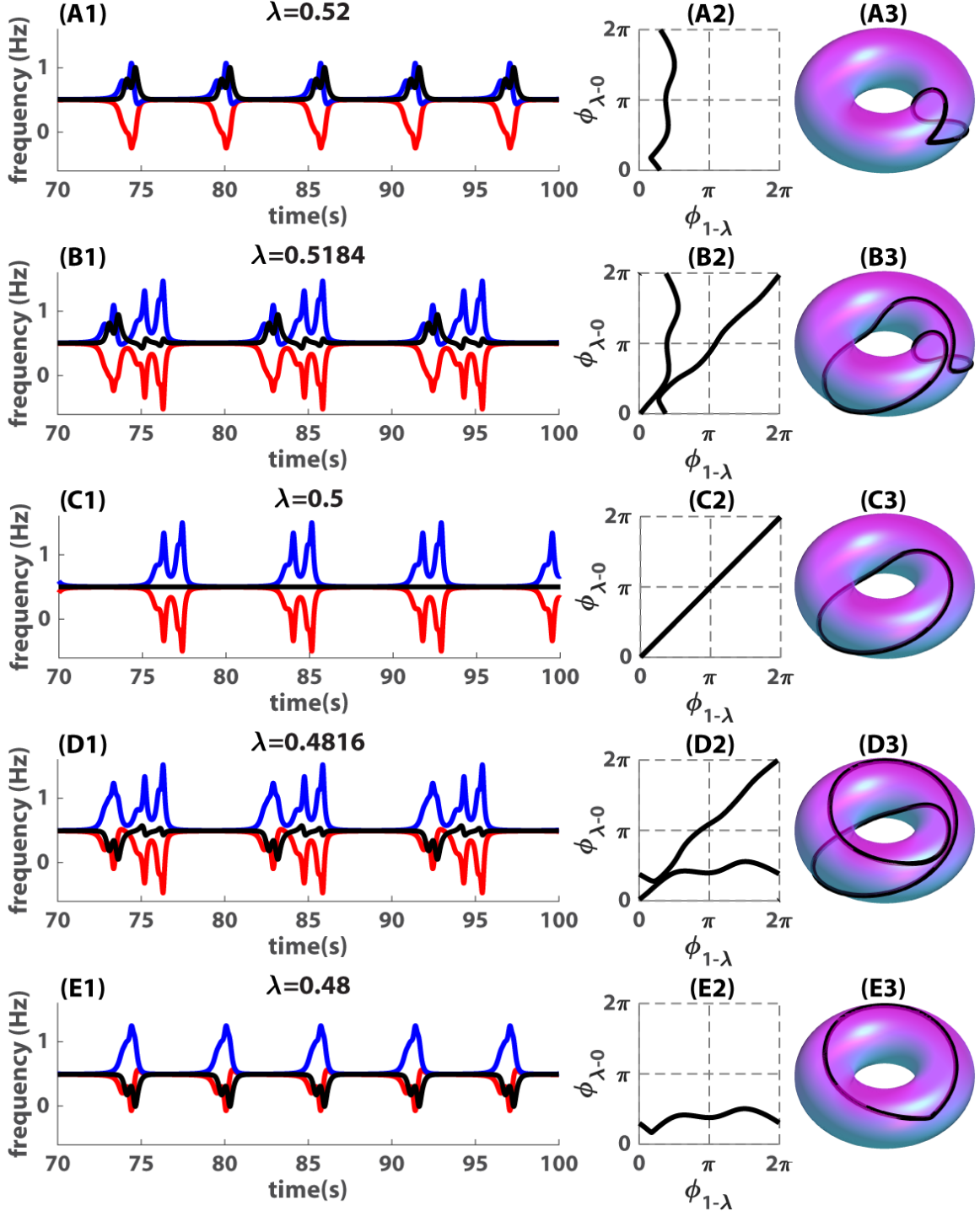


Figure 3.7: Extended forms of triadic metastable coordination. Here we extend the examples given in Figure 3.6 B1-3 and C1-3 with additional values of λ (all other parameters are the same). Within a small parameter range $\lambda \in [0.48, 0.52]$, there are at least five distinct types of relative phase orbits that are not homotopic to each other, i.e. (0, 1) for A2-3, (1, 2) for B2-3, (1, 1) for C2-3, (2, 1) for D2-3, and (1, 0) for E2-3, with corresponding frequency dynamics in A1-E1.

So far we have based our classification on winding numbers, which only give a rough description of patterns. On the other hand, frequency dynamics (Figure 3.7 A1-E1) reflects not only the winding numbers but also additional information about the temporal unfolding of each pattern. Winding numbers are reflected as the clustering of the frequency curves and the relative size of holes between curves (since the integral of frequency difference is exactly the change in relative phase). Frequency dynamics also shows the order in which simple patterns (e.g. Figure 3.7 A1 and C1) are composed into a more complex one (B1) (in Figure 3.7, one cycle in B1 is roughly adding a cycle in A1 in front of a cycle from C1; from Figure B.10, one can see more clearly that this order is not arbitrary) and the overall duration of a pattern (see the difference between Figure 3.6 A1 and 3.7 C1). Thus, metastable patterns can be studied in more details as the geometry of 2D graphs composed of frequency trajectories. This is very convenient when we study higher-dimensional metastable coordination that cannot be visualized on a torus (we devise a computational method that takes advantage of this point in the next chapter). An example is shown below.

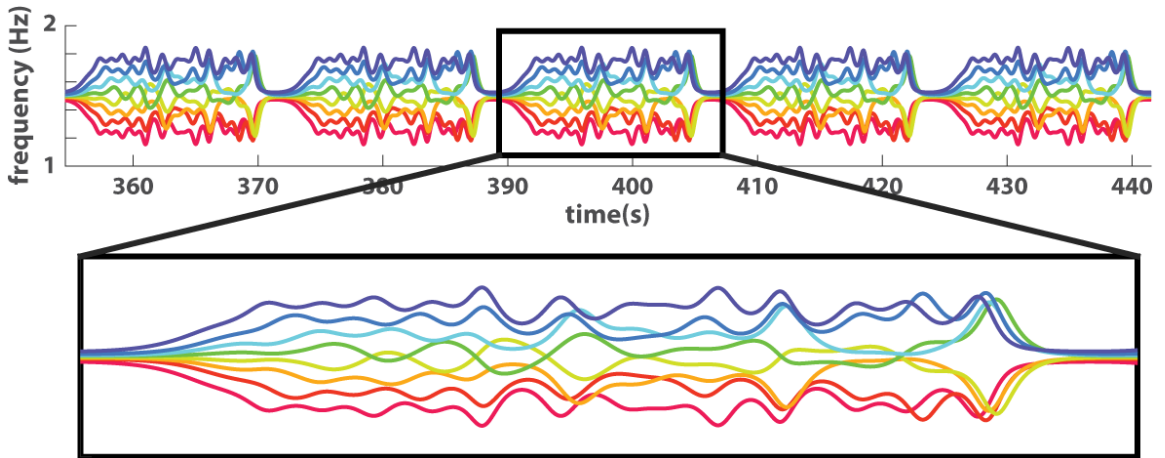


Figure 3.8: An example of eight-agent metastable coordination, with coupling $a = b = 0.15$, average natural frequency $\bar{\omega} = 1.5$ Hz, and difference between adjacent oscillators $\delta\omega_{i+1,i} = 0.075$ Hz, shown as frequency trajectories. One period of the metastable pattern is enlarged in the black box under the time axis. The winding numbers of relative phases between adjacent oscillators is $(1, 1, 1, 1, 1, 1, 1)$.

Figure 3.8 shows a metastable pattern (repeated for five cycles) formed by eight oscillators as a complex shape composed of frequency trajectories. Trajectories fan out separately at the beginning of each cycle but return as two clusters at the end, and in between form various organizations. The complexity of this pattern cannot be fully described by the winding numbers alone, i.e. $(1, 1, 1, 1, 1, 1, 1)$. In fact, the winding numbers only provide a geometric constraint on the area of empty space between curves. While a systematic geometric study of multiagent metastable patterns has to be left to the future, this example gives a taste of how complex and, nevertheless, ordered dynamic patterns can be generated without synchronization.

3.3 DISCUSSION

The present model is a natural generalization of the extended HKB (for $N = 2$) [13] to higher dimensions (arbitrary N) and an extension of the classical Kuramoto model (for large N) [12] to include second-order coupling, thereby reconciling small-scale and large-scale theories of coordination. The model successfully captures key features of multiagent coordination in mid-scale ensembles at multiple levels of description [35]. Similar to the HKB model [27], second-order coupling is demanded by the experimental observation of antiphase (and associated multistability) but now in eight-person coordination; and similar to the extended HKB [13], the model captures how increasing frequency difference δf weakens inphase and antiphase patterns, leading to segregation but now between two groups instead of two persons. This cross-scale consistency of experimental observations may be explained by the scale-invariant nature of the critical coupling ratio $\kappa_c = 1$, the transition point between monostability (only an all-inphase state) and multistability (states containing any number of antiphase patterns). The scale invariance suggests that experimental methods and conclusions for small-scale coordination dynamics have implications for multistability, phase transitions, and metastability at larger scales, and enables a unified approach

to coordination that meshes statistical mechanics and nonlinear dynamics.

Another generalization of the classical Kuramoto model by Hong and Strogatz [141] also allows for antiphase-containing patterns (“ π -state”) by letting the sign of the first order coupling (a) be positive for some oscillators (“the conformists”) and negative for others (“the contrarians”). However, in contrast to our model, antiphase induced this way does not come with multistability, nor the associated order-to-order transitions observed in human rhythmic coordination [28, 142]. The second-order coupling in our model allows each individual to be *both* a conformist *and* a contrarian but possibly to different degrees [37]. The simple addition of a second stable state may not seem like a big plus at $N = 2$ (2 stable states), but it rapidly expands the system’s behavioral repertoire as the system becomes larger (2^{N-1} stable states for N oscillators; with only first-order coupling, the system always has $1^{N-1} = 1$ stable state, and therefore does not benefit from scaling up). This benefit of scale may be how micro-level multistability contributes to the functional complexity of biological systems [32, 143].

Besides the multistability of micro patterns (a general feature endowed by higher-order coupling [20, 22, 144]), the addition of second-order coupling also affects macro-level order in terms of critical scaling (see [72] for a summary), i.e. for coupling strength $K > K_c$ near K_c , the order parameter $\|H\|$ (norm of the order function [145]) is proportional to $(K - K_c)^\beta$, with $\beta = 1/2$ for the classical Kuramoto model and $\beta = 1$ when second-order coupling is added [146, 147]. For complex biological systems like the brain which seem to operate near criticality [148], these two types of scaling behavior have very different functional implications. When modeling such complex systems, one may want to have a closer examination or re-examination of empirical data of large-scale coordination near the critical point, and preferably at multiple levels of description [115].

Building upon the mathematical context of stationary solutions, we have to recall

that spontaneous social coordination is highly metastable (e.g. Figure 3.2A-C) [35], captured by the model when frequency diversity is combined with weak coupling (e.g. Figure B.1A, in contrast to BC under stronger coupling). Individuals did not become phase-locked in long run, but dwell temporarily when passing by a preferred relation (inphase and antiphase) [32, 33] (e.g. red trajectory in Figure 3.5A; note here stability analysis of stationary solutions provides landmarks for characterizing metastable patterns). For $N > 2$, an ensemble can visit different spatial organizations sequentially (see examples of human behavior in [35], model behavior Figure B.10), forming complex patterns that extend in both space and time (e.g. Figure 3.8). Remarkably, the kind of order present in metastable patterns (as demonstrated in Sections 3.2.6 and B.9) are achieved without unison (i.e. synchronization) or reducing the behavioral complexity of individual agents. To the contrary, individual oscillators gain complex behaviors by participating in metastable collective patterns, who are rather boring when left alone (see contrast between Figure 3.6A1 and Figure 3.7B1). For these reasons, metastability makes a viable mechanism for encoding complex information as real-world complex living systems do (e.g. a brain) [28, 33, 115, 131, 149–151]. In the brain, highly coherent patterns like collective synchronization can be less functional and even pathological [152, 153]. Our results call for more attention to these not-quite coherent but empirically relevant patterns of coordination.

Key experimental observations are captured by our model under the assumptions of uniform coupling (everyone couples with each other in the same way) and constant natural frequency. However these assumptions may be loosened to reflect detailed dynamics. For example, introducing individual differences in coupling style (equation (3.5)) gives more room to explain how one metastable phase relation may exert strong influence on another (Figure 3.5A). Long time-scale dynamics observed in the experiment (see Section B.8 in Appendix B) may also be explained by frequency adaptation, which has been observed in dyadic social coordination [154]. A systematic study of

the consequences of asymmetric coupling and frequency adaptation on coordination among multiple agents seems worthy of further experimental and theoretical exploration.

To conclude, we proposed a model that captured key features of human social coordination in mid-sized ensembles [35], and at the same time connected well-studied large-scale and small-scale models of coordination. The model provides mechanistic explanations of the statistics and dynamics already observed, as well as a road map for future empirical exploration. As an experimental-theoretical platform for understanding biological coordination, the value of the middle scale should not be underestimated, nor the importance of examining coordination phenomena at multiple levels of description.

3.4 MATERIALS AND METHODS

3.4.1 Methods of the human experiment

A complete description of the methods of the “Human Firefly” experiment can be found in [35]. Here we only recapitulate a few points necessary for understanding the present paper. For an ensemble of eight people (120 subjects in total), each subject was equipped with a touchpad that recorded his/her tapping behavior as a series of zeros and ones at 250 Hz (1=touch, 0=detach), and an array of eight LEDs arranged in a ring, each of which flashed when a particular subject tapped. For each trial, subjects were first paced with metronomes for 10s, later interacting with each other for 50s (instructed to maintain metronome frequency while looking at others’ taps as flashes of the LEDs). Between the pacing and interaction period, there was a 3s transient, during which subjects tapped by themselves. Tapping frequency during this transient has been used to estimate the “natural frequencies” of the subjects (see Estimating the distribution of natural frequencies). During pacing, four subjects received the same metronome (same frequency, random initial phase), and the other

four another metronome. The metronome assignments created two frequency groups (say, group A and B) with intergroup difference $\delta f = |f_A - f_B| = 0, 0.3$, or 0.6 Hz (same average $(f_A + f_B)/2 = 1.5$ Hz). From a single subject's perspective, the LED array looks like the legend of Figure 3.2A (all LEDs emit white light; color-coding only for labeling locations): a subject always saw his/her own taps as the flashes of LED 1, members of his/her own frequency group LED 2-4, and members of the other group LED 5-8 (members from two groups were interleaved to preserve spatial symmetry).

From the tapping data (rectangular waves of zeros and ones), we obtained the onset of each tap, from which we calculated instantaneous frequency and phase. Instantaneous frequency is the reciprocal of the interval between two consecutive taps. Phase (φ) is calculated by assigning the onset of the n th tap phase $2\pi(n - 1)$, then interpolating the phase between onsets with a cubic spline.

3.4.2 Estimating the distribution of natural frequencies

Human subjects have variable capability to match the metronome frequency and maintain it, which in turn affects how they coordinate. To reflect this kind of variability in the simulations, the oscillators' natural frequencies were drawn from a probability distribution around the “metronome frequency” (central frequencies f_A and f_B for groups A and B). To estimate this distribution from human data, we first approximated the “natural frequency” of each subject in each trial with the average tapping frequency during the transient between pacing and interaction periods (see Methods of the human experiment), and subtracted from it the metronome frequency (see blue histogram in Figure B.2 from the “Human Firefly” experiment [35]). We then estimated the distribution non-parametrically, with a *kernel density estimator* in the form of

$$\hat{P}(x) = \frac{1}{nh} \sum_{i=1}^n K\left(\frac{x - x_i}{h}\right) \quad (3.6)$$

where the *Kernel Smoothing Function* is Normal, $K(y) = \frac{1}{\sqrt{2\pi}} e^{-\frac{y^2}{2}}$. Here $n = 2048$ (256 trials \times 8 subjects) from the experiment. We choose the bandwidth $h = 0.0219$, which is optimal for a normal density function according to [155],

$$h = \left(\frac{4}{3n}\right)^{1/5} \sigma \quad (3.7)$$

where σ is the measure of dispersion, estimated by

$$\tilde{\sigma} = \text{median}\{|y_i - \text{median}\{y_i\}|\}/0.6745 \quad (3.8)$$

where y_i 's are samples [156]. The result of the estimation is shown in Figure B.2 (red curve).

3.4.3 Phase-locking value and level of integration

The (short-windowed) phase-locking value (PLV) between two oscillators (say x and y) during a trial is defined as

$$PLV_{xy} = \frac{1}{W} \sum_{w=1}^W \frac{1}{M} \left| \sum_{m=1}^M \exp(i\phi_{xy}[(w-1)M + m]) \right| \quad (3.9)$$

where $\phi_{xy} = \varphi_x - \varphi_y$, W is the number of windows which each ϕ trajectory is split into, and M is number of samples in each window (in the present study, $W = 16$ and $M = 750$, same as [35]).

Intragroup PLV (PLV_{intra}) is defined as

$$PLV_{intra} = \left(\binom{|A|}{2} + \binom{|B|}{2} \right)^{-1} \left(\sum_{x,y \in A} PLV_{xy} + \sum_{x,y \in B} PLV_{xy} \right) \quad (3.10)$$

where A and B are two frequency groups of four oscillators, corresponding to the design of the “Human Firefly” experiment [35], $A = \{1, 2, 3, 4\}$, $B = \{5, 6, 7, 8\}$, and $|A| = |B| = 4$.

Intergroup PLV (PLV_{inter}) is defined as

$$PLV_{inter} = \frac{1}{|A||B|} \sum_{x \in A, y \in B} PLV_{xy}. \quad (3.11)$$

In both the human and simulated data, comparisons of PLV_{intra} and PLV_{inter} for different levels of δf were done using two-way ANOVA with Type III Sums of Squares, and Tukey Honest Significant Difference tests for post-hoc comparisons (shown in Figure 3.3BD).

The level of integration between two frequency groups is measured by the relationship between intragroup coordination (measured by PLV_{intra}) and intergroup coordination (measured by PLV_{inter}). The groups are said to be *integrated* if intragroup coordination is positively related to intergroup coordination, and *segregated* if negatively related. Quantitatively, for each combination of intergroup difference δf and coupling strength a (assuming $a = b$ for our model, assuming $b = 0$ for the classical Kuramoto model), we use linear regression

$$PLV_{inter,k}^{(\delta f, a)} = \beta_0^{(\delta f, a)} + \beta_1^{(\delta f, a)} PLV_{intra,k}^{(\delta f, a)} + error_k^{(\delta f, a)} \quad (3.12)$$

where $PLV_{,k}^{(\delta f, a)}$ is the inter/intra-group PLV for the k th trial simulated with the parameter pair $(\delta f, a)$, and the slope of the regression line $\beta_1^{(\delta f, a)}$ is the measure of *level of integration* between groups. If $\beta_1 > 0$, the groups may be said to be integrated; if $\beta_1 < 0$, segregated. The set $\{(\delta f, a) | \beta_1^{(\delta f, a)} = 0\}$ is the *critical boundary* between the domains of integration and segregation.

3.4.4 Method of simulation

All simulations were done using the Runge-Kutta 4th-order integration scheme, with a fixed time step $\Delta t = 0.004$ for duration $T = 50$ (matching the sampling interval and the duration of interaction period of the human experiment [35]; second may be used as unit), i.e. for system $\dot{X} = f(X)$, with initial condition $X(0) = X_0$, the $(n + 1)$ th sample of the numeric solution can be solved recursively

$$X[n + 1] = X[n] + \frac{1}{6}(k_1 + 2k_2 + 2k_3 + k_4) \quad (3.13)$$

where

$$k_1 = \Delta t f(X[n]) \quad (3.14)$$

$$k_2 = \Delta t f(X[n] + k_1/2) \quad (3.15)$$

$$k_3 = \Delta t f(X[n] + k_2/2) \quad (3.16)$$

$$k_4 = \Delta t f(X[n] + k_3). \quad (3.17)$$

The solver was implemented in CUDA C++, ran on a NVIDIA graphics processing unit, solving every 200 trials in parallel for each parameter pair $(\delta f, a)$. For each trial, initial phases were drawn randomly from a uniform distribution and natural frequencies the distribution defined by equation (3.7). Here 200 trials are used per condition, greater than that of the human experiment [35] to obtain a more accurate estimate of the mean.

CHAPTER 4

TOPOLOGICAL ANALYSIS OF MULTIAGENT METASTABLE COORDINATION

In the preceding chapters, statistical analyses of the Human Firefly experiment [35] have primarily been time-independent, although we have complemented these statistical results with example dynamics. This is in part due to a lack of well-suited tools for characterizing complex spatiotemporal patterns and detecting pattern switching in high-dimensional nonlinear dynamical systems. Regarding coupled oscillators, complex spatiotemporal patterns emerge during metastable coordination between multiple agents (i.e. agents coordinate intermittently with each other at certain phase relations; see Sections 2.2.1 and 3.2.6). In contrast to dyadic metastable coordination, whose spatiotemporal scale is unique for fixed boundary conditions, multiagent metastable coordination allows different spatial and temporal scales to coexist, due to the addition of spatial components (see Section 3.2.6). Multiagent metastable patterns are thus unlikely to be distinguished by a single scalar at a particular level of description (e.g. one single order parameter at the statistical level). On the other hand, because the state space is high-dimensional and often sparsely covered by data, it is also unlikely to find structures in the dynamics by taking into account every micro-level detail. In other words, some statistics or dimensionality reduction has to be done. Here we explore the utility of tools from computational algebraic topology for such (nonlinear) dimensionality reduction. With these tools, it is possible to keep track of topological features in the coordination patterns instead of the state variables themselves.

In the following sections, we center our discussion around two examples of single

trial dynamics reported in [35] for proof of concept. In Section 4.1, the original dynamics is given and the utility of traditional state-based recurrence plots is discussed. In Section 4.2, a topology-based method is introduced for detecting structures in the dynamics. The results of applying this topology-based method on the examples are shown in Section 4.3 and discussed in Section 4.4.

4.1 EXAMPLES OF COORDINATION DYNAMICS

In this section, we show the original dynamics of two example trials – one involves three interacting agents, the other eight – from the Human Firefly experiment [35] (also see Chapter 2). By contrasting these two examples, we want to demonstrate what problems arise with traditional methods when the number and diversity of agents are increased in the coordination dynamics.

We begin with the three-agent example (Figure 4.1), which is easily interpretable visually. In Figure 4.1A, coordination among three agents (1, 3, 4) are shown in terms of two phase relations (1-3 magenta, and 3-4 orange). From 10s to 40s, the system visited recurrently an all-inphase pattern (marked by 3 black triangles; between the triangles, only 3-4 are inphase, with agent 1 wrapping), before switching to an inphase-antiphase pattern around 40s (1-3 inphase, 3-4 antiphase in Figure 4.1A; due to a sudden slowing down of agent 3, orange trajectory around 40s in Figure 4.1B; frequency is the time derivative the phase). The ease of interpretation comes from the facts that the number of interacting agents is small (low-dimensionality) and that they are close in frequency (Figure 4.1B), as a result of which their phase coordination occurs on visually comparable time scales.

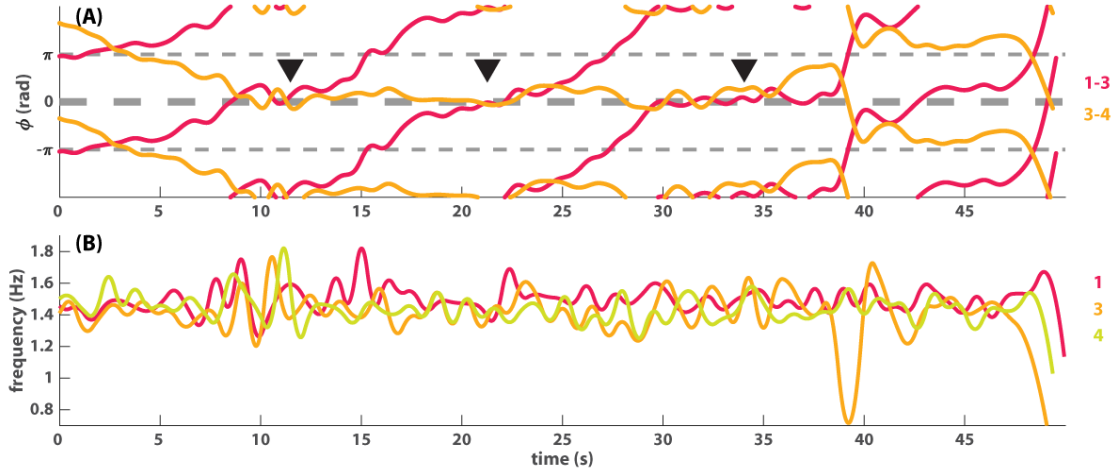


Figure 4.1: An example of triadic coordination dynamics. Coordination among three agents (labeled as 1, 3, and 4) is shown as the dynamics of two pair-wise relative phases (A) and three instantaneous frequency trajectories (B). Around 10s, three agents formed an all-inphase relation ($\phi_{1,3} \approx \phi_{3,4} \approx 0$ rad) for a few seconds, marked by a black triangle on the left in (A). This pattern recurred intermittently two more times (middle, right triangle in A), which ended when pair 3-4 switched to antiphase (40-48s, orange trajectory $\phi_{3,4} \approx \pi$ rad). Both relative phase trajectories (A) evolve on a slow time scale because the frequency of these three agents are very close (B).

This ease of analysis is lost when more interacting agents and frequency diversity are involved, as illustrated in the eight-agent example (Figure 4.2). The dynamics of pairwise relative phases (Figure 4.2A) is much less intelligible now that they are evolving at very different time scales, e.g. slow dynamics for pairs 3-2, 5-7, and 6-8 (thickened trajectories, mostly horizontal, reflecting strong phase coordination) in contrast to fast dynamics for other pairs (thin trajectories, mostly wrapping, i.e. with a steep slope). It is also not clear how these multiple phase relations constrain each other in forming higher-level structures. The frequency dynamics (Figure 4.2B) is more informative regarding the overall trend in the organization (e.g. eight agents were separated into two frequency groups at the beginning, coded in warm vs. cold colors, and became entangled at the end), but not much about how phase relations formed or changed in relation to the overall trend. This kind of multiagent dynamics

involving multiple spatiotemporal scales requires additional computational tools for characterizing coordination patterns and detecting pattern transitions.

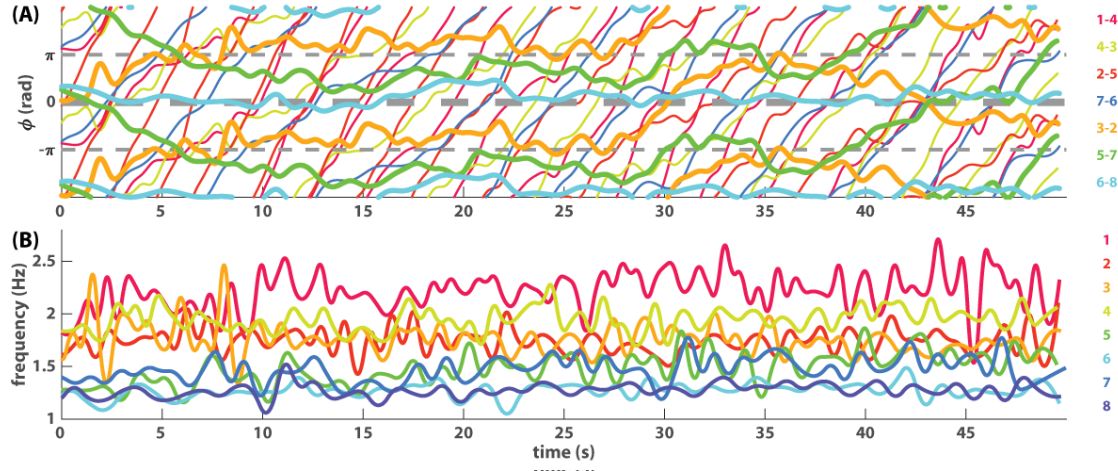


Figure 4.2: An example of eight-agent coordination dynamics shown as seven pair-wise relative phases (A) and eight instantaneous frequency trajectories (B). In (A), slowly varying phase relations are shown as thick lines (orange trajectory 3-2, green 5-7, cyan 6-8), whereas fast varying phase relations are shown as thin lines (with much steeper slopes than the thick lines). In (B), the corresponding frequency trajectories indicate that the frequency diversity is much greater than in Figure 4.1B. The ensemble of eight started with two frequency groups (under the experimental condition of intergroup difference $\delta f = 0.6$ Hz), one in warm colors (1, 2, 3, 4) and one in cold colors (5, 6, 7, 8). But toward the end of the trial, members from the two groups begin to mingle.

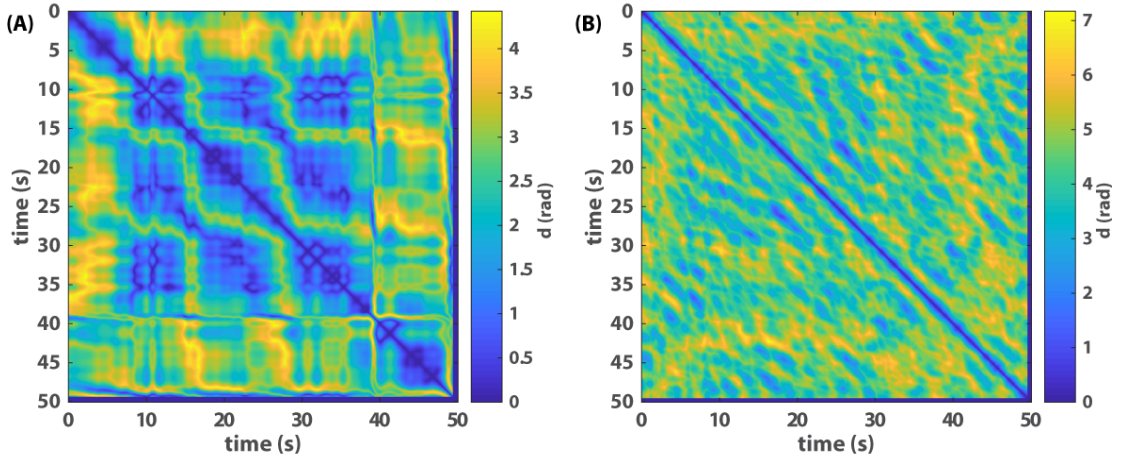


Figure 4.3: Recurrence plots of relative phase dynamics. (A) shows the recurrence of phase relations among the three agents (the state variable is a vector with 2 relative phases shown in Figure 4.1A as components) and (B) that of the eight agents (the state variable is a vector with 7 relative phases in Figure 4.2A as components).

Recurrence plot [157,158] is a powerful tool for visualizing and analyzing patterns of nonlinear dynamical systems, especially when the state space itself is too high-dimensional to visualize. Rather than showing the state variable per se, it shows the relation between states at different points in time, e.g. as a distance matrix, from which one can infer how frequently a system visit different points in the state space. In Figure 4.3AB, we show the recurrence plots of the two examples above in terms of the state variable $\vec{\phi}(t)$, whose components are relative phases shown in Figure 4.1A and 4.2A respectively (the components of the distance matrices are defined as

$$d_{t_1, t_2} = \|W(\vec{\phi}(t_1) - \vec{\phi}(t_2))\| \quad (4.1)$$

where function W wraps each component to the interval $(-\pi, \pi]$ and $\|\cdot\|$ is the L_2 -norm). The recurrence of relative phases clearly captures the structure of the triadic coordination (Figure 4.3A; a 3-by-3 grid between 10 and 40s, reflecting the main recurrent pattern; the blocks before 10s and after 40s reflect two other patterns), but does not reveal much structure in the eight-agent case (Figure 4.3B). This

illustrates that conventional recurrence plots which work for low-dimensional coordination dynamics may not work well for high-dimensional dynamics involving multiple spatiotemporal scales. In order to shed more light on the eight-agent example, we next present a method for constructing a new type of recurrence plot, which quantifies the recurrence of topological features (e.g. connected components and loops) in the coordination patterns across multiple scales.

4.2 METHOD OF TOPOLOGICAL ANALYSIS

As shown in Section 3.2.6, multiagent metastable patterns can be classified by their topological and geometric features. The method presented hereafter aims to identify changes of topological features in multiagent coordination patterns as a way to detect phase transitions. To do so, we need to first transform the original data into a sequence of point clouds, each representing the coordination pattern at a particular time (Section 4.2.1), then compute the topological portraits (i.e. persistent homology) of each point cloud and compare these portraits across time (Section 4.2.2).

4.2.1 Coordination patterns as point clouds

For a point cloud to represent a coordination pattern, the distance between points has to capture essential aspects of coordination between agents. The behavioral dynamics of N agents was initially represented as N time series of absolute phases (φ_i for integer $0 < i \leq N$). However, a small distance in phase (i.e. relative phase near zero) does not necessarily imply coordination (phases may coincide frequently between oscillators of very different natural frequencies, i.e. even a broken clock is right twice a day), and conversely, coordination does not necessarily imply small distance in phase (since coordination can happen at π or other relative phases as shown in Chapter 2 and 3).

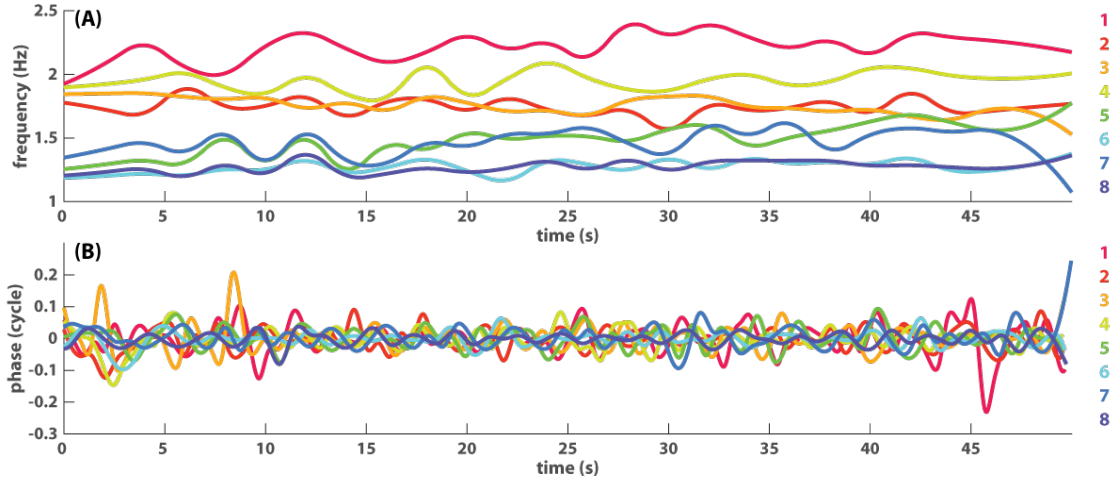


Figure 4.4: Decomposition of absolute phase dynamics for the eight-agent example. The absolute phase of each agent is decomposed into a slowly varying frequency component (A) and a fast varying residual phase (B) (this type of decomposition is well-known in coupled oscillator theory, see e.g. [159]).

A more reasonable way to represent coordination patterns is by instantaneous frequency (Figure 4.1B, 4.2B) – the time derivative of absolute phase. Whenever there is phase coordination, the derivative of the relative phase must be small (e.g. ϕ trajectories flattening in Figure 4.1A), hence the instantaneous frequency of two agents approaches each other. During sudden transitions, however, instantaneous frequencies may oscillate with a high amplitude, approaching each other without coordinating. To resolve this ambiguity (i.e. closeness in instantaneous frequency due to actual coordination or fluctuations near a transition), we decompose the absolute phase of each agent into a slowly varying frequency component (e.g. Figure 4.4A for the eight-agent example) and a fast varying residual phase (phase for short in Figure 4.4B) without losing any information (i.e. absolute phase can be restored by $\varphi = 2\pi (\text{frequency}(t) \cdot t + \text{phase}(t))$). To do so, we first fit a piece-wise cubic spline ($\hat{\varphi}$) to the absolute phase (φ) (least-square, using `splinefit` in Matlab with robust fitting parameter $\beta = 0.5$ [160]). Knots of the spline were chosen at 2s intervals, based on the observation that dyadic phase coordination mostly exceeded 2s (about

87%, see distribution in Fig B of S1 File in [35]). The slow component (frequency) is the derivative of $\hat{\varphi}$ and the fast component (residual phase) is $\varphi - \hat{\varphi}$.

Finally, time series of these two components are segmented into 2s windows (consecutive windows overlap by 1s) and the coordination pattern around time t (s) is represented as a point cloud in 3-dimensional space – a set of M points whose coordinates correspond to local time, residual phase, and frequency respectively (we will see an example later in Figure 4.7A, where each point in the point cloud is shown as a small ball; $M = 160$ for this study, containing 20 time points for each of the eight agents, centered at 0.1s intervals), i.e. $X(t) = \{x_1(t), \dots, x_i(t), \dots, x_M(t)\}$ where $x_i(t) \in U_t = I_t \times S^1 \times \mathbb{R}^+$ with $I_t = [t - w/2, t + w/2]$ for a coordination pattern sampled at time t (s) in a window of $w = 2$ (s). To later compute the topological features associated with each point cloud $X(t)$, we need to equip the space U_t with a metric, i.e. the distance between any point $a = (a_1, a_2, a_3)^\top$ and $b = (b_1, b_2, b_3)^\top \in U_t$,

$$d(a, b) = \|(a_1 - b_1, W(a_2 - b_2), a_3 - b_3)^\top\| \quad (4.2)$$

where

$$W(a) = \begin{cases} a & |a| \leq 0.5 \\ 1 - a & \text{otherwise} \end{cases}. \quad (4.3)$$

Here the three dimensions of U_t have different units, so in principle, one can rescale each dimension by modifying the metric. Nevertheless, they are not independent, i.e. [second][cycle][cycle/second], thus cannot be scaled arbitrarily. The most natural choice is to have no scaling, which is adopted in the present study.

In general, one may customize the representation based on the nature of agent behavior (e.g. rhythmic or non-rhythmic) and the type of coordination of interest (e.g. phase coordination in the present case). But as long as a sequence of point clouds are properly constructed to reflect the patterns of interest, the following section provides a potential method to reveal structures in the dynamics via topological data analysis.

4.2.2 Multiscale topological portraits and their dynamics

In this section, we show how to compute topological portraits for each coordination pattern and to study the dynamics of such portraits. The goal is to detect sudden topological transitions in the coordination patterns, allowing us to return to the original time series to study the nature of such transitions. Persistent homology is the basis of our analyses. We will first give an intuitive description of what persistent homology is and why it is useful for understanding complex metastable coordination, before filling in with necessary technical details (for a formal account of homology, see [161], and persistent homology, see [162–164]).

Homology captures fundamental topological features of a structure like connected components, loops, cavities, and their higher-dimensional analogues (“holes” of different dimensions). Persistent homology keeps track of these features across scales. It was initially conceived to distinguish the correct topological features of a sampled structure (e.g. the number of connected components and loops of a torus) from noise, since correct features are more persistent across scales [165]. In the present study, we are interested in *multiscale coordinative structures*, where the set of “correct” features may vary with scale. A figurative example is given in Figure 4.5, which can be seen as a structure of 19 connected components and 19 loops (from 19 A’s) at one scale, or 1 connected component and 2 loops (from 1 B) at a grosser scale (commonly used to study human local/global perception [166]). The point is not to determine whether one set of features is more correct than the other, but rather to combine these two levels of description to obtain a more complete picture of the structure. As for metastable coordination patterns (as constructed per Section 4.2.1), agents form (approximately) connected components during phase coordination and form loops due to the recurrent nature of metastable coordination (see behavior of agent 2, 3, 4 in Figure 4.4A) – features that can be suitably described by homology. Moreover, as discussed in Section 4.1 and previous chapters, multiagent metastable patterns pos-

sess interesting features across multiple spatiotemporal scales, which maybe elusive to traditional tools but can be captured by the persistence of homological features.



Figure 4.5: A letter B made up of many A's. Topologically, a "A" is one connected component with one loop and a "B" is one connected component with two loops. At a fine scale, this figure may be said to have 19 connected components and 19 loops; or at a gross scale, it may be said to have 1 connected component and 2 loops. A complete description of this figure needs to embrace both scales.

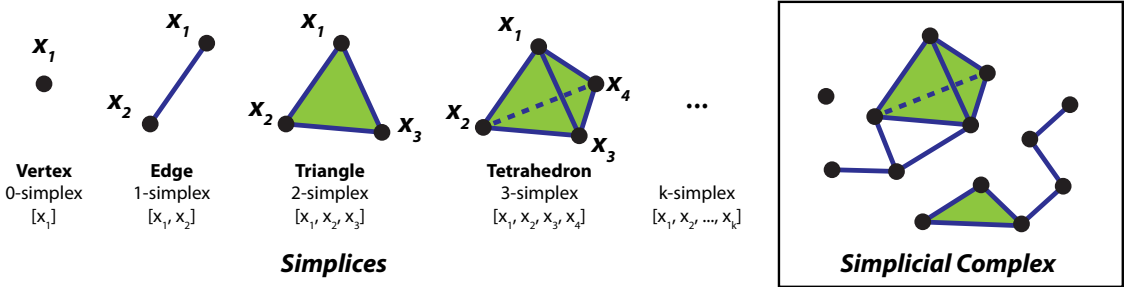


Figure 4.6: Simplices and a simplicial complex. Simplices are elementary geometric objects of different dimensionality, which can be combined into more complex structures, i.e. simplicial complexes. A k -simplex can be thought of as a k -dimensional triangle, determined by its $(k+1)$ vertices. For example, a 2-simplex is a conventional triangle, determined by three vertices $[x_1, x_2, x_3]$, a 0-simplex a vertex determined by itself $[x_1]$, and a 1-simplex an edge determined by two vertices $[x_1, x_2]$. A simplicial complex therefore can be described combinatorially as a set of vertices plus a collection of its subsets (higher-dimensional simplices connecting those vertices).

A coordination pattern (point cloud) $X = \{x_1, \dots, x_M\}$ measured at a specific scale ϵ refers to a union of balls centered at each point in X (e.g. Figure 4.7A-C), i.e. $X_\epsilon = \bigcup_{i=1}^M B_{\epsilon/2}(x_i)$. Our goal is to identify independent homological features ("holes") in X_ϵ and record how they vary (e.g. emerge or disappear) with scale ϵ (diameter of balls). To compute these features algebraically, we first need to triangulate the structure X_ϵ into a *simplicial complex*. The building blocks of a simplicial complex

are *simplices*, which can be thought of as generalized triangles (Figure 4.6), i.e. a k -simplex is a k -dimensional triangle defined by its $(k+1)$ vertices. A familiar example is a network, which is a simplicial complex containing only 0- and 1-simplices (i.e. vertices and edges). In the present study, we construct the *Rips complex* $R_\epsilon(X)$ [167] for each pattern X at scale ϵ . $R_\epsilon(X)$ is an abstract simplicial complex consisting of all points in X as its vertices and any k -simplex whose vertices are within ϵ distance with each other (distance as defined in equation 4.2). $R_\epsilon(X)$ approximates the topological structure of X_ϵ , which is less accurate than its topologically faithful counterparts (e.g. a *Čech complex* [168]), but much more economical computationally and thus adopted in the present method (see [169] regarding how Rips and Čech complexes are related).

Now our task amounts to finding the “holes” in $R_\epsilon(X)$. A hole is simply some empty space surrounded by a closed chain of geometrical elements. In other words, a k -dimensional hole can be identified by a *cycle* formed by a chain of k -simplices (or a k -*cycle*) that is not the *boundary* of any $(k+1)$ -simplex. To compute these holes algebraically, we represent a simplicial complex as a sequence of chain groups C_k (chains generated by k -simplices of $R_\epsilon(X)$, or k -chains),

$$\cdots C_{k+1} \xrightarrow{\partial_{k+1}} C_k \xrightarrow{\partial_k} C_{k-1} \rightarrow \cdots \rightarrow C_2 \xrightarrow{\partial_2} C_1 \xrightarrow{\partial_1} C_0 \xrightarrow{\partial_0} 0 \quad (4.4)$$

where a *boundary operator* ∂_{k+1} maps $(k+1)$ -simplices to their boundaries, which are k -cycles that do not enclose any hole. Any k -*cycle*, say γ , per se has no boundary, i.e. $\partial_k \gamma = 0$. To find the holes, one simply “removes” the boundaries (image of ∂_{k+1}) from the collection of all cycles (kernel of ∂_k),

$$H_k = \ker \partial_k / \text{Im } \partial_{k+1} \quad (4.5)$$

where H_k is the k^{th} *homology group* of the simplicial complex (or to be scale-specific, H_k^ϵ of $R_\epsilon(X)$) and its generators capture independent k -dimensional holes.

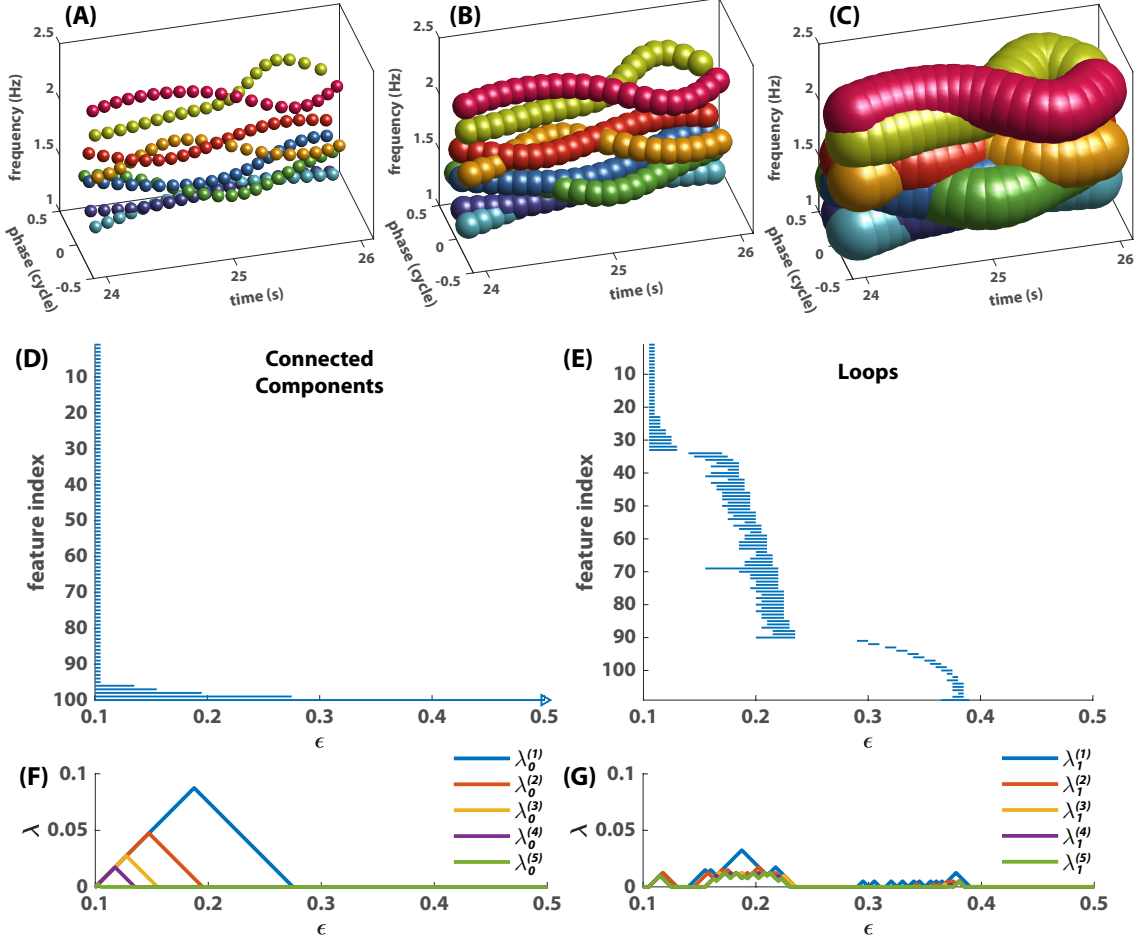


Figure 4.7: Persistence of topological features. (A-C) shows a coordination pattern (point cloud) represented at three different scales ϵ , i.e. a union of balls with diameter $\epsilon = 0.1$ (A), 0.2 (B), or 0.5 (C) centered at each point. The 0th and 1st persistent homology (connected components and loops respectively) of this point cloud is shown in (D,E) as barcodes and in (F,G) as persistence landscapes. In (D,E), each horizontal bar represents a connected component (D) or loop (E), whose left (right) end indicates its birth (death) scale. Right arrow in (D) indicates that this component never dies (one connected component remains at any scale). (F,G) summarize the same information as a sequence of landscape functions (λ), reflecting the most to least prominent homological features across scales (blue to green lines are the five largest landscape functions).

Persistent homology keeps track of each independent k -dimensional hole, which may emerge at any scale, throughout its life span across scales. It concerns a family of simplicial complexes R_{ϵ_i} (equation 4.6), capturing the topology of pattern X from

finer to grosser scales ($0 \leq \epsilon_i < \epsilon_{i+1}$ for any index $0 \leq i < P - 1$),

$$R_{\epsilon_0}(X) \subseteq R_{\epsilon_1}(X) \subseteq \cdots \subseteq R_{\epsilon_{i-1}}(X) \subseteq R_{\epsilon_i}(X) \subseteq R_{\epsilon_{i+1}}(X) \subseteq \cdots \subseteq R_{\epsilon_P}(X) \quad (4.6)$$

$$\{C_k^{\epsilon_0}\} \xrightarrow{f^0} \{C_k^{\epsilon_1}\} \xrightarrow{f^1} \cdots \rightarrow \{C_k^{\epsilon_{i-1}}\} \xrightarrow{f^{i-1}} \{C_k^{\epsilon_i}\} \xrightarrow{f^i} \{C_k^{\epsilon_{i+1}}\} \rightarrow \cdots \rightarrow \{C_k^{\epsilon_P}\} \quad (4.7)$$

each associated with a sequence of chain groups $\{C_k^{\epsilon_i}\}$ (equation 4.7). Here the simplicial complex and associated chain groups capturing X at a finer scale are included in those of a grosser scale, captured by the inclusion maps f^i 's. Importantly, these inclusion maps help to associate the holes (or non-bounding cycles) in the complexes across scales. Each independent k -dimensional hole can then be represented as an interval (ϵ_b, ϵ_d) , where ϵ_b is the scale at which a hole emerges, i.e. its *birth scale*, and ϵ_d the scale at which it was filled in, i.e. its *death scale*. The life span $\epsilon_d - \epsilon_b$ indicates how persistent the hole is across scales (not to be confused with persistence over time, e.g. metastable dwells). With this interval representation, we can visualize these k^{th} homological features across scales as *barcodes* [169] (Figure 4.7D and E shows the persistence of generators of the 0^{th} and 1^{st} homology groups H_0 and H_1 respectively, capturing connected components and loops across scales). The set of all intervals constitutes a multiscale topological portrait of a coordination pattern X . Using the software Perseus developed by Nanda [170], we compute such topological portraits (0^{th} and 1^{st} persistent homology) for each pattern $X(t)$ (constructed as described in Section 4.2.1) for $t = 2, 3, \dots, 48$.

As mentioned at the beginning of this section, our end goal is to study the dynamics of such topological portraits in order to identify transitions in coordination patterns. This requires us to define a measure of distance between any two topological portraits. In the present study, we use *persistence landscape distance* as a metric, considering its low computation time and potential for statistical use [171]. Persistence landscapes [172] translate a set of intervals $\{(\epsilon_b^{(i)}, \epsilon_d^{(i)})\}_{i=1}^M$ into a sequence

of piecewise-linear *landscape functions* $\{\lambda^{(l)}\}_{l=1}^L$. Intervals are first used to construct a sequence of tent functions

$$f_i(\epsilon) = \begin{cases} 0 & \epsilon \notin (\epsilon_b, \epsilon_d) \\ \epsilon - \epsilon_b & \epsilon \in (\epsilon_b, \frac{\epsilon_b + \epsilon_d}{2}] \\ \epsilon_d - \epsilon & \epsilon \in [\frac{\epsilon_b + \epsilon_d}{2}, \epsilon_d) \end{cases} \quad (4.8)$$

for $i = 1, 2, \dots, M$. $\lambda^{(l)}(\epsilon)$ is the l^{th} largest value of $\{f_i(\epsilon)\}_{i=1}^M$. The smaller the l , the more prominent the features captured by the landscape function $\lambda^{(l)}$ (e.g. Figure 4.7 F, G shows first five landscape functions computed from intervals in D, E respectively; an interval with infinity that appears in every barcode is ignored in the computation, e.g. Figure 4.7D). $\lambda^{(L)}$ is the smallest function ($\lambda^{(L)}(\epsilon) \leq \lambda^{(l)}(\epsilon)$ for any l and ϵ) that is not zero for all ϵ . Now we can compare topological portraits of coordination patterns just like functions. We define the distance between the k^{th} topological portrait (persistent homology) of two coordination patterns X and X' as the sup norm of the difference between their corresponding average landscape functions,

$$D_k(X, X') = \|\bar{\lambda}_k(\epsilon) - \bar{\lambda}'_k(\epsilon)\|_\infty = \sup_{\epsilon} |\bar{\lambda}_k(\epsilon) - \bar{\lambda}'_k(\epsilon)| \quad (4.9)$$

where $\bar{\lambda}_k(\epsilon) = \frac{1}{K} \sum_{l=1}^L \lambda_k^{(l)}(\epsilon)$, and $\{\lambda_k^{(l)}\}_{l=1}^L$ and $\{\lambda'_k^{(l)}\}_{l=1}^L$ are the k^{th} persistence homology of X and X' represented as landscape functions.

With a metric defined, we are in a position to study the recurrence plot of topological portraits, which is a distance matrix with components $d_{i,j} = D_k(X(t_i), X(t_j))$ for the k^{th} persistent homology of a time series of coordination patterns $X(t)$ (Figure 4.8A-B, D-E). The subdiagonal of this matrix reflects the rate of change of topological features as a function of time. To provide additional comparison between topology-based and non-topological recurrence, we define a *state-based* metric by treating each

point cloud with M points as a state vector with $3M$ components,

$$\begin{aligned} d_x(X, X') = & \| (x_1 - x'_1, \dots, x_M - x'_M, \\ & W(x_{M+1} - x'_{M+1}), \dots, W(x_{2M} - x'_{2M}), \\ & x_{2M+1} - x'_{2M+1}, \dots, x_{3M} - x'_{3M}) \| \end{aligned} \quad (4.10)$$

for coordination patterns $X = \{x_i\}_{i=1}^M$ and $X' = \{x'_i\}_{i=1}^M$, where W follows the definition in equation (4.3). Recurrence plots based on this metric are included (Figure 4.8C, F) in addition to the traditional recurrence plots of relative phase (Figure 4.3) to show how much information is gained by the decomposition alone (Section 4.2.1), without any topological analyses. Notice that $d_x(X(t_i), X(t_j))$ increases with the time difference $|t_i - t_j|$, which does not reflect the difference in coordination pattern. Therefore we shift each point in $X(t)$ along the time-axis backwards by t , before computing the recurrence plot. This is not a problem for D_k , since topological portraits are invariant under translation of the pattern.

In the next section, we will show how the topological method outlined here reveals transitions in the coordination dynamics between eight agents (Figure 4.2) that eluded traditional methods of visualization and analysis (Figure 4.2A, Figure 4.3B).

4.3 RESULTS

Before investigating the eight-agent example, we first validate this method with the triadic example (Figure 4.1), the dynamics of which we already know (see Section 4.1). Figure 4.8AB shows the recurrence of topological features, i.e. connected components (0^{th} persistent homology) and loops (1^{st} persistent homology) respectively. In Figure 4.8A, three moments stand out against the background (marked by black triangles), indicating sudden changes in connected components. These moments coincide with three “escapes” from the all-inphase pattern in the original relative phase dynamics (steepened magenta trajectory ϕ_{13} following each of the three black triangles in Figure

4.1A; the same interruptions in the coordination pattern can be seen in Figure 4.3A). Figure 4.8B reveals a small transition around 10s and a large transition around 40s (marked by black triangles) in terms of loops. They coincide with the time of the first formation of the all-inphase pattern and its eventual destruction (replaced by inphase-antiphase pattern), which can be clearly seen in Figure 4.1A and Figure 4.3A. Taken together, topological recurrence (Figure 4.8AB) is able to faithfully capture important transitions of coordination patterns observed in the triadic example (Figure 4.1), as much as the traditional recurrence plot of the relative phase (Figure 4.3A). For comparison, a state-based recurrence plot is shown in Figure 4.8C (i.e. treating each point cloud as a state vector without extracting topological features, as defined by equation 4.10), which also captures the essential transitions but not as definitely as the topology-based recurrence plots (Figure 4.8AB) or the traditional recurrence plot of relative phases (Figure 4.3A). This indicates that the clarity present in the topology-based recurrence plots (Figure 4.8AB) is not solely due to the decomposition into slow and fast components, or more generally, the point cloud representation of coordination patterns (Section 4.2.1).

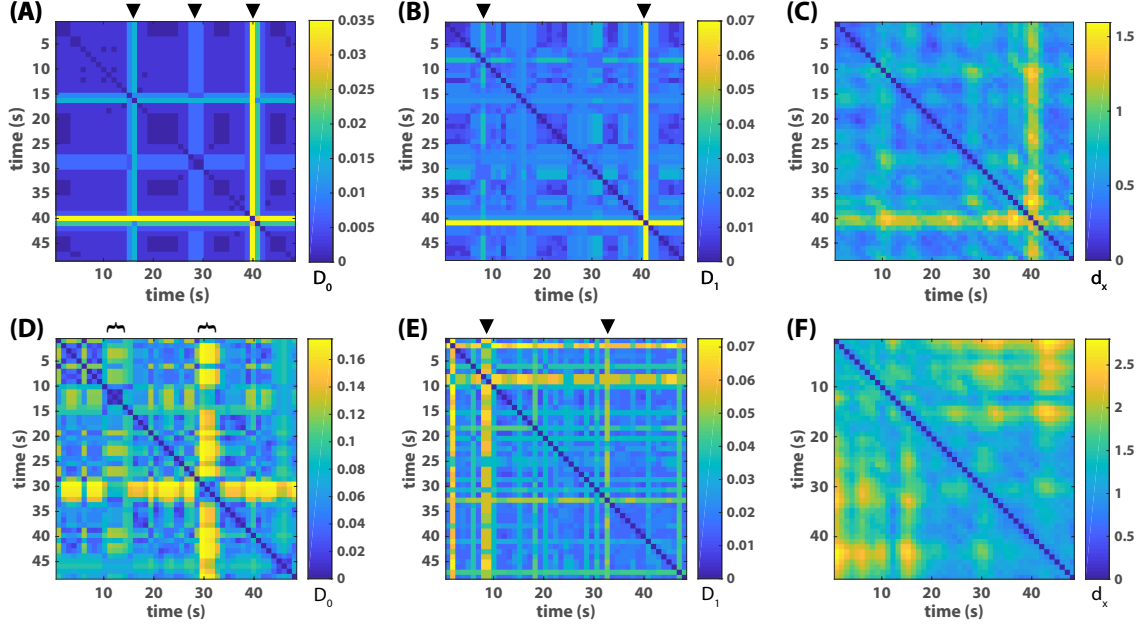


Figure 4.8: Recurrence plots of topological features versus states. (A-B) shows the recurrence of connected components and loops respectively for the triadic example, where the color of each pixel indicates the topological distance between the coordination pattern at time x and time y , as defined in equation (4.9), i.e. $D_0(X(x), X(y))$ for (A), $D_1(X(x), X(y))$ for (B). Black triangles on top mark the time of topological transitions. They correspond very well with transitions in the original relative phase dynamics (Figure 4.1A) and its associated recurrence plot (Figure 4.3A). (C) shows the recurrence of states, where the color of each pixel reflects the distance between point clouds $X(x)$ and $X(y)$ as state vectors, as defined in equation (4.10), instead of their topological portraits. The same transitions also appear in (C) as in (A-B) though less sharp. (D-E) shows the corresponding recurrence plots for the eight-agent example (Figure 4.2). In the recurrence plot of connected components (D), two transitions are apparent, each of which lasts about 5s (marked by black brackets). The onset of first transition (around 10s) and the offset of the second (about 33s) also stands out in the recurrence plot of loops (E), marked by black triangles. These features are not apparent in the state-based recurrence plot (F, also Figure 4.3B).

Following the basic validation above, we are ready for the eight-agent case. The recurrence of connected components (Figure 4.8D) is strikingly structured, compared to the original dynamics (Figure 4.2), the recurrence of relative phases (Figure 4.3B) and the state-based recurrence of point clouds (Figure 4.8F). It shows a major transition (in terms of connected components) around 30s and a minor one around 10s (marked by black brackets on top of Figure 4.8D). The onset of the 10s transition

and the offset of the 30s transition are also highlighted by the transition of loops (marked by triangles in Figure 4.8E). Next we return to the original relative phase and frequency dynamics (Figure 4.9) to investigate what underlies these topological transitions, with an emphasis on the transitions of connected components.

We begin with the major transition (of connected components) around 30s (second period with black background in Figure 4.9). Before the onset of this transition, the ensemble was in a relatively stable configuration with three frequency pairs (Figure 4.9A, trajectories enclosed by black circles), a lone wolf (agent 1, magenta trajectory on top in Figure 4.9A), and a commuter (agent 4, yellow trajectory in Figure 4.9A) oscillating between its neighbors (i.e. lone wolf agent 1, and pair 2-3). At the onset of the transition (28s), the top two frequency pairs broke up and an episode of partner-switching occurred at 30s (from configuration [1, 4, 3-2, 5-7, 6-8] to [1, 4-3, 2-5, 7-6-8]). After another partner-switching at the offset of the transition (33s), the original configuration was restored. This partner-switching dynamics is also reflected in the relative phases (slowly varying relative phases in Figure 4.9B correspond to circled-pairs in A, and fast varying relative phases in C correspond to relations indicated by double arrows in A). Among the slowly varying phase relations (Figure 4.9B), 3-2 (orange) departs from antiphase ($\pm\pi$) at the onset of the transition (break-up of the frequency pairs), wraps for one cycle during the transition (orange trajectory tilting), and returns to antiphase at the offset of the transition (green trajectory 5-7 has a similar action, but only wraps for half a cycle during the transition from near inphase to near antiphase). Complementarily, the fast varying phase relation 4-3 (yellow trajectory in Figure 4.9C) stops wrapping during the transition and dwells near antiphase (forming a transient new pair; similar action is observed in 2-5 and 7-6 in Figure 4.2A, though not repeated in Figure 4.9C to avoid visual crowding). In short, we see an interesting non-local transition of multiagent coordination patterns in both frequency and relative phase, detected by a major transition in the topological

portrait.

If we trace the global configuration right before the major transition (3 pairs + 1 lone wolf + 1 commuter, around 25s in Figure 4.9A) backwards in time, we reach the minor transition around 10s (first period with black background). In fact, the minor transition of connected components marks the inception of the said global configuration, where agent 1 (magenta in Figure 4.9A) departs from the warm-color group becoming a lone wolf (also seen in Figure 4.9C as suddenly increased slope of relative phase 1-4), as pairs 3-2, 5-7 stabilize (Figure 4.9B orange, green trajectories become flat; the three trajectories in B are in fact most stable during this period rather than afterwards). In contrast to the major one, this minor transition signifies multiple local events.

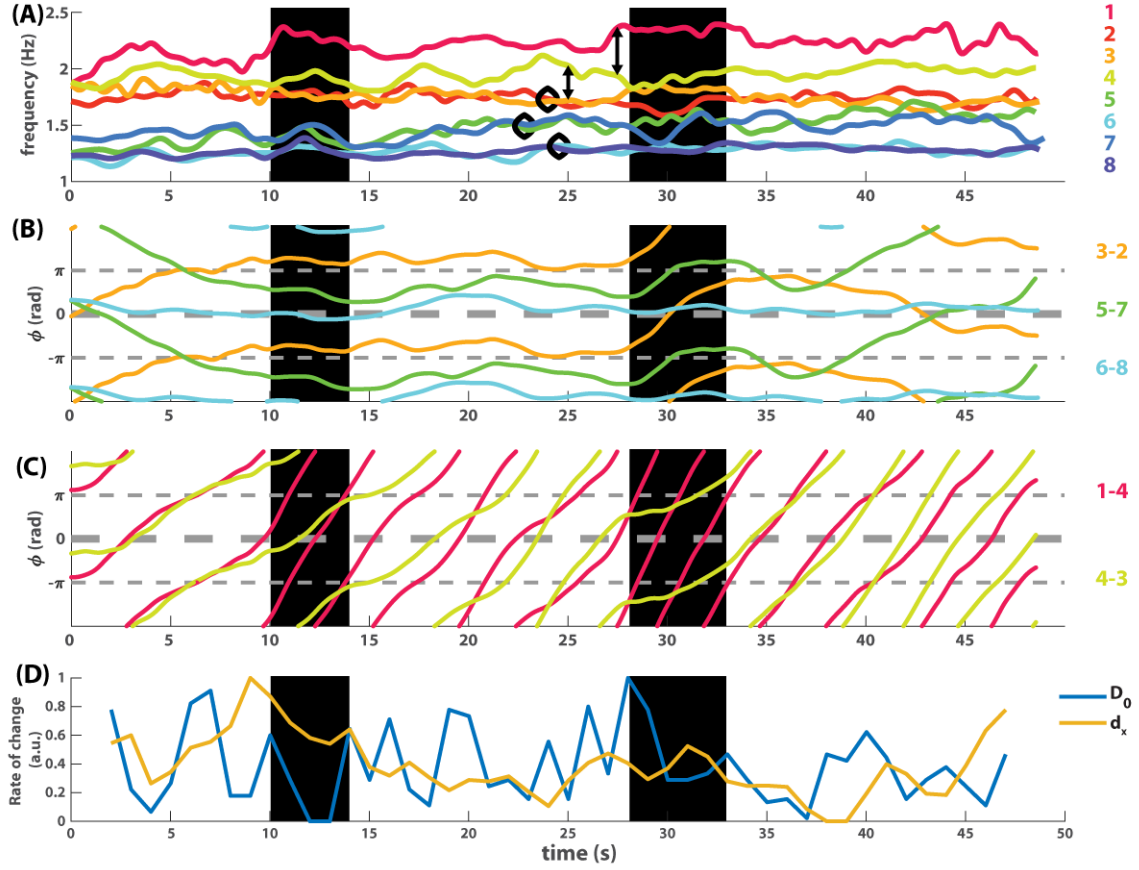


Figure 4.9: Breaking down the frequency, relative phase and topological dynamics of the eight-agent coordination. (A-C) shows selected trajectories of frequency and relative phase from Figure 4.2, after a 2s moving average. (A) shows the frequency dynamics of all eight agents. (B) shows the dynamics of three slowly varying relative phases (thickened trajectories in Figure 4.2A), corresponding to three pairs of frequency trajectories enclosed by black circles in (A). (C) shows the dynamics of two fast varying relative phases (among the thin trajectories in Figure 4.2A), corresponding to relations between frequency trajectories connected by double arrows in (A). (D) shows the rate of change of connected components (blue trajectory) and states (yellow trajectory), which is the distance between two consecutive patterns under the metric D_0 (equation 4.9) and d_x (equation 4.10) respectively. Both trajectories are normalized by mapping $[\min, \max] \mapsto [0, 1]$ for comparison. Two transitional periods seen in Figure 4.8D are highlighted with black backgrounds, bordered by adjacent peaks in the blue trajectory in (D). See text for interpretations.

The transitions of loops (marked by triangles in Figure 4.8E) provide supplementary descriptions of the two transitions discussed above. In particular, the transition of loops around 10s reflects local disturbances, i.e. high amplitude oscillation in agent 1 and 3's frequency (magenta and orange trajectories in Figure 4.2B and Figure 4.4B)

in anticipation of the departure of agent 1 (and the corresponding transition in connected components). The transition of loops near 32s is weaker and reflects small oscillations of agent 1, 7 and 8 (magenta, blue and purple trajectories near 32s in Figure 4.4B) anticipating the end of the major transition of connected components.

Overall, the recurrence plots of topological portraits not only reveal transitions of coordination patterns in the data that eluded traditional methods but also inform us about the relative significance of such transitions (i.e. global or local transition, high or low disturbances). To have a sense of why state-based recurrence is not sensitive to such information, we compare side by side the topology-based rate of change (blue trajectory in Figure 4.9D) and the state-based rate of change (yellow trajectory). By studying the onset of two transitions (the left edge of black rectangles in Figure 4.9D), we find that a sudden change in topology (blue peak, 28s) does not require a sudden change of state (i.e. position of individual points in the point cloud), and conversely, a sudden change of state (yellow peak, 9s) does not imply a sudden change in topology. In other words, the topological method captures the interdependency between the movement of individual points in the point cloud, which cannot be captured, in principle, by the “sum” of independently measured movements of each point.

4.4 DISCUSSION

In this chapter, we adopted a topological approach to analyzing metastable coordination dynamics involving many diverse agents, and demonstrated its efficacy in a proof-of-concept study of two example trials of human coordination from a recent experiment (Chapter 2, [35]). By studying the recurrence and dynamics of topological portraits, we revealed structures in the dynamics and important transitions of coordination patterns that eluded traditional methods (contrast Figure 4.9DE for the topological method with Figure 4.2 and Figure 4.3B for traditional methods). For example, a non-local topological transition (major transition around 30s in Figure

4.8D, 4.9) was discovered, showing how sudden, coordinated pattern switching can occur across multiple local groups that are segregated in frequency. This transition has been reported and discussed in [35] but the method of discovery was deferred till the present work for a full exposition.

The topological approach works well in the present case due to a few important features, and may prove advantageous in more general applications to coordination phenomena in complex systems. First, simplicial complexes are purely relational (coordinate-free) representations of structures, i.e. any rigid motions of the structure are “taken out” when converted into a simplicial complex. The subsequent topological analyses also retain relational-only information. In the study of coordination phenomena, relational quantities are of the essence [28], and can be gleaned from a dynamic pattern by mapping it to a simplicial complex. Second, topology is the mathematical discipline that helps connect pieces of local information into global information [173]. In multiagent coordination, the number of relational quantities multiplies ($N(N - 1)/2$) dyadic relations between N agents can be uniquely determined by $N - 1$ independent ones, as in Figure 4.2A). These relational quantities constrain each other and form higher-order structures [35, 40] which may not be discernible by examining each quantity individually. Algebraic topology and computational algebraic topology provide a mature set of tools to build global pictures from such local (e.g. dyadic) relational quantities. As demonstrated in our results, the ability of topological portraits to represent global information is a key to detecting coordinated collective transitions that are not a simple accumulation of independent changes (see Figure 4.9D and corresponding text, as explained at the end of Section 4.3). Last but not least, as discussed in Section 4.1 and previous chapters, multiple spatiotemporal scales coexist in metastable coordination between multiple diverse agents. Persistent homology [162, 165] provides a well-developed mathematical framework to represent multiscale topological features (scale-wise resolution only limited by initial data and

computational feasibility). Beyond the specific context of metastable rhythmic coordination, relational, local-global and multiscale information are of key interest in the study of complex systems in general (e.g. [92, 174–176]). Thus the topological approach outlined in the present work may serve as a prototype for more general analyses of complex systems.

Over the past decade, computational topology has gradually attracted biologists' attention as a set of new tools to shed light on geometrical or topological structures in complex, high-dimensional data that were difficult to quantify or visualize by traditional means. For example, various types of topological portraits (not limited to persistent homology) have been used to study the shape of viral evolutionary tracks [177], RNA folding pathways [178], collective encoding of global spatial organization by groups of neurons [179, 180] and the geometry of neural dynamics [181, 182] (see [183] for more applications in neuroscience). In contrast to these studies, where topological portraits are the primary subject of analyses and interpretation, here we focused on the *change* of topological portraits without direct interpretation of the portraits themselves. Instead, we returned to the original time series to recover what underlie such changes (transitions). There are technical and theoretical reasons to do so, which will be discussed next.

Technically, the exact content of a topological portrait may be affected by how the original data were sampled and subsequently how point clouds were constructed from the data (Section 4.2.1). In particular, its direct interpretation may vary with the metric associated with the point cloud (equation 4.2), which in the present study is subject to scaling (stretching a point cloud along different dimensions). Nevertheless, we preserve our ability to differentiate between patterns based on their topological portraits, so long as the data are sampled in the same way and the point clouds defined by the same metric, as in the present study. If we see a change in the topological portrait, there must be a corresponding change in the coordination pattern; and if the

change in the coordination pattern is sufficiently small, the change in the topological portrait is also small (due the fact that the topological portraits are stable with respect to the metric defined in equation 4.9 [172]). In other words, it is easier to detect changes in topological features than to describe those exact features from the portraits.

On the theoretical side, studying phase transitions is key to understanding nonlinear dynamical processes, and with respect to rhythmic coordination, we expect to see some form of topological (homological) change in the original frequency and relative phase dynamics if an actual transition has occurred. Here a phase transition refers to a change of (literally) phase relation in one or more pairs of oscillatory processes, e.g. a pair switching from dwelling at a relative phase to phase wrapping, to stay apart or to form new phase relations. At such a transition, previously overlapping frequency trajectories may bifurcate (at the end of a dwell), whereas the resulting branches either stand alone, merge with other trajectories or merge back together. Topologically (in a sufficiently large neighborhood near the transition), these three scenarios lead to a lasting increase in the number of connected components (e.g. first transition 10s in Figure 4.9A), a transient reduction in the number of connected components (by merging into a larger one; e.g. time block 27-29s in Figure 4.9A), or a transient loop formation (e.g. time block 39-41s in Figure 4.1B) respectively. The latter two are particularly interesting because the magnitude of the topological change is not so much about the topological difference between the pattern before and after the transition, but that the topology during the transition is highly nongeneric compared to what happens before and after. As reflected in our results, these features indeed stand out against the backgrounds (e.g. 30s in Figure 4.8D, and 40s Figure 4.8B). In short, the current interpretation directly addresses dynamics-relevant topological changes in the original time series, without interpreting the topological portraits as an intermediate step.

This does not mean however that we are uninterested in direct analyses and interpretation of topological portraits. To the contrary, the motivation behind using persistent landscapes is that they are conducive to further statistical analyses. But first we need to know which statistics are relevant to the underlying dynamics. For example, does the magnitude of change in connected components (average 0th persistent landscape) truly reflect the scope of a phase transition (how local-global the transition is, e.g. comparing the minor and major transitions in Figure 4.9)? If we divide the analysis of topological recurrence by scale, will we be able to infer at what scale a transition occurs? Or more generally, can we accurately classify the type of phase transitions (see examples in the previous paragraph) by taking into account all landscape functions (without averaging)? Answers to these questions are highly desirable. To deliver valid answers, systematic testing is required on transitions whose classification we know *a priori*, e.g. simulated transitions based on mathematical models (see [40] for a model developed based on the Human Firefly experiment [35]). There have been successful applications of computational topology in capturing known periodic behavior and topological phase transitions in theoretical models of physical systems [184, 185]. As for models of biological systems, in particular regarding multiagent metastable patterns (see Chapter 3), a systematic classification and parametrization of all possible transitions is non-trivial in itself and still in its early development. We therefore leave a model-based analyses to future research.

To conclude, we proposed in this chapter a topology-based approach to understanding metastable coordination dynamics involving multiple agents. We demonstrated by analysis of examples and theoretical discussions that such a method can reveal structures in the dynamics in terms of transitions of various types. Further developments using simulated time series are required to head toward a systematic method of classifying phase transitions in multiagent coordination dynamics,

for which this chapter provides a prototype.

CHAPTER 5

TOWARD AN UNDERSTANDING OF MULTISCALE COORDINATIVE STRUCTURES

This dissertation includes a series of studies dedicated to the general question of how multiscale coordinative structures in nature (Section 1.1) are formed and under which laws of coordination. This question includes an empirical- and a theoretical-oriented aspect: what kind of coupled dynamical systems reflect the dynamic laws underlying multiscale coordinative structures in nature and what are the sufficient conditions for a coupled dynamical system to actually produce a multiscale coordinative structure. Separate treatments of these two aspects create dilemmas if such a law of coordination is nonlinear (a trait of complex systems, e.g. [186–188]). It is generally difficult to study the behavior of any high-dimensional nonlinear dynamical system globally and systematically. This means that even if a system of equations describing a “true law of multiscale coordinative structure” is right in front of you, you may never recognize it if a sufficient amount of time has not been invested in the theoretical study of its behavior. The flip side is that you may invest an indefinite amount of time on a system of nonlinear equations that in principle cannot produce any multiscale coordinative structure. By embracing both aspects, this dissertation contributes to the cyclic scientific process of empirical-theoretical investigation that aims toward a true understanding of multiscale coordinative structures.

Preexisting empirical and theoretical studies of rhythmic coordination often focus on the type of behavior (as measured) that lacks either, if not both, of two important aspects of multiscale coordinative structure: order with complexity and multiple levels of description (see Chapter 1). To reveal both aspects in the same empirical

setting, a new experimental paradigm was developed for probing coordination dynamics in intermediate-sized ensembles of humans. The size of the ensemble allows the coexistence of multiple levels of description. The accompanying experimental apparatus permits versatile control of the boundary conditions of human interaction such that regimes of complex coordination can be explored. Subsequently in the human experiment based on this paradigm (Chapter 2, [35]), manipulation of the boundary conditions (frequency diversity) affected coordination on multiple levels of description, including relations between and within frequency groups, as well as dyads.

Based on this experiment, a scalable, coupled phase oscillator model (equation 3.1) was developed to capture key experimental observations on all observed levels of description (Chapter 3). This new model unified two existing models of coordination – the Kuramoto model for large-scale coordination (Section 1.2) and the extended HKB model for dyadic coordination (Section 1.3) – essentially by adding second order coupling from the extended HKB to the Kuramoto model, or conversely adding scalability from the Kuramoto to the extended HKB model. We found that the second order coupling is indispensable for capturing experimental observations from Chapter 2, in particular, the coexistence of inphase and antiphase preference in dyadic relations. Further mathematical analyses showed that this coexistence of inphase and antiphase at the dyadic level reflected multistability endowed by second order coupling. For the coordination of identical oscillators to be multistable, the ratio between the second and first order coupling must exceed a critical value (Section 3.2.4). Beyond this critical value, any combination of inphase and antiphase relations is a stable coordination pattern; below this critical value, only all-inphase coordination (synchronization) is stable, the regime where the Kuramoto model lives. For this reason, the Kuramoto model cannot capture all key experimental observations. The critical value demarcating the regimes of mono- to multi-stable coordination is scale invariant. It is therefore identical to that of the HKB, which was also devised to

capture the mono- to multi-stable (bi-stable) transition in human rhythmic coordination [27]. This is not just a formal connection between models, but more importantly a connection between coordinative phenomena across scales obtainable through the models. Practically, experimenters may estimate the parameters (natural frequency and coupling strength as in, e.g., equation 3.5) that captures individual subjects' coordinative behavior at a small scale and predict what occurs at a larger scale between many such individuals. If the prediction is not aligned with observations, the difference between them would provide important information regarding what has changed with scaling. More generally, it connects the behavioral complexity observed in smaller systems to larger systems composed of them.

Similar to past studies of dyadic coordination ($N=2$, Section 1.3), the empirical data for multiagent coordination suggest two dynamical mechanisms for complex coordinative behavior: multistability (as summarized above) and metastability (coordination without phase-locking). Further theoretical study of the model (equation 3.3) in relevant parameter regimes reveals that a small addition of complexity at the dyadic level becomes much more powerful at larger scales. For multistability, the number of stable coordination patterns for coupled identical oscillators increases exponentially with scale. From the perspective of pattern formation, this means that the system's behavioral repertoire enlarges rapidly with size. On the other hand, multistability is also associated with memory (or "mneme" [189]) in biological, especially, neural systems [190–196]. Thus one may also say that the system's memory capacity grows exponentially with its size. This is analogous to static random-access memory in computers, where large memory capacity can be built from small bistable circuits (flip-flops). This is not a feature of the Kuramoto model, which only has one stable state (under a given coupling strength) regardless of scale. Hence, the Kuramoto model is memoryless, analogous to an imaginary computer whose memory is stored only in ones but no zeros. The analogy with computer memory, however,

reveals a problem. Namely, this type of complexity is decomposable, i.e. a subsystem has the same repertoire of coordination patterns regardless of whether it is isolated from the rest of the system or not (though the size of the basin of attraction may vary). Thus, a small-scale system does not gain emergent behavior by partaking in a larger system, which is in conflict with our expectation from a multiscale coordinative structure (Section 1.1). For a multiscale coordinative structure, at least with respect to the number of stable states, the whole seems to be neither the sum nor the product of its parts. The whole has to be different [140]. Multistability of the coordination of identical components is not a sufficient mechanism for complexity in multiscale coordinative structures.

When the components are diverse and the coupling sufficiently weak (Section B.1), metastability is at work. Unlike dyadic metastable coordination whose topology is unique, multiple purely metastable patterns (no phase-locking between any components) can be created by simply adding a third agent (Section 3.2.6). In fact, we conjecture that there are infinitely many purely metastable and topologically distinct patterns formed by three oscillators. This complexity of the three is not decomposable. Due to the lack of phase-locking in purely metastable coordination, it is associated with the incoherence regime of coupled phase oscillators, with finite- N fluctuations (i.e. temporal oscillation of the Kuramoto order parameter for a finite number of oscillators, see [12, 72, 197]). The fluctuations reflect intermittent dwells at and escapes from preferable phase relations (the analysis of multistability provides the number of dwells per revolution of the relative phase). Contrary to the common assumption that this is a regime of disorder, numeric results demonstrate (Chapter 3) that ordered and complex sequences of spatial patterns can be produced under metastable coordination (e.g. Figure 3.7, 3.8 and B.10; see also [33]). Metastability therefore is a mechanism for ordered-yet-complex behaviors that are not decomposable – a good candidate mechanism for generating multiscale coordinative structures.

Here “complexity” of a metastable pattern can be thought of as its *topological complexity* (e.g. [173, 198]) relative to purely phase-locked patterns (e.g. synchronization), measured by a vector of winding numbers of its relative phase orbit. Numeric results (Section 3.2.6 and B.9) further suggest that if a complex metastable pattern is a concatenation of some simpler patterns in time, the topological complexity of the complex pattern is the sum of the topological complexity of those simpler patterns. Moreover, one can predictably find this complex pattern by varying a single parameter (e.g. natural frequency of one oscillator, Section 3.2.6) between the values that lead to the simpler patterns that constitute it. In future research, an analytical proof of these results should be attempted. If successful, it would provide a mathematical framework for systematic studies of multiagent metastability by investigating the mapping from an oscillator system’s parameter space (natural frequencies and coupling strength) to algebraic structures (e.g. vector spaces).

In the study of metastable patterns, geometric features (e.g. clustering of curves, area of holes between curves) of frequency graphs (e.g. Figure 3.8) not only accurately reflect the topology of corresponding relative phase orbits (i.e. topological complexity of the metastable patterns) but also provide additional characterization of the patterns (e.g. the period, the sequence of concatenation from simpler patterns; see Figure B.10). As a result, high-dimensional coordination patterns can be studied geometrically as 2-dimensional graphs. A new method for analyzing such graphs was introduced, combining tools from traditional nonlinear time series analysis and computational algebraic topology, in particular, persistent homology. Persistent homology captures connected components and holes in these graphs at multiple scales as algebraic structures. By studying the dynamics of such algebraic structures, the method successfully captured important coordinated transitions in dynamic patterns formed by many diverse agents, which eluded traditional, non-topological methods. In future research, the method may be further improved and validated by honing

against simulated data, thereby creating a reliable computational tool for analyzing metastable patterns of multiagent coordination in simulated and empirical data.

One issue that has been touched upon but not fully explored in this dissertation is the long time scale behavior observed in the human experiment [35], which may be worth further empirical and theoretical investigation. In single-trial dynamics, there was indication of frequency adaptation (see Section B.8), which has been observed in human social coordination in dyads [154]. Statistically, the average level of dyadic coordination drifts towards a moderate level over time (Section A.5). It may be worth asking whether certain forms of adaptation in natural frequency or coupling strength lead the system toward regimes of certain types of metastable coordination (e.g. a certain level of topological complexity) and whether there is any benefit in doing so (e.g. having many other patterns to switch to via small parameter changes). These questions can be better addressed if the mathematical framework for multiagent metastability initiated in this dissertation is fully developed in future studies.

From multiagent metastability to multiscale coordinative structures, the study of adaptation or evolution of parameters (e.g. natural frequency and coupling strength) may be an inevitable path. The formation of units or modules in complex systems has well demonstrated evolutionary advantages [199–204]. The formation of such modules at multiple levels of description suggests a separation of evolutionary time scales (see [205]). To approach this problem from the perspective of coordination dynamics, one first needs to associate modularity of the parameters (e.g. clustering in frequency, modularity in network connectivity) with that of the dynamics. While there is a long way ahead towards a true understanding of multiscale coordinative structures, we must not lose our wonder about their “secrets” (Section 1.1).

I believe that the justification of art is the internal combustion it ignites in the hearts of men and not its shallow, externalized, public manifestations. The purpose of art is not the release of a momentary ejection of adrenalin but is, rather, the gradual, lifelong construction of a state of wonder and serenity.
– Glenn Gould [206]

APPENDICES

APPENDIX A

SUPPLEMENTARY INFORMATION FOR THE HUMAN EXPERIMENT

A.1 PREPROCESSING OF RECORDED SIGNALS

In the current study, we characterize social coordination in terms of frequency and phase relations. Here we detail how frequency and phase related variables were transformed from raw signals (square waves consisting of zeros and ones, see Experimental Setup). We define the inter-tap interval (ITI) as the time difference between the onsets of two consecutive taps. Instantaneous Frequency (F) is the reciprocal of ITI, interpolated linearly between taps in accord with the original sampling rate (250Hz). We obtained Phase (θ_i) by first assigning the value $2\pi(n - 1)$ to the onset of the n^{th} tap of the i^{th} individual, and then interpolating samples in between with a cubic spline method. Further, we define relational variables Frequency Ratio (FR_{ij}) and Relative Phase (ϕ_{ij}) between individual i and j as

$$FR_{ij} = \frac{\min(F_i, F_j)}{\max(F_i, F_j)} \quad (\text{A.1})$$

and

$$\phi_{ij} = \theta_i - \theta_j \quad (\text{A.2})$$

respectively. To quantify the degree of phase coordination, we segment each time series into consecutive 3s windows, and calculate the Phase-Locking Value (PLV) within such windows.

$$PLV = 1 - CV = \frac{1}{N} \left| \sum_{n=1}^N e^{i\phi[n]} \right| \quad (\text{A.3})$$

where CV is circular variance, and N is the total number of samples in a window (750 pts). PLV ranges from zero to one. A value of one indicates the maximal degree of coordination, and a value of zero indicates no coordination.

A.2 MULTIVARIATE ANALYSIS OF VARIANCE (MANOVA)

To study how dyadic coordination within and between initial groups (denoted as variable relation with two categories: within-group and between-group) changes as diversity varies (i.e. between-group difference in frequency predispositions, $\delta f = 0, 0.3, 0.6$ Hz), we performed a 2×3 (*relation* \times δf) MANOVA to compare the mean PLV in different conditions, using Type III Sums of Squares. Multiple comparisons were performed using Tukey HSD (honest significant difference) tests.

A.3 LINEAR REGRESSIONS AND CRITICAL FREQUENCY IDENTIFICATION

To study the macro organization of groups, we examined the relation between within-group and between-group phase coordination, and how it changes as diversity (δf) increases. Least Square method was used to obtain the regression line for each δf ,

$$PLV_{between-group}^{\delta f} = \beta_0^{\delta f} + \beta_1^{\delta f} PLV_{within-group}^{\delta f} + \epsilon^{\delta f} \quad (\text{A.4})$$

The slope $\beta_1 = \beta_1^{\delta f}$ is the relation between within- and between-group coordination, an index of the degree of integration between two initial groups. If $\beta_1 = 1$, there is only one undifferentiated supergroup. $0 < \beta_1 < 1$ indicates that initial groups integrated into a supergroup but there is remnant of the diversity (coordination with one group increases the coordination with the other group but not as much as when there is no diversity). $\beta_1 < 0$ indicates that initial groups remain segregated (coordination with one group decreases coordination with another group).

If there exists a diversity δf such that within-group coordination does not vary with between-group coordination (degree of integration $\beta_1^{\delta f=0}$), we call it a critical diversity (δf^*) – a separatrix between regimes of integration and segregation of two initial groups. To obtain δf^* , we regressed the degree of integration β_1 against diver-

sity δf ,

$$\beta_1 = \alpha_0 + \alpha_1 \delta f + \epsilon \quad (\text{A.5})$$

and estimated where the regression line crosses $\beta_1 = 0$,

$$\delta f^* := -\frac{\alpha_0}{\alpha_1} \quad (\text{A.6})$$

A.4 DISTRIBUTIONAL COMPARISON

To verify how much the distribution of relational variables (FR, ϕ) in each condition reflects genuine coordination, we constructed chance level distributions by random permutations of all taps within each condition (i.e. taps produced following the same metronome). A total of 10,000 random permutations were performed. For each permutation, relational variables were computed following the same procedures as that of the original data (see Section A.1) and a probability density function (PDF) was computed for each variable using a 100-bin histogram. Given a significance level of $p = 0.0005$ for each bin (based on Bonferroni correction for $\hat{p} = 0.05$ for the entire distribution), we computed the confidence interval around chance level distribution (two-tailed) as between $(100 - 50p)$ percentile and $50p$ percentile of the 10,000 random distributions for each bin. The real distribution is significantly different from chance at a specific value of FR or ϕ , if the probability density of this value is outside the confidence interval (seen as light-colored bands in main text Figs).

A.5 LONG TIME-SCALE BEHAVIOR IN HUMAN COORDINATION

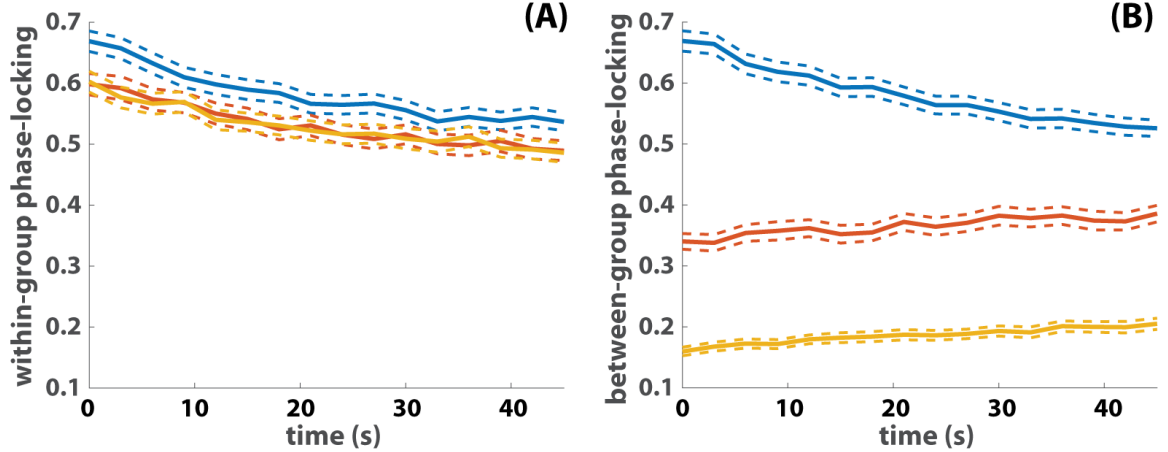


Figure A.1: Multiagent coordination exhibits slow dynamics. In the experimental data, between agents of low initial frequency difference (i.e. within-group, A; between-group for $\delta f = 0$ Hz, B blue), initially high phase locking tended to decrease over time. In contrast, under moderate to high initial frequency difference (B, red, yellow), initially weak coordination slowly strengthened. Solid and dashed lines are, respectively, means and standard errors of phase-locking value over all trials of a specific diversity condition (δf) in fixed time windows.

Considering the evolution of phase-locking during interaction, we found that a high degree of phase-locking was unsustainable, which can be seen in Figure A.1 as the decaying phase-locking value overtime for those whose initial phase-locking value is above 0.5 (i.e. within-group coordination in all three intergroup difference conditions, see A, and between-group coordination when there is no intergroup difference, see B, blue curve). In contrast, low levels of phase-locking (below 0.5, stemming from large initial frequency difference) tend to increase over time (Figure A.1B, red, yellow curves). The finding suggests that when dyadic interactions are embedded in a larger ensemble, they tend to persist as moderate phase coordination rather than the very strong or very weak ones.

APPENDIX B

SUPPLEMENTARY INFORMATION FOR THE MODEL

B.1 CHOOSING THE APPROPRIATE COUPLING STRENGTH

What we want to see is how the present model behaves as we manipulate the diversity of natural frequency ω_i 's just as we did to human subjects. However, there remain two unknown parameters to be taken care of, namely the coupling strength a and b in equation (3.3). Before systematically finding the appropriate coupling strength, we want to first show qualitatively how it affects the dynamics.

Three simulated trials with increasing coupling strength are shown in Figure B.1 from A to C, whereas the initial phases and natural frequencies are the same across trials (warm-color group centered around $f_A = 1.2$ Hz, cold-color group $f_B = 1.8$ Hz, corresponding to $\delta f = 0.6$ Hz). When the coupling is weak ($a = b = 0.1$, Figure B.1A), oscillators are well-segregated into two frequency groups. Within each frequency group, members intermittently converge (marked by black triangles) then diverge, reflecting metastability at a group level (collective dwells). For intermediate coupling ($a = b = 0.2$, Figure B.1B), oscillators within each group are locked together, interacting strongly as a whole with the other frequency group (seen as the oscillation of frequency), so that the ensemble ($N = 8$) behaves like a dyad ($N = 2$). Finally, for strong coupling ($a = b = 0.4$, Figure B.1C), everyone converges to a single steady frequency. We see a progression from group-level segregation to integration from (A) to (C), indicating the important role of coupling strength in determining intergroup relation. Qualitatively, the model's behavior under weak coupling (Figure B.1A) is closer to human behavior (Figure 3.2C) than that of stronger coupling. Next we take a more quantitative look.

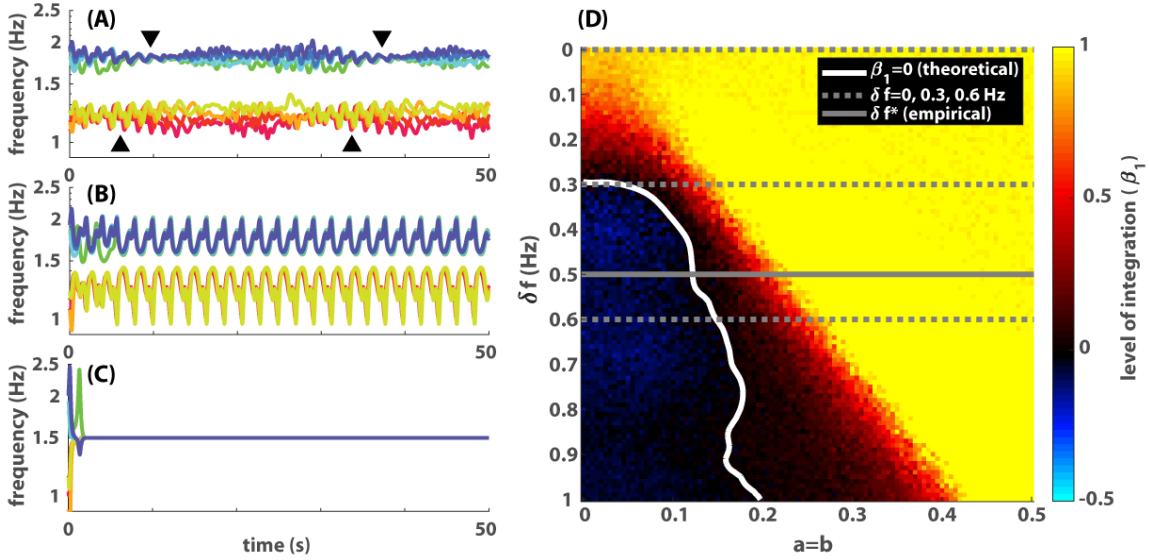


Figure B.1: The effect of diversity and coupling strength on the level of integration between groups. (A-C) show frequency dynamics of three simulated trials, with increasing coupling strength ($a = b = 0.1, 0.2, 0.4$ respectively) and all other parameters identical (the warm-color group's natural frequencies evenly spread in the interval $[f_A - 0.08\text{Hz}, f_A + 0.08\text{Hz}]$ with $f_A = 1.2\text{ Hz}$), similarly for the cold-color group in $[f_B - 0.08\text{Hz}, f_B + 0.08\text{Hz}]$ with $f_B = 1.8\text{ Hz}$; initial phases are random across oscillators but the same across trials). When the coupling is too strong (C), all oscillators lock to the same steady frequency. When the coupling is moderate (B), oscillators split into two frequency groups, phase-locked within themselves, interacting metastably with each other (dwell when trajectories are close, escape when trajectories are far apart). When the coupling is weak (A), intragroup coordination also becomes metastable seen as episodes of convergence (black triangles) and divergence. (D) shows the level of intergroup integration quantitatively (β_1 , color of each pixel) for each combination of frequency diversity δf and coupling strength $a = b$. White curve indicates the critical boundary between segregation (blue area on the left, $\beta_1 < 0$) and integration (red and yellow area on the right, $\beta_1 > 0$). Within the regime of integration, the yellow area indicates complete integration ($\beta_1 \approx 1$) where there is a high level of phase locking, and the red area indicates partial integration ($0 < \beta_1 \ll 1$) suggesting metastability. Dashed gray lines label δf 's that appeared in the human experiment. Solid gray line labels the empirically estimated critical diversity.

To quantify the joint effect of frequency diversity (δf) and coupling strength ($a = b$ for simplicity) on integration and segregation between two frequency groups, we calculated the level of intergroup integration (β_1) for simulated trials using the same method as for the human experiment (see Phase-locking value and level of integration in Materials and Methods in the main text). For each parameter pair

$(\delta f, a)$ with $a = b$, we simulated 200 trials. In each simulated trial, two frequency groups A and B each consists of four oscillators ($\varphi_1, \dots, \varphi_4$ in group A , $\varphi_5, \dots, \varphi_8$ in group B). The natural frequency of oscillators in group A (i.e. $\omega_1, \dots, \omega_4$, divided by 2π) was drawn from a distribution $P(f_A)$ centered around f_A (corresponds to the metronome frequency for the group in the human experiment), and $P(f_B)$ for group B . The difference between two groups $\delta f = |f_A - f_B|$ corresponds to the level of diversity in the human experiment. Here the probability density function $P(f)$, which defines frequency dispersion within each group, was obtained by a nonparametric estimation of the empirical distribution (see Materials and Methods in the main text).

The level of integration for simulated trials is shown in Figure B.1D as the color of each pixel (diversity δf as y-coordinate; coupling strength $a = b$ as x-coordinate). Three regimes are apparent: the highly integrated (yellow, $\beta_1 \approx 1$), the partially integrated (red, $0 < \beta_1 \ll 1$), and the segregated (blue, $\beta_1 < 0$). Between the red and blue area is the critical boundary (white solid line, $\beta_1 = 0$), separating the regimes of integration and segregation. With any fixed coupling strength, for the critical boundary to fall between $\delta f = 0.3$ Hz and $\delta f = 0.6$ Hz as in the human experiment, the coupling strength has to be weak (for $\delta f = 0.6$ Hz, $\beta_1 < 0$ only when $a = b < 0.15$) but not too weak (for $\delta f = 0.3$ Hz, $\beta_1 > 0$ only when $a = b > 0.05$). Without risking overfitting, we simply choose the coupling strength $a = b = 0.105$, for which the level of integration is the closest to experimental observation for $\delta f = 0.3$ Hz ($\beta_1 = 0.31$).

B.2 EMPIRICAL DISTRIBUTION OF TAPPING FREQUENCY AROUND METRONOME FREQUENCY

In the “Human Firefly” experiment [35], subjects’ tapping frequency during the transient between pacing and interaction (a proxy to “natural frequency”; see Materials and Methods in main text) dispersed around the metronome frequencies. The distribution of this deviation from metronome frequencies is shown in Figure B.2 (blue

histogram). Most of the time, subjects were very close to the metronome frequency (peak around zero). We can use a normal distribution $\mathbb{N}(\mu, \sigma)$ to capture this peak (Figure B.2 yellow line) where parameters $\mu = 0$ and $\sigma = 0.0986$ (Hz) were estimated using the median and 10th percentile of the empirical distribution. We can see a difference between the empirical distribution and the normal distribution - the normal distribution (yellow line) does not capture the fat-tails of the empirical distribution (blue bars exceed yellow line on its shoulders). These “mutant fireflies” making up the fat-tails are not to be dismissed as outliers, because they contribute to the behavior of others in the ensemble. To better represent the empirical distribution, we used Kernel Density Estimation (with a normal kernel) as described in section Estimating the distribution of natural frequencies of Materials and Methods in the main text, and the result of estimation is shown as the red line in Figure B.2 (named kernel distribution). The kernel distribution better captures the tails of the empirical distribution and was used to generate natural frequencies of oscillators in the simulations.

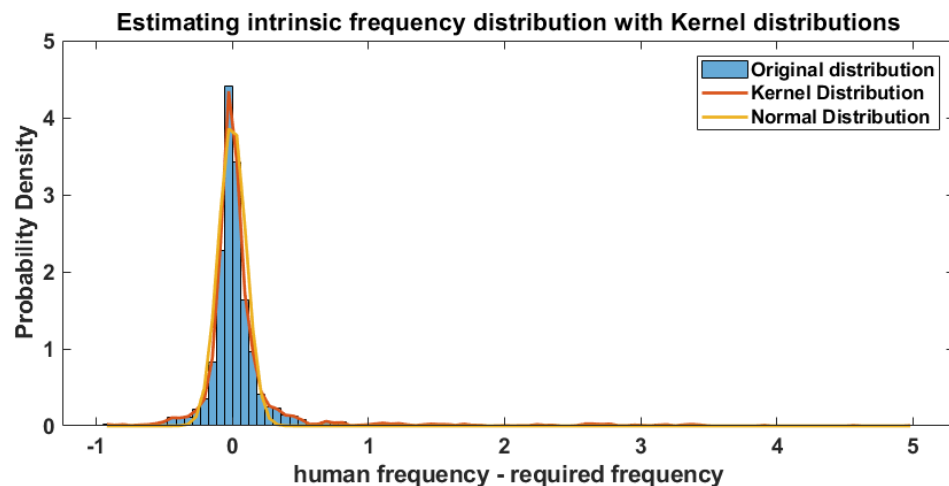


Figure B.2: Distribution of human movement frequency around metronome frequencies and its estimation.

B.3 EXAMPLES OF DYNAMICS WITH INTERGROUP COUPLING REMOVED

By removing intergroup coupling, we obtain a modification of equation (3.3)

$$\dot{\phi}_i = \omega_i - a \sum_{j=1}^N e_{ij} \sin \phi_{ij} - b \sum_{j=1}^N e_{ij} \sin 2\phi_{ij} \quad (\text{B.1})$$

where $e_{ij} = 1$ if $i, j \in \{1, 2, 3, 4\}$ or $i, j \in \{5, 6, 7, 8\}$, $e_{ij} = 0$ otherwise, for $N = 8$.

The resulting dynamics (with all other parameters the same as examples in Figure 3.4A-C in the main text) are given in Figure B.3. Within each frequency group (one group in cold colors, one group in warm colors), we see the same metastable dynamics being repeated regardless of intergroup difference ($df = 0, 0.3, 0.6$ Hz for Figure B.3A, B, C respectively). These trials, without intergroup coupling, provide a baseline dynamics for comparison with Figure 3.4A-C, revealing the effect of intergroup influence. It turns out that for a given intragroup coupling, intragroup metastability comes from intragroup dispersion of natural frequencies. Metastability vanishes when two metastable groups have no intergroup difference (Figure 3.4A). In other words, without intergroup difference ($\delta f = 0$), there are more oscillators within the same range of frequency, which cooperatively increases intragroup coordination. If we remove this intragroup dispersion of natural frequency (along with the metastability), we can no longer reproduce the experimental observation that intragroup coordination was weakened and altered by intergroup differences (see Section B.4 for a statistical analysis).

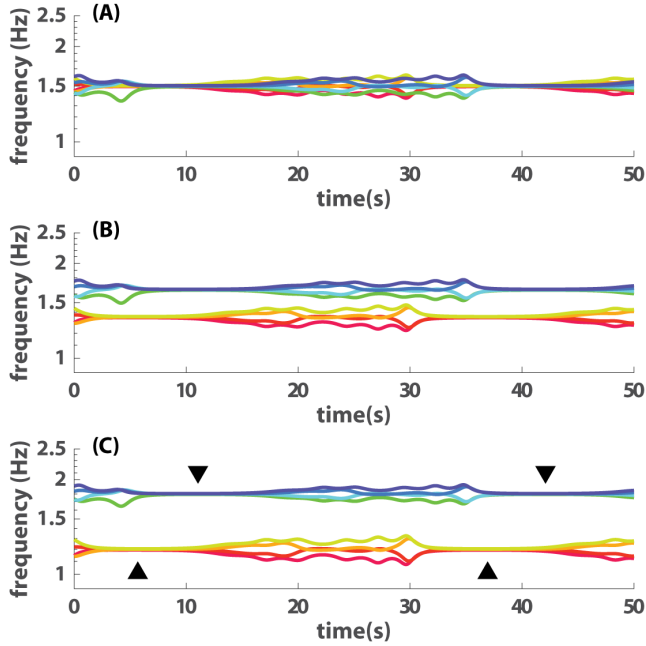


Figure B.3: Intragroup dynamics without intergroup coupling, for intergroup difference $\delta f = 0$ (A), $\delta f = 0.3$ (B), and $\delta f = 0.6$ Hz (C).

With intergroup coupling, the time scale of metastability is modified by δf , as shown in Figure 3.4BC where the interval between two episodes of convergence (black triangles) is shorter for $\delta f = 0.3$ Hz (B) than for $\delta f = 0.6$ Hz (C). In Figure B.4A, this is also visualized as the dynamics of phase-locking value (PLV) within groups (average PLV of all intragroup dyads in 3-s windows). When oscillators within groups converge, PLV is close to 1, and the interval between two consecutive peaks in a PLV trajectory reflects the time scale of the metastable coordination. Without influence from the other group, the time scales are exactly the same (trajectories exactly on top of each other in Figure B.4B). With influence from the other group, the time scale depends on the level of intergroup difference (inter-peak intervals for $\delta f = 0.3$ Hz was much shorter than that of $\delta f = 0.6$ Hz in Figure B.4A). Perhaps, we can consider $\delta f = 0$ Hz (i.e. lost of metastability, B.4A blue line) as the special case where the inter-convergence interval is zero.

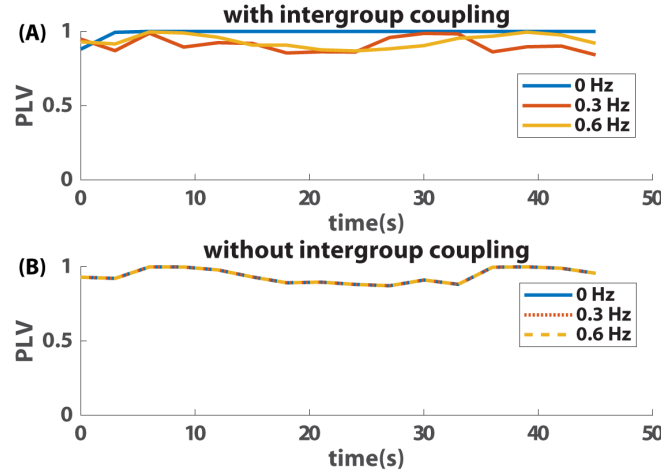


Figure B.4: Dynamics of intragroup phase-locking value (PLV) with (A) and without (B) intergroup coupling for different levels of frequency diversity δf (color coded, see legends).

It is also interesting to notice that for $\delta f = 0.6$ Hz, the metastable time-scale of the trial with intergroup coupling (Figure B.4A yellow line) is very similar to that of the trial without intergroup coupling (Figure B.4B yellow line). This may be connected to the fact that $\delta f = 0.6$ Hz (given $a = b = 0.105$) is in the regime of intergroup segregation. It is perhaps a hypothesis worth further investigation that the level of intergroup integration (as measured by β_1 , see main text) reflects how the time scale of intragroup metastability was affected by intergroup difference. Here our discussion of these examples is only to provide an intuitive understanding of the dynamics.

B.4 EFFECT OF REDUCED INTRAGROUP VARIABILITY IN NATURAL FREQUENCY

Recall that the reduction in intragroup coordination shown in Figure 3.3D (left) was based on simulations with nontrivial dispersion in natural frequency within each group, reflecting the natural variability carried into the experiment by human subjects. What if we remove that intragroup dispersion? As shown in Figure B.5A (left three bars), intragroup coordination becomes very close to the maximal level (phase-locking value close to 1) for all diversity conditions (MANOVA interaction

effect $F(2, 19194) = 50152, p < 0.001$); we no longer see the large drop in intragroup coordination as seen in Figure 3.3BD. Even if we break the symmetry in coupling strength (use equation (3.1) with random coefficients, instead of uniform coupling in equation (3.3); see Random coupling for details), the phenomenon is not recovered (Figure B.5B very similar to A; MANOVA interaction effect $F(2, 19194) = 59678, p < 0.001$). By studying the model's behavior, we found that the reduction in intra-group coordination due to intergroup difference, as observed in the human experiment, mainly depends on asymmetry in natural frequency rather than coupling strength.

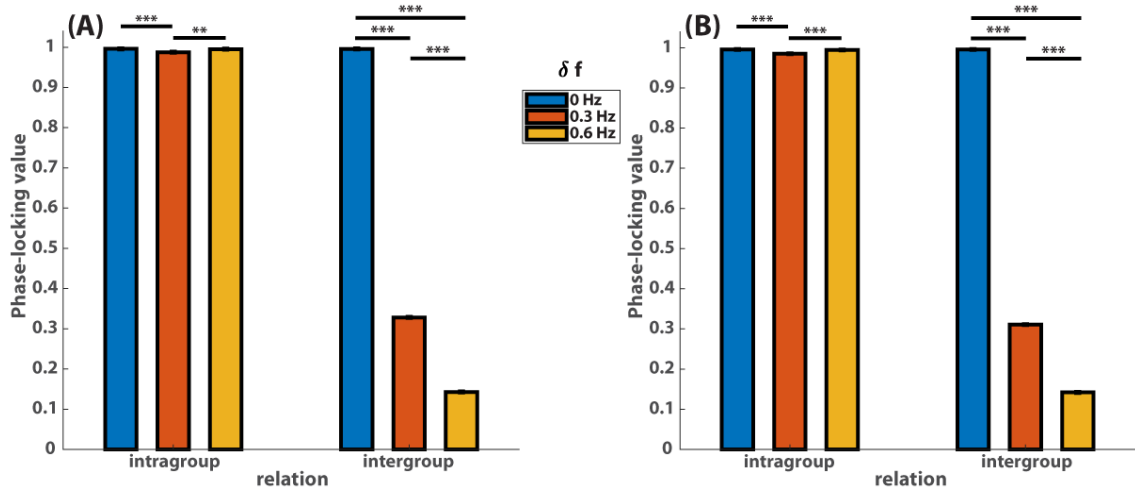


Figure B.5: Intragroup and intergroup phase-locking by different levels of diversity δf for simulated data with identical natural frequency within groups. (A) shows the results of simulations with uniform coupling, and (B) non-uniform coupling (a 's and b 's are randomly distributed in the interval $[0, 0.2]$ see text for details).

B.5 RANDOM COUPLING

To study the effect of symmetry breaking in coupling strength, we generated random coefficients for equation (3.1), following a uniform distribution on the interval $[0, a_{max}]$,

$$P(a) = \frac{1}{a_{max}}. \quad (\text{B.2})$$

We simulated 200 trials for each parameter pair ($\delta f = 0.3 \text{ Hz}, a_{max}$) for $a_{max} \in [0, 1]$ (discretized into intervals of length 0.01) with initial phases randomly distributed

from 0 to π and natural frequencies following the empirical distribution from the human experiment (see Empirical distribution of tapping frequency around metronome frequency). We then find the value of $a_{max} = 0.2$, which produces the level of intergroup integration (β_1) closest to the experimental value (0.31). Using this fitted a_{max} , we simulated 200 trials with no intragroup dispersion in natural frequency, which were used to produce results in Figure B.5B.

B.6 INTERGROUP RELATION WITHOUT SECOND ORDER COUPLING

To examine whether the second order coupling term (i.e. $b \sum \sin 2\phi_{ij}$) in equation (3.3) is necessary for reproducing key experimental results, we let $b = 0$ and followed the exact same analysis as for the case of $b \neq 0$. The results are shown in Figure B.6 (its $b \neq 0$ counterpart is Figure B.1D), and Figure B.7AB (its $b \neq 0$ counterpart is Figure 3.3CD).

Figure B.6 shows the organization of the parameter space $\delta f \times a$ in terms of the level of integration between groups (β_1 , see definition in main text). Similar to Figure B.1D (for $b \neq 0$), the space consists of three regions - complete integration ($\beta_1 \approx 1$, yellow), partial integration ($\beta_1 \ll 1$, red), and segregation ($\beta_1 < 0$, blue) - arranged from upper right to lower left. Figure B.6 is approximately a scaled version of Figure B.1D along a .

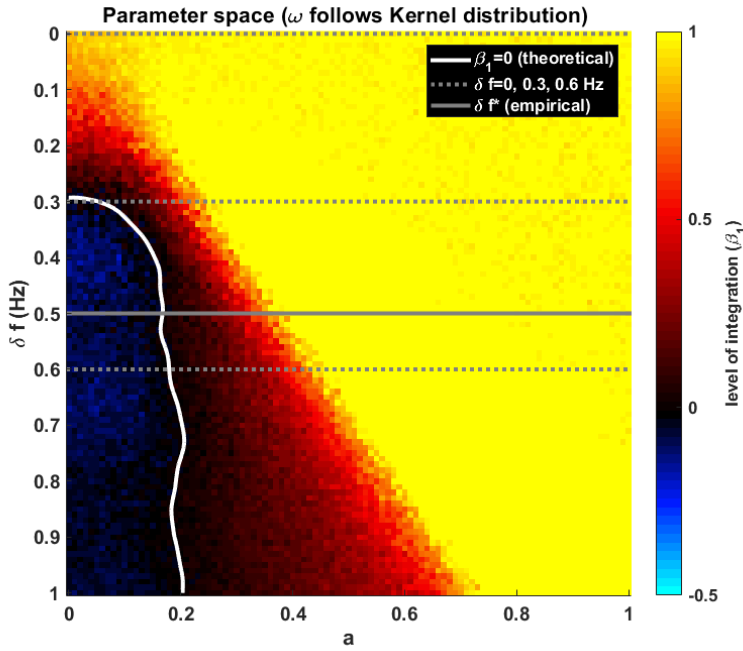


Figure B.6: Level of integration between groups by δf and a , with $b = 0$. See Figure B.1D for interpretation.

We estimated the coupling strength to be $a = 0.154$, where the corresponding level of integration for $\delta f = 0.3$ Hz is the closest to the empirical value (up to 10^{-3} precision for a ; for $a = 0.154$, $\beta_1(0.3\text{Hz}) = 0.29$, the empirical value is 0.31). The corresponding relations between intragroup and intergroup coordination is shown in Figure B.7A and average intra/intergroup coordination in Figure B.7B for different levels of δf .

In Figure B.7A, each dot represents a particular trial with its x-coordinate indicating the average intragroup coordination (measured by phase-locking value, see Materials and Methods in main text) and y-coordinate the average intergroup coordination, whereas the color indicates the diversity δf . Similar to the human experiment and the case of $b \neq 0$, more intragroup coordination is associated with more intergroup coordination (i.e. integration) for $\delta f = 0$ and 0.3 Hz (blue, red regression lines with positive slopes), and less intergroup coordination (i.e. segregation) for $\delta f = 0.6$ Hz (yellow regression line with negative slope). Two differences are (1) the β_1 for

$\delta f = 0.6$ Hz is not significantly different from zero ($p > 0.05$; see main text for more statistics), whereas the counterpart in the human data and the case of $b \neq 0$ are ($p < 0.05$); (2) in the human data and the case of $b \neq 0$, three regression lines intersect at almost the same point (see Figure 3.3A, C), which is not the case for $b = 0$ (Figure B.7A).

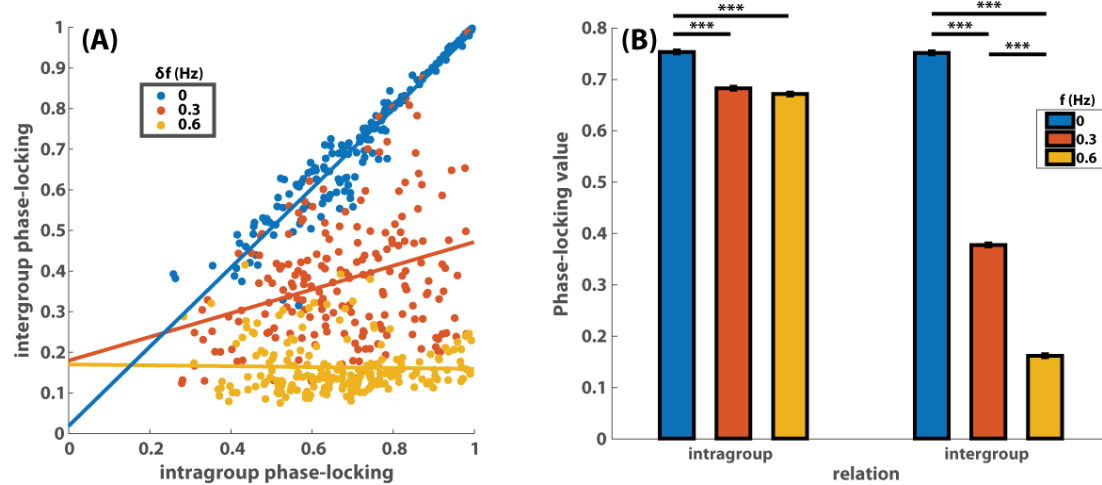


Figure B.7: Intragroup, intergroup coordination and the relationship between them for $a = 0.154$ and $b = 0$. Here the level of coordination is measured by phase-locking value (see main text for definitions). (A) shows the relationship between intragroup (x-coordinate of each dot) and intergroup coordination (y-coordinate of each dot) for different levels of diversity (color code). The solid lines are corresponding regression lines whose slope quantifies the level of integration between two frequency groups. (B) shows the average intragroup (left three bars) and intergroup coordination (right three bars) for different levels of diversity (color code).

In Figure B.7B, we show the average level of intragroup and intergroup coordination (again, in terms of phase-locking values). Intragroup coordination is reduced by the presence of intergroup difference (red, yellow bars on the left significantly shorter than blue bar). Intergroup coordination is more dramatically reduced by intergroup difference. Overall, these results resemble the human data and the case of $b \neq 0$.

B.7 THE DYNAMICS OF RELATIVE PHASES AND ITS LINEAR STABILITY ANALYSIS

From the absolute phase dynamics equation (3.3), we can derive *relative phase* dynamics between N oscillators

$$\begin{aligned}\dot{\phi}_i = & \delta\omega_i - a \sin \phi_i - b \sin 2\phi_i \\ & - a \sum_{j=1}^{N-1} \left[\sin \phi_j + \sin(\phi_i - \phi_j) \right] - b \sum_{j=1}^{N-1} \left[\sin 2\phi_j + \sin 2(\phi_i - \phi_j) \right]\end{aligned}\quad (\text{B.3})$$

where $\phi_i := \phi_{1,i+1} = \varphi_1 - \varphi_{i+1}$ is the relative phase between the 1st and the $(i+1)$ th oscillator (dot is the time derivative), and $\delta\omega_i := \omega_1 - \omega_{i+1}$ difference in natural frequency between them. Equation (B.3) is put into the present form to show its similarity (first row) and difference (second row) with the extended HKB (equation 3.2). In particular, the second row in equation (B.3) shows why dyadic relations embedded in a larger group do not entirely behave like isolated dyads as concluded from the human experiment [35]. Moreover, this system per se can behave like a system of coupled oscillators under metastable coordination (see Section 3.2.6).

Below we show the linear stability analysis of equation (B.3) near a fixed point where oscillators are either inphase or antiphase to each other (see [40] for a more concise and formal version based on absolute phases).

We first scale the dynamics such that (with another abuse of notation) $\dot{\phi}_i = \frac{d\phi_i}{d\tau}$ where $\tau = at$, and have

$$\begin{aligned}\dot{\phi}_i = & \delta\omega_i/a - \sin \phi_i - b/a \sin 2\phi_i \\ & - \sum_{j=1}^{N-1} \left[\sin \phi_j + \sin(\phi_i - \phi_j) \right] - b/a \sum_{j=1}^{N-1} \left[\sin 2\phi_j + \sin 2(\phi_i - \phi_j) \right].\end{aligned}$$

We only consider the simple case $\delta\omega_1 = \dots = \delta\omega_{N-1} = 0$ (identical oscillators),

and define $\kappa := 2b/a$,

$$\begin{aligned}\dot{\phi}_i &= -\sin \phi_i - \kappa/2 \sin 2\phi_i \\ &\quad - \sum_{j=1}^{N-1} \left[\sin \phi_j + \sin(\phi_i - \phi_j) \right] - \kappa/2 \sum_{j=1}^{N-1} \left[\sin 2\phi_j + \sin 2(\phi_i - \phi_j) \right]\end{aligned}$$

with Jacobian matrix whose elements are

$$\begin{aligned}J_{ik} &= \frac{\partial f_i}{\partial \phi_k} \\ &= \begin{cases} i = k : & -2 \cos \phi_k - 2\kappa \cos 2\phi_k - \sum_{j=1, j \neq k}^{N-1} \left[\cos(\phi_k - \phi_j) + \kappa \cos 2(\phi_k - \phi_j) \right] \\ i \neq k : & -\cos \phi_k + \cos(\phi_i - \phi_k) - \kappa \cos 2\phi_k + \kappa \cos 2(\phi_i - \phi_k) \end{cases}.\end{aligned}$$

We are only concerned with fixed points whose components are either inphase or antiphase. If there is at least one antiphase, the fixed point reflects a configuration of two clusters that are inphase within themselves, but antiphase between each other. Without loss of generality, we let n_+ be the size of the larger or equal-sized cluster, and n_- the smaller or equal-sized cluster, i.e. $n_+ \geq n_- > 0$ and $n_+ + n_- = N$. We name the oscillators in the first cluster $\varphi_1, \dots, \varphi_{n_+}$, whose relations are described by relative phases $\phi_1, \dots, \phi_{n_+-1}$; and we name the oscillators in the second cluster $\varphi_{n_++1}, \dots, \varphi_N$, whose relations to the first cluster are $\phi_{n_+}, \dots, \phi_{N-1}$. In other words, we want to evaluate the Jacobian at fixed points $\Phi = (\phi_1, \dots, \phi_{N-1})$ where the first $(n_+ - 1)$ relative phases $\phi_1 = \dots = \phi_{n_+-1} = 0$ and the last n_- relative phases $\phi_{n_+} = \dots = \phi_{N-1} = \pi$, with $n_+ \geq n_- = N - n_+$.

$$J_{ik}|_{\Phi} = \begin{cases} i = k : & -\cos \phi_k \left(2 + \sum_{j=1, j \neq k}^{N-1} \cos \phi_j \right) - \kappa N \\ & = \begin{cases} k < n_+ : & -(2 + n_+ - 2 - n_-) - \kappa N = n_- - n_+ - \kappa N \\ k \geq n_+ : & \left[2 + (n_+ - 1) - (n_- - 1) \right] - \kappa N = 2 + n_+ - n_- - \kappa N \end{cases} \\ i \neq k : & \cos \phi_k (\cos \phi_i - 1) \\ & = \begin{cases} i < n_+, k < n_+ : & 0 \\ i < n_+, k \geq n_+ : & 0 \\ i \geq n_+, k < n_+ : & -2 \\ i \geq n_+, k \geq n_+ : & 2 \end{cases} \end{cases} .$$

We can see that the Jacobian evaluated at our fixed point is a block-triangular matrix

$$\mathbf{J} = \begin{bmatrix} \alpha \mathbf{I}_{(n_+ - 1) \times (n_+ - 1)} & \mathbf{0}_{(n_+ - 1) \times n_-} \\ -\mathbf{2}_{n_- \times (n_+ - 1)} & \mathbf{2}_{n_- \times n_-} + \beta \mathbf{I}_{n_- \times n_-} \end{bmatrix} \quad (\text{B.4})$$

where $\alpha = n_- - n_+ - \kappa N$ and $\beta = n_+ - n_- - \kappa N$.

Now we find the eigenvalues

$$|\mathbf{J} - \lambda \mathbf{I}| = \begin{vmatrix} (\alpha - \lambda) \mathbf{I}_{(n_+ - 1) \times (n_+ - 1)} & \mathbf{0}_{(n_+ - 1) \times n_-} \\ -\mathbf{2}_{n_- \times (n_+ - 1)} & \mathbf{2}_{n_- \times n_-} + (\beta - \lambda) \mathbf{I}_{n_- \times n_-} \end{vmatrix} \quad (\text{B.5})$$

$$= |(\alpha - \lambda) \mathbf{I}_{(n_+ - 1) \times (n_+ - 1)}| |\mathbf{2}_{n_- \times n_-} + (\beta - \lambda) \mathbf{I}_{n_- \times n_-}| = 0. \quad (\text{B.6})$$

The eigenvalues of $\mathbf{2}_{n_- \times n_-}$ can be calculated through discrete Fourier transform. Thus we have

$$\lambda_1 = \dots = \lambda_{n_+ - 1} = \alpha \quad (\text{B.7})$$

$$\lambda_{n_+} = 2n_- + \beta \quad (\text{B.8})$$

$$\lambda_{n_+ + 1} = \dots = \lambda_{N-1} = \beta. \quad (\text{B.9})$$

Because of $n_+ \geq n_- > 0$, we have $\alpha < \beta$. This makes λ_{n_+} the largest eigenvalue. Thus for the antiphase-containing fixed points to be stable, we need $2n_- + \beta = N(1 - \kappa) < 0$, which implies $\kappa > 1$. Since we have repeated eigenvalues and J generally not a diagonal matrix, this is a degenerate fixed point but nevertheless asymptotically stable for $\kappa > 1$.

There is of course an all-inphase fixed point (i.e. $n_+ = N, n_- = 0$), for which all eigenvalues $\lambda_1 = \dots = \lambda_{N-1} = \alpha$. In this case, $\alpha = -(1 + \kappa)N$, which is always negative (in the present analysis, we assume $a > 0, b \geq 0$ thus $\kappa \geq 0$), i.e. the all-inphase fixed point is always stable.

B.8 ADDITIONAL TRIADIC DYNAMICS

Here we provide in Figure B.8 two additional variations of the simulated triadic dynamics shown in Figure 3.5B. Figure B.8A shows what happens when all three oscillators have the identical coupling style, i.e. $a_1 = a_3 = a_4$ and $b_1 = b_3 = b_4$ (keeping the same mean coupling strength as Figure 3.5B and C). With the symmetry completed restored (in contrast to Figure 3.5C where only the symmetry between agent 3 and 4 is restored), not only the “bumps” in ϕ_{34} are gone but also the metastability altogether (at least at the observable time scale). This further illustrates the role of symmetry breaking in understanding the single-trial dynamics.

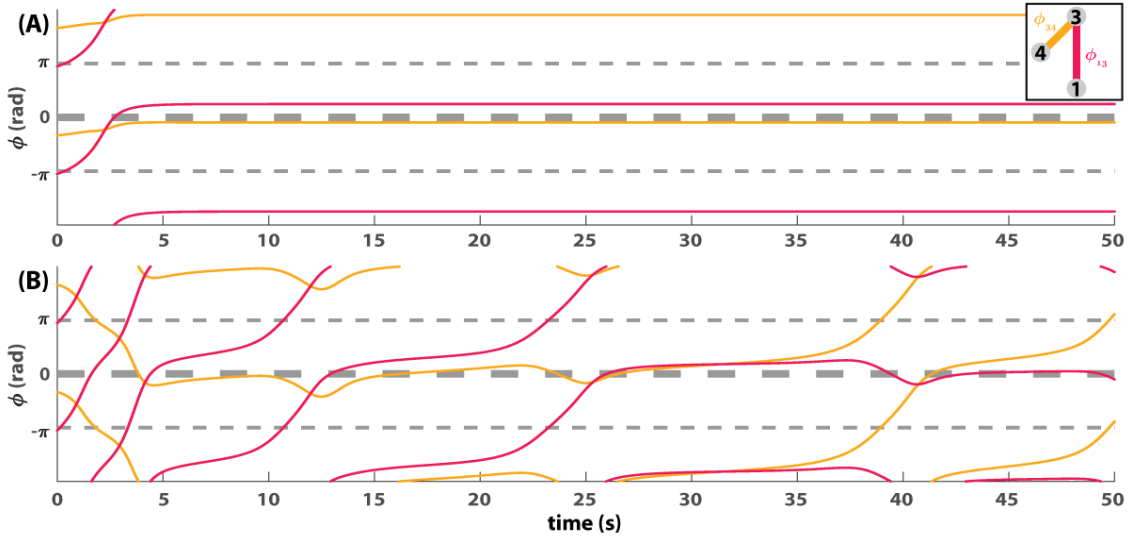


Figure B.8: Simulated triadic coordination as a pair of relative phases, with (A) $a_1 = a_3 = a_4 = 0.4033$ and (B) varying natural frequency ω_3 .

Figure B.8B shows what happens when agent 3's natural frequency is not constant. A main clue suggesting a non-constant natural frequency is the increasing size of “bumps” in ϕ_{34} observed in the human behavior (see Figure 3.5A, the bump in yellow line at 15s was smaller than the one at 25s, and even smaller than the one at 37s) which was accompanied by growing length of the dwells of ϕ_{13} (red trajectory in Figure 3.5A has three periods of flattening, each one longer than the previous one). This could simply mean that agent 3's “natural frequency” was moving towards agent 1's and away from agent 4's. In the model, the natural frequencies of agent 1 and 4 are 1.57 and 1.45 Hz respectively. We simply let ω_3 increase linearly from 1.2 Hz to 1.7 Hz, instead of being constant (i.e. 1.375 Hz for Figure 3.5BC and B.8A), over the course of the trial. The resulted dynamics is shown in Figure B.8B. We see the dwells of ϕ_{13} (red line flattening around 7, 17 and 32s) are getting longer over time as the bumps in ϕ_{34} (yellow line) grow (the last bump grows out of itself at 37s and leaves inphase). In fact, at the end of the last dwell (around 37s) ϕ_{13} is no longer metastable in the original sense but begins to oscillate around inphase $\phi = 0$, whereas

ϕ_{34} takes its place at that time and becomes metastable (i.e. after 37s yellow line starts wrapping).

Gradually increasing natural frequency of agent 3 (ω_3) creates two subtle effects in addition to the increasing bump size. The first has already been hinted at that a gradual change of parameter can cause ϕ_{34} to suddenly leave inphase (~ 37 s yellow line in Figure B.8B). In the human trial (Figure 3.5A), ϕ_{34} had also, after the third bump, left inphase (37s). The difference is that the humans left for antiphase, instead of becoming metastable as for our simple model assuming linearly increasing natural frequency. This suggests that there was, unsurprisingly, more interesting adaptation going on in human movement frequency than just a linear ramping. Another subtle effect is of the same flavor but is concerned with what happens before ϕ_{34} began to dwell at inphase. In the human trial, ϕ_{34} decreased for almost one cycle before it stopped at inphase (0-10s yellow line in Figure 3.5A). This is not the case with constant frequency (Figure 3.5B, yellow line, ϕ_{34} immediately increases to inphase after the beginning of the trial), but it is the case with varying frequency (Figure B.8B, yellow line, 0-5s). All these show, by a very simple example, how gradual adaptation in natural frequency may cause sudden changes in coordination patterns.

B.9 ADDITIONAL COMPARISONS REGARDING TRIADIC METASTABLE PATTERNS

Here we show a few more examples of triadic metastability (Figure B.9 and B.10) supplementing Figure 3.6 and 3.7 in Chapter 3. Figure B.9 A1-3 shows that the topology of the relative phase orbit does not change in a neighborhood near $\lambda = 0.5$ ([0.49, 0.51]), i.e. remains of type (1, 1) as in Figure 3.7 C1-3. It means that the topology shown in Figure B.9 A2-3 and Figure 3.7 C2-3 is structurally stable with respect to λ . This is not the case for Figure 3.6 A2-3. As for any arbitrarily small neighborhood of $\lambda = 0.5$, there exist irrational numbers which leads to quasiperiodic

orbits, i.e. not of type (1, 1). The structural stability of orbits in Figure 3.7 C2-3 is due to the presence of coupling.

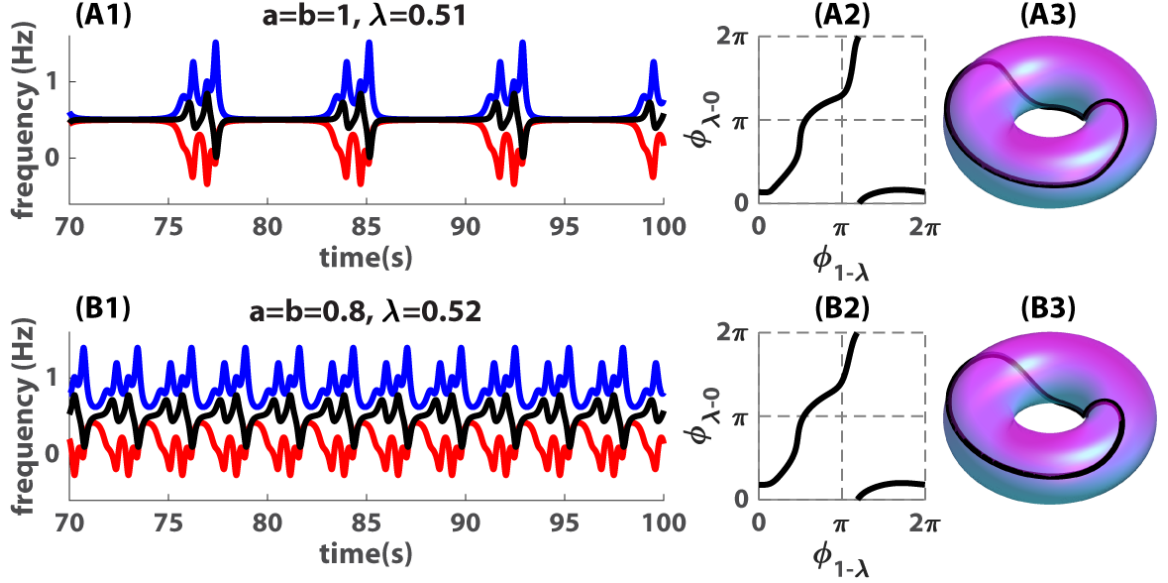


Figure B.9: Additional examples of simulated triadic metastability. (A1) and (B1) show the frequency dynamics of three oscillators whose natural frequencies are 0 (red), λ (black) and 1 (blue) Hz, interacting with each other under the coupling strength $a = b$ (values shown in A1, B1). The corresponding periodic orbits of relative phases are shown in (A2-3) and (B2-3) respectively, both of the same type (1, 1).

In comparison to Figure 3.7 A1-3, Figure B.9 B1-3 shows how reducing coupling strength affects the regimes of different metastable patterns. $\lambda = 0.52$ belongs to the regime of type (0, 1) under the coupling $a = b = 1$ (Figure 3.7 A2-3) but becomes part of the regime of type (1, 1) when the coupling is weakened $a = b = 0.8$ (Figure B.9 B2-3). This indicates a reduction in the measure of the regime of type (0, 1) and an increase in that of type (1, 1).

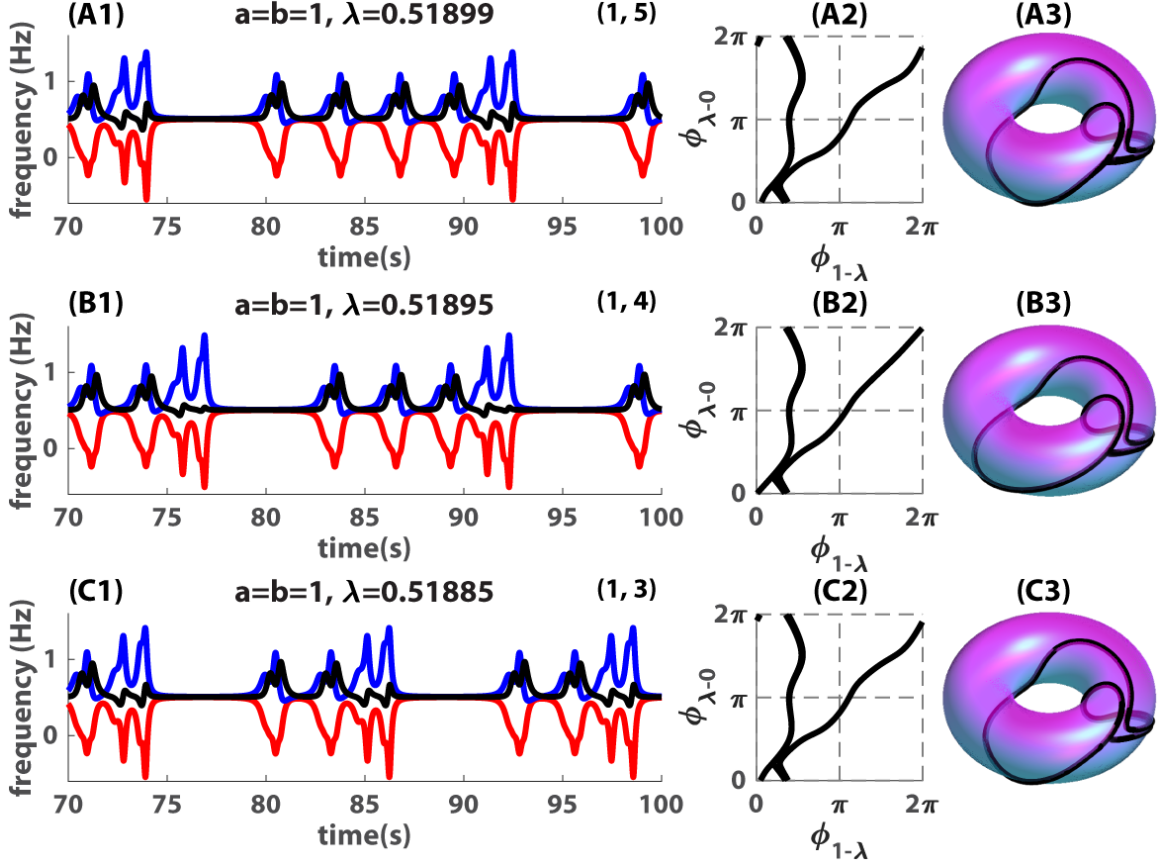


Figure B.10: Sequence production in triadic metastable coordination. Three more values of λ are added here as an extension to Figure 3.7, where all other parameters are the same. Winding numbers of each pattern is shown in the upper right corner of A1-C1, which is measured by the amount of change in $\phi_{1-\lambda}$ and $\phi_{\lambda=0}$ (divided by 2π) in each cycle.

We show three additional examples of triadic metastable patterns of type (1, 3), (1, 4), (1, 5) (Figure B.10 C1-3, B1-3, A1-3 respectively) found recursively between patterns in Figure 3.7 A1-3 and B1-3 of type (0, 1) and (1, 2). One can clearly see the composition of patterns in the sum of winding numbers, e.g. $(1, 3) = (0, 1) + (1, 2)$ in the frequency dynamics (C1), which amounts to adding one cycle from Figure 3.7 A1 to Figure 3.7 B1. In fact, from Figure B.10 C1 to A1, we see a primitive kind of sequence production by adding repeatedly the same cycle of type (0, 1) in front. The same information is not as clear in the relative phase orbits in Figure B.10 A2-C2 and A3-C3 (except under extreme magnification, not shown), because $\phi_{1-\lambda}$ changes

unintelligibly slowly for the first part of each cycle (seen as overlapping blue and black curves in A1-C1). As a result, the orbit wraps very close to itself around the meridian circle.

BIBLIOGRAPHY

- [1] Waddington, C. H. *How Animals Develop* (Harper & Brothers, New York, 1962).
- [2] Spencer, H. The social organism. *Westminster review* **73**, 90–121 (1860).
- [3] Zipf, G. K. *National unity and disunity; the nation as a bio-social organism.* (Principia Press, Oxford, England, 1941).
- [4] Simon, H. A. The organization of complex systems. In *Hierarchy Theory: The Challenge of Complex Systems*, 245–261 (1977).
- [5] West, G. B. *Scale: The Universal Laws of Growth, Innovation, Sustainability, and the Pace of Life in Organisms, Cities, Economies, and Companies* (Penguin Press, New York, New York, USA, 2017).
- [6] Holland, J. H. *Emergence: from Chaos to Order.* (Addison-Wesley, Redwood City, CA, 1998).
- [7] Wolfram, S. *A New Kind of Science* (Wolfram media, Champaign, IL, 2002).
- [8] Miller, J. H. & Page, S. E. *Complex Adaptive Systems: an Introduction to Computational Models of Social Life* (Princeton university press, 2009).
- [9] Emsley, J. *The elements* (Oxford University Press, New York, 1998).
- [10] Cajaiba-Santana, G. Social innovation: Moving the field forward. A conceptual framework. *Technological Forecasting and Social Change* **82**, 42–51 (2014).
- [11] Cohen, A. K. *Delinquent Boys: the Culture of the Gang* (Free Press, New York, NY, 1955).
- [12] Kuramoto, Y. *Chemical Oscillations, Waves, and Turbulence*, vol. 19 of *Springer Series in Synergetics* (Springer Berlin Heidelberg, Berlin, Heidelberg, 1984).
- [13] Kelso, J. A. S., Del Colle, J. D. & Schöner, G. Action-perception as a pattern formation process. In Jeannerod, M. (ed.) *Attention and Performance 13: Motor Representation and Control*, vol. 45, 139–169 (Lawrence Erlbaum Associates, Inc, Hillsdale, NJ, US, 1990).
- [14] Haken, H. Cooperative phenomena in systems far from thermal equilibrium and in nonphysical systems. *Reviews of Modern Physics* **47**, 67–121 (1975).

- [15] Haken, H. *Advanced Synergetics: Instability Hierarchies of Self-Organizing Systems and Devices* (Springer-Verlag Berlin Heidelberg, 1983).
- [16] Haken, H. *Synergetics: Introduction and Advanced Topics* (Springer Berlin Heidelberg, Berlin, Heidelberg, 2004).
- [17] Haken, H. *The Science of Structure: Synergetics* (Van Nostrand Reinhold, New York, NY, 1984).
- [18] Winfree, A. T. vol. 12 of *Interdisciplinary Applied Mathematics* (Springer New York, New York, NY, 2001).
- [19] Strogatz, S. H. & Stewart, I. Coupled oscillators and biological synchronization. *Scientific American* **269**, 102–109 (1993).
- [20] Okuda, K. Variety and generality of clustering in globally coupled oscillators. *Physica D: Nonlinear Phenomena* **63**, 424–436 (1993).
- [21] Komarov, M. & Pikovsky, A. Multiplicity of singular synchronous states in the Kuramoto model of coupled oscillators. *Physical Review Letters* **111**, 204101 (2013).
- [22] Komarov, M. & Pikovsky, A. The Kuramoto model of coupled oscillators with a bi-harmonic coupling function. *Physica D: Nonlinear Phenomena* **289**, 18–31 (2014).
- [23] Li, K., Ma, S., Li, H. & Yang, J. Transition to synchronization in a Kuramoto model with the first- and second-order interaction terms. *Physical Review E* **89**, 032917 (2014).
- [24] Von Holst, E. On the nature of order in the central nervous system. In *The Collected Papers of Erich von Holst Vol. 1, The Behavioral Physiology of Animal and Man*, 3–32 (University of Miami Press, Coral Gables, FL., 1973).
- [25] Golubitsky, M., Stewart, I., Buono, P.-L. L. & Collins, J. J. Symmetry in locomotor central pattern generators and animal gaits. *Nature* **401**, 693–695 (1999).
- [26] Grillner, S. Control of locomotion in bipeds, tetrapods, and fish. In Pollock, D. M. (ed.) *Comprehensive Physiology* (John Wiley & Sons, Inc., Hoboken, NJ, USA, 2011).
- [27] Haken, H., Kelso, J. A. S. & Bunz, H. A theoretical model of phase transitions in human hand movements. *Biological Cybernetics* **51**, 347–356 (1985).
- [28] Kelso, J. A. S. *Dynamic Patterns: The Self-Organization of Brain and Behavior* (The MIT Press, Cambridge, Massachusetts, 1995).

- [29] Kelso, J. A. S. Phase transitions and critical behaviour in human bimanual coordination. *American Journal of Physiology: Regulatory, Integrative and Comparative Physiology* **246**, R1000–1004 (1984).
- [30] Jeka, J. J. & Kelso, J. A. S. Manipulating symmetry in the coordination dynamics of human movement. *Journal of experimental psychology. Human perception and performance* **21**, 360–374 (1995).
- [31] Tognoli, E. & Kelso, J. A. S. Brain coordination dynamics: true and false faces of phase synchrony and metastability. *Progress in Neurobiology* **87**, 31–40 (2009).
- [32] Kelso, J. A. S. Multistability and metastability: understanding dynamic coordination in the brain. *Philosophical Transactions of the Royal Society B: Biological Sciences* **367**, 906–918 (2012).
- [33] Tognoli, E. & Kelso, J. A. S. The metastable brain. *Neuron* **81**, 35–48 (2014).
- [34] Tognoli, E., Zhang, M. & Kelso, J. A. S. On the nature of coordination in nature. In *Advances in Cognitive Neurodynamics (VI)*, 375–382 (Springer Nature Singapore, 2018).
- [35] Zhang, M., Kelso, J. A. S. & Tognoli, E. Critical diversity: Divided or united states of social coordination. *PLOS ONE* **13**, e0193843 (2018).
- [36] Bressler, S. L. & Kelso, J. A. S. Cortical coordination dynamics and cognition. *Trends in Cognitive Sciences* **5**, 26–36 (2001).
- [37] Kelso, J. A. S. & Engstrom, D. A. *The Complementary Nature* (The MIT Press, Cambridge, Massachusetts, 2006).
- [38] Schöner, G. & Kelso, J. A. S. A dynamic pattern theory of behavioral change. *Journal of Theoretical Biology* **135**, 501–524 (1988).
- [39] Jeka, J. J., Kelso, J. A. S. & Kiemel, T. Pattern switching in human multilimb coordination dynamics. *Bulletin of Mathematical Biology* **55**, 829–845 (1993).
- [40] Zhang, M., Beetle, C., Kelso, J. A. S. & Tognoli, E. Connecting coordination across scales (In review).
- [41] Camazine, S. *et al.* *Self-Organization in Biological Systems* (Princeton University Press, 2003).
- [42] Brown, F. A. Living clocks: the clocks are accounted for as "open systems" depending upon subtle geophysical rhythms. *Science (New York, N.Y.)* **130**, 1535–1544 (1959).
- [43] Wunderlich, F. M. Symphonies of urban places: urban rhythms as traces of time in space a study of urban rhythms '. *Place and Location Studies in Environmental Aesthetics and Semiotics VI* 91–111 (2008).

- [44] Glass, L. Synchronization and rhythmic processes in physiology. *Nature* **410**, 277–284 (2001).
- [45] Buzsáki, G. *Rhythms of the Brain* (Oxford University Press, 2006).
- [46] Blasius, B., Huppert, A. & Stone, L. Complex dynamics and phase synchronization in spatially extended ecological systems. *Nature* **399**, 354–359 (1999).
- [47] Repp, B. H. Sensorimotor synchronization: a review of the tapping literature. *Psychonomic Bulletin & Review* **12**, 969–992 (2005).
- [48] Schöner, G. & Kelso, J. A. S. Dynamic pattern generation in behavioral and neural systems. *Science* **239**, 1513–1520 (1988).
- [49] Assisi, C. G., Jirsa, V. K. & Kelso, J. A. S. Dynamics of multifrequency coordination using parametric driving: theory and experiment. *Biological Cybernetics* **93**, 6–21 (2005).
- [50] Peper, C., Beek, P. J. & van Wieringen, P. C. W. Multifrequency coordination in bimanual tapping: Asymmetrical coupling and signs of supercriticality. *Journal of Experimental Psychology: Human Perception and Performance* **21**, 1117–1138 (1995).
- [51] Oullier, O., de Guzman, G. C., Jantzen, K. J., Lagarde, J. & Kelso, J. A. S. Social coordination dynamics: measuring human bonding. *Social Neuroscience* **3**, 178–192 (2008).
- [52] Richardson, M. J., Marsh, K. L., Isenhower, R. W., Goodman, J. R. L. & Schmidt, R. C. Rocking together: dynamics of intentional and unintentional interpersonal coordination. *Human Movement Science* **26**, 867–891 (2007).
- [53] Tognoli, E., Lagarde, J., DeGuzman, G. C. & Kelso, J. A. S. The phi complex as a neuromarker of human social coordination. *Proceedings of the National Academy of Sciences* **104**, 8190–8195 (2007).
- [54] Dumas, G., Nadel, J., Soussignan, R., Martinerie, J. & Garnero, L. Inter-brain synchronization during social interaction. *PLOS ONE* **5**, e12166 (2010).
- [55] Noy, L., Dekel, E. & Alon, U. The mirror game as a paradigm for studying the dynamics of two people improvising motion together. *Proceedings of the National Academy of Sciences* **108**, 20947–20952 (2011).
- [56] Hasson, U., Ghazanfar, A. A., Galantucci, B., Garrod, S. & Keysers, C. Brain-to-brain coupling: a mechanism for creating and sharing a social world. *Trends in Cognitive Sciences* **16**, 114–121 (2012).
- [57] Schmidt, R. C., Carello, C. & Turvey, M. T. Phase transitions and critical fluctuations in the visual coordination of rhythmical movements between people. *Journal of Experimental Psychology: Human Perception and Performance* **16**, 227–247 (1990).

- [58] Varela, F., Lachaux, J. P., Rodriguez, E. & Martinerie, J. The brainweb: phase synchronization and large-scale integration. *Nature reviews. Neuroscience* **2**, 229–239 (2001).
- [59] Kelso, J. A. S., de Guzman, G. C., Reveley, C. & Tognoli, E. Virtual Partner Interaction (VPI): Exploring novel behaviors via coordination dynamics. *PLOS ONE* **4**, e5749 (2009).
- [60] Dumas, G., de Guzman, G. C., Tognoli, E. & Kelso, J. A. S. The human dynamic clamp as a paradigm for social interaction. *Proceedings of the National Academy of Sciences* **111**, E3726–E3734 (2014).
- [61] Kostrubiec, V., Dumas, G., Zanone, P.-G. & Kelso, J. A. S. The Virtual Teacher (VT) paradigm: learning new patterns of interpersonal coordination using the Human Dynamic Clamp. *PLOS ONE* **10**, e0142029 (2015).
- [62] Lagarde, J., Peham, C., Licka, T. & Kelso, J. A. S. Coordination dynamics of the horse-rider system. *Journal of Motor Behavior* **37**, 418–424 (2005).
- [63] Pfau, T., Spence, A., Starke, S., Ferrari, M. & Wilson, A. Modern riding style improves horse racing times. *Science (New York, N.Y.)* **325**, 289 (2009).
- [64] Fuchs, A., Jirsa, V. K., Haken, H. & Kelso, J. A. S. Extending the HKB model of coordinated movement to oscillators with different eigenfrequencies. *Biological Cybernetics* **74**, 21–30 (1996).
- [65] Schöner, G., Haken, H. & Kelso, J. A. S. A stochastic theory of phase transitions in human hand movement. *Biological cybernetics* **53**, 247–257 (1986).
- [66] Schöner, G., Jiang, W. Y. & Kelso, J. A. S. A synergetic theory of quadrupedal gaits and gait transitions. *Journal of Theoretical Biology* **142**, 359–391 (1990).
- [67] Collins, J. J. & Stewart, I. Coupled nonlinear oscillators and the symmetries of animal gaits. *Journal of Nonlinear Science* **3**, 349–392 (1993).
- [68] Kelso, J. A. S. & Jeka, J. J. Symmetry breaking dynamics of human multilimb coordination. *Journal of Experimental Psychology: Human Perception and Performance* **18**, 645–668 (1992).
- [69] Buck, J. & Buck, E. Synchronous fireflies. *Scientific American* **234**, 74–85 (1976).
- [70] Edelman, G. M. & Tononi, G. S. Reentry and the dynamic core: neural correlates of conscious experience. In Metzinger, T. (ed.) *Neural Correlates of Consciousness* (MIT Press, 2000).
- [71] Néda, Z., Ravasz, E., Brechet, Y., Vicsek, T. & Barabási, A.-L. The sound of many hands clapping. *Nature* **403**, 849–850 (2000).

- [72] Strogatz, S. H. From Kuramoto to Crawford: exploring the onset of synchronization in populations of coupled oscillators. *Physica D: Nonlinear Phenomena* **143**, 1–20 (2000).
- [73] Néda, Z., Ravasz, E., Vicsek, T., Brechet, Y. & Barabási, A.-L. L. Physics of the rhythmic applause. *Physical Review E - Statistical Physics, Plasmas, Fluids, and Related Interdisciplinary Topics* **61**, 6987–6992 (2000).
- [74] Mirocco, R. E. & Strogatz, S. H. Synchronization of pulse-coupled biological oscillators. *SIAM Journal on Applied Mathematics* **50**, 1645–1662 (1990).
- [75] Richardson, M. J., Garcia, R. L., Frank, T. D., Gergor, M. & Marsh, K. L. Measuring group synchrony: a cluster-phase method for analyzing multivariate movement time-series. *Frontiers in Physiology* **3**, 1–10 (2012).
- [76] Fuchs, A. *Nonlinear Dynamics in Complex Systems* (Springer Berlin Heidelberg, Berlin, Heidelberg, 2013).
- [77] Kelso, J. A. S. The dynamic brain in action: coordinative structures, criticality, and coordination dynamics. In Plenz, D. & Niebur, E. (eds.) *Criticality in Neural Systems*, chap. 4, 67–104 (2014).
- [78] de Guzman, G. C. & Kelso, J. A. S. Multifrequency behavioral patterns and the phase attractive circle map. *Biological Cybernetics* **64**, 485–495 (1991).
- [79] Kelso, J. A. S. & de Guzman, G. C. Order in time: how the cooperation between the hands informs the design of the brain. In Haken, H. (ed.) *Neural and Synergetic Computers*, 180–196 (Springer Berlin Heidelberg, Berlin, Heidelberg, 1988).
- [80] Strogatz, S. H. *Sync: The Emerging Science of Spontaneous Order* (Hyperion, New York, New York, USA, 2003), 1st edn.
- [81] Buck, J. Synchronous rhythmic flashing of fireflies. II. *The Quarterly Review of Biology* **63**, 265–289 (1988).
- [82] Buzsáki, G. Theta rhythm of navigation: link between path integration and landmark navigation, episodic and semantic memory. *Hippocampus* **15**, 827–840 (2005).
- [83] Alderisio, F., Bardy, B. G. & di Bernardo, M. Entrainment and synchronization in networks of Rayleighvan der Pol oscillators with diffusive and HakenKelsoBunz couplings. *Biological Cybernetics* **110**, 151–169 (2016).
- [84] Nishikawa, T. & Motter, A. E. Symmetric states requiring system asymmetry. *Physical Review Letters* **117**, 1–5 (2016).
- [85] Valdesolo, P. & DeSteno, D. Synchrony and the social tuning of compassion. *Emotion* **11**, 262–266 (2011).

- [86] Hove, M. J. & Risen, J. L. It's all in the timing: interpersonal synchrony increases affiliation. *Social Cognition* **27**, 949–960 (2009).
- [87] Zhang, M., Dumas, G., Kelso, J. A. S. & Tognoli, E. Enhanced emotional responses during social coordination with a virtual partner. *International Journal of Psychophysiology* **104**, 33–43 (2016).
- [88] Fogel, A., Nwokah, E., Dedo, J. Y. & Messinger, D. Social process theory of emotion: A dynamic systems approach. *Social Development* **1**, 122–142 (1992).
- [89] Wheatley, T., Kang, O., Parkinson, C. & Looser, C. E. From mind perception to mental connection: synchrony as a mechanism for social understanding. *Social and Personality Psychology Compass* **6**, 589–606 (2012).
- [90] Oullier, O. & Kelso, J. A. S. Social coordination, from the perspective of Coordination Dynamics. In Meyers, R. A. (ed.) *Encyclopedia of Complexity and Systems Science*, 8198–8213 (Springer New York, New York, NY, 2009).
- [91] Schmidt, R. C., Fitzpatrick, P., Caron, R. & Mergeche, J. Understanding social motor coordination. *Human Movement Science* **30**, 834–845 (2011).
- [92] Sekara, V., Stopczynski, A. & Lehmann, S. Fundamental structures of dynamic social networks. *Proceedings of the National Academy of Sciences* **113**, 9977–9982 (2016).
- [93] Boiger, M. & Mesquita, B. The construction of emotion in interactions, relationships, and cultures. *Emotion Review* **4**, 221–229 (2012).
- [94] Carneiro, R. R. L. R. On the relationship between size of population and complexity of social organization. *Southwestern Journal of Anthropology* **23**, 234–243 (1967).
- [95] Changizi, M. A. & He, D. Four correlates of complex behavioral networks: differentiation, behavior, connectivity, and compartmentalization: Carving networks at their joints. *Complexity* **10**, 13–40 (2005).
- [96] Weng, G., Bhalla, U. S. & Iyengar, R. Complexity in biological signaling systems. *Science (New York, N.Y.)* **284**, 92–96 (1999).
- [97] Stouffer, D. B. & Bascompte, J. Compartmentalization increases food-web persistence. *Proceedings of the National Academy of Sciences* **108**, 3648–3652 (2011).
- [98] Kirschner, M. & Gerhart, J. Evolvability. *Proceedings of the National Academy of Sciences* **95**, 8420–8427 (1998).
- [99] Ash, J. & Newth, D. Optimizing complex networks for resilience against cascading failure. *Physica A: Statistical Mechanics and its Applications* **380**, 673–683 (2007).

- [100] Edelman, G. M. & Gally, J. A. Degeneracy and complexity in biological systems. *Proceedings of the National Academy of Sciences* **98**, 13763–13768 (2001).
- [101] Bar-Yam, Y. Multiscale variety in complex systems. *Complexity* **9**, 37–45 (2004).
- [102] Sporns, O. Network attributes for segregation and integration in the human brain. *Current Opinion in Neurobiology* **23**, 162–171 (2013).
- [103] Tononi, G. S., Sporns, O. & Edelman, G. M. A measure for brain complexity: relating functional segregation and integration in the nervous system. *Proceedings of the National Academy of Sciences* **91**, 5033–5037 (1994).
- [104] McPherson, M., Smith-Lovin, L. & Cook, J. M. Birds of a feather: homophily in social networks. *Annual Review of Sociology* **27**, 415–444 (2001).
- [105] Moody, J. Race, school integration, and friendship segregation in America. *American Journal of Sociology* **107**, 679–716 (2001).
- [106] Schelling, T. C. Dynamic models of segregation. *Journal of Mathematical Sociology* **1**, 143–186 (1971).
- [107] Stark, T. H. & Flache, A. The double edge of common interest. *Sociology of Education* **85**, 179–199 (2012).
- [108] Blau, P. M. *Inequality and Heterogeneity : a Primitive Theory of Social Structure* (Free Press, New York, NY, 1977).
- [109] Kelso, J. A. S. Instabilities and phase transitions in human brain and behavior. *Frontiers in Human Neuroscience* **4**, 23 (2010).
- [110] Scheffer, M. *et al.* Early-warning signals for critical transitions. *Nature* **461**, 53–59 (2009).
- [111] Wilson, K. G. Problems in physics with many scales of length. *Scientific American* **241**, 158–179 (1979).
- [112] Schelling, T. C. *Micromotives and Macrobbehavior*. Fels lectures on public policy analysis (Norton, New York, 1978), 1st ed. edn.
- [113] Leibold, M. A. *et al.* The metacommunity concept: a framework for multi-scale community ecology. *Ecology Letters* **7**, 601–613 (2004).
- [114] Parra, J. *et al.* Gamma-band phase clustering and photosensitivity: Is there an underlying mechanism common to photosensitive epilepsy and visual perception? *Brain* **126**, 1164–1172 (2003).
- [115] Tognoli, E. & Kelso, J. A. S. Enlarging the scope: grasping brain complexity. *Frontiers in Systems Neuroscience* **8**, 122 (2014).

- [116] Kelso, J. A. S., Dumas, G. & Tognoli, E. Outline of a general theory of behavior and brain coordination. *Neural Networks* **37**, 120–131 (2013).
- [117] Takamatsu, A., Tanaka, R. & Fujii, T. Hidden symmetry in chains of biological coupled oscillators. *Physical Review Letters* **92**, 228101–228102 (2004).
- [118] Yokoyama, K. & Yamamoto, Y. Three people can synchronize as coupled oscillators during sports activities. *PLoS Computational Biology* **7**, e1002181 (2011).
- [119] Kuramoto, Y. & Battogtokh, D. Coexistence of coherence and incoherence in nonlocally coupled phase oscillators. *Nonlinear Phenomena in Complex Systems* **5**, 380–385 (2002).
- [120] Holling, C. Understanding the complexity of economic, ecological, and social systems. *Ecosystems* **4**, 390–405 (2001).
- [121] Kelso, J. A. S. An essay on understanding the mind. *Ecological Psychology* **20**, 180–208 (2008).
- [122] Palla, G., Barabási, A.-L. & Vicsek, T. Quantifying social group evolution. *Nature* **446**, 664–667 (2007).
- [123] Wang, J., Suri, S. & Watts, D. J. Cooperation and assortativity with dynamic partner updating. *Proceedings of the National Academy of Sciences* **109**, 14363–14368 (2012).
- [124] Haken, H., Peper, C. E., Beek, P. J. & Daffertshofer, A. A model for phase transitions in human hand movements during multifrequency tapping. *Physica D: Nonlinear Phenomena* **90**, 179–196 (1996).
- [125] Arnold, V. I. Small denominators. I. Mapping of the circumference onto itself. In Givental, A. B. *et al.* (eds.) *Collected Works*, vol. 2, 152–223 (Springer Berlin Heidelberg, Berlin, Heidelberg, 2009).
- [126] Jensen, O. & Colgin, L. L. Cross-frequency coupling between neuronal oscillations. *Trends in Cognitive Sciences* **11**, 267–269 (2007).
- [127] Lemke, J. L. Across the scales of time: artifacts, activities, and meanings in ecosocial systems. *Mind, Culture, and Activity* **7**, 273–290 (2000).
- [128] Nakagaki, T., Yamada, H. & Ueda, T. Interaction between cell shape and contraction pattern in the Physarum plasmodium. *Biophysical Chemistry* **84**, 195–204 (2000).
- [129] Buck, J. & Buck, E. Biology of synchronous flashing of fireflies. *Nature* **211**, 562–564 (1966).
- [130] Acebrón, J. A., Bonilla, L. L., Pérez Vicente, C. J., Ritort, F. & Spigler, R. The Kuramoto model: A simple paradigm for synchronization phenomena. *Reviews of Modern Physics* **77**, 137–185 (2005).

- [131] Breakspear, M., Heitmann, S. & Daffertshofer, A. Generative models of cortical oscillations: neurobiological implications of the Kuramoto model. *Frontiers in Human Neuroscience* **4**, 1–14 (2010).
- [132] Castellano, C., Fortunato, S. & Loreto, V. Statistical physics of social dynamics. *Reviews of Modern Physics* **81**, 591–646 (2009).
- [133] Marder, E. & Bucher, D. Central pattern generators and the control of rhythmic movements. *Current Biology* **11**, R986 – R996 (2001).
- [134] Schmidt, R. C. & Richardson, M. J. Dynamics of interpersonal coordination. In Fuchs, A. & Jirsa, V. K. (eds.) *Coordination: Neural, Behavioral and Social Dynamics*, vol. 2008, 281–308 (Springer Berlin Heidelberg, Berlin, Heidelberg, 2008).
- [135] Hoyt, D. F. & Taylor, C. R. Gait and the energetics of locomotion in horses. *Nature* **292**, 239–240 (1981).
- [136] Leonard, N. E. *et al.* Decision versus compromise for animal groups in motion. *Proceedings of the National Academy of Sciences* **109**, 227–232 (2012).
- [137] Acebrón, J. A., Bonilla, L. L., De Leo, S. & Spigler, R. Breaking the symmetry in bimodal frequency distributions of globally coupled oscillators. *Physical Review E* **57**, 5287–5290 (1998).
- [138] Tognoli, E. *EEG Coordination Dynamics: Neuromarkers of Social Coordination*, 309–323 (Springer Berlin Heidelberg, Berlin, Heidelberg, 2008).
- [139] Devaney, R. L. *An Introduction To Chaotic Dynamical Systems* (Westview Press, Boulder, Colorado, 2003), 2nd edn.
- [140] P. W. Anderson. More is different. *Science* **177**, 393–396 (1972).
- [141] Hong, H. & Strogatz, S. H. Kuramoto model of coupled oscillators with positive and negative coupling parameters: an example of conformist and contrarian oscillators. *Physical Review Letters* **106**, 054102 (2011).
- [142] Fuchs, A. & Kelso, J. A. S. A theoretical note on models of interlimb coordination. *Journal of Experimental Psychology: Human Perception and Performance* **20**, 1088–1097 (1994).
- [143] Laurent, M. & Kellershohn, N. Multistability: a major means of differentiation and evolution in biological systems. *Trends in Biochemical Sciences* **24**, 418–422 (1999).
- [144] Hansel, D., Mato, G. & Meunier, C. Clustering and slow switching in globally coupled phase oscillators. *Physical Review E* **48**, 3470–3477 (1993).

- [145] Daido, H. Order function and macroscopic mutual entrainment in uniformly coupled limit-cycle oscillators. *Progress of Theoretical Physics* **88**, 1213–1218 (1992).
- [146] Daido, H. Generic scaling at the onset of macroscopic mutual entrainment in limit-cycle oscillators with uniform all-to-all coupling. *Physical Review Letters* **73**, 760–763 (1994).
- [147] Crawford, J. D. & Davies, K. T. R. Synchronization of globally-coupled phase oscillators: singularities and scaling for general couplings. *Physica D: Nonlinear Phenomena* **125**, 62 (1999).
- [148] Chialvo, D. R. Emergent complex neural dynamics. *Nature Physics* **6**, 744 (2010).
- [149] Friston, K. J. Transients, metastability, and neuronal dynamics. *NeuroImage* **5**, 164 – 171 (1997).
- [150] Ashwin, P., Orosz, G., Wordsworth, J. & Townley, S. Dynamics on networks of cluster states for globally coupled phase oscillators. *SIAM Journal on Applied Dynamical Systems* **6**, 728–758 (2007).
- [151] Rabinovich, M. I., Huerta, R., Varona, P. & Afraimovich, V. S. Transient cognitive dynamics, metastability, and decision making. *PLoS Computational Biology* **4**, e1000072 (2008).
- [152] Jirsa, V. K., Stacey, W. C., Quilichini, P. P., Ivanov, A. I. & Bernard, C. On the nature of seizure dynamics. *Brain* **137**, 2210–2230 (2014).
- [153] Tang, E. *et al.* Developmental increases in white matter network controllability support a growing diversity of brain dynamics. *Nature Communications* **8**, 1252 (2017).
- [154] Nordham, C. A., Tognoli, E., Fuchs, A. & Kelso, J. A. S. How interpersonal coordination affects individual behavior (and vice versa): experimental analysis and adaptive HKB model of social memory. *Ecological Psychology* **7413**, 1–26 (2018).
- [155] W. Bowman, A. & Azzalini, A. Applied smoothing techniques for data analysis. 31 (Oxford University Press, New York, 1997).
- [156] Hogg, R. V. Statistical robustness: One view of its use in applications today. *American Statistician* **33**, 108–115 (1979).
- [157] Eckmann, J.-P., Kamphorst, S. O. & Ruelle, D. Recurrence plots of dynamical systems. *EPL (Europhysics Letters)* **4**, 973 (1987).
- [158] Marwan, N., Carmen Romano, M., Thiel, M. & Kurths, J. Recurrence plots for the analysis of complex systems. *Physics Reports* **438**, 237–329 (2007).

- [159] Winfree, A. T. Biological rhythms and the behavior of populations of coupled oscillators. *Journal of Theoretical Biology* **16**, 15–42 (1967). 335.
- [160] Lundgren, J. Splinefit (2017). URL <https://www.mathworks.com/matlabcentral/fileexchange/13812-splinefit>.
- [161] Hatcher, A. *Algebraic Topology* (Cambridge University Press, Cambridge, United Kingdom, 2001).
- [162] Zomorodian, A. & Carlsson, G. Computing persistent homology. *Discrete & Computational Geometry* **33**, 249–274 (2005).
- [163] Carlsson, G. Topology and data. *Bulletin of the American Mathematical Society* **46**, 255–308 (2009).
- [164] Mischaikow, K. & Nanda, V. Morse theory for filtrations and efficient computation of persistent homology. *Discrete & Computational Geometry* **50**, 330–353 (2013).
- [165] Edelsbrunner, H., Letscher, D. & Zomorodian, A. Topological persistence and simplification. *Discrete and Computational Geometry* **28**, 511–533 (2002).
- [166] Kimchi, R. Primacy of wholistic processing and global local paradigm - a critical-review. *Psychological Bulletin* **112**, 24–38 (1992).
- [167] Hausmann, J.-C. On the Vietoris-Rips complexes and a cohomology theory for metric spaces. *Prospects in Topology: Proceedings of a Conference in Honor of William Browder*. **138**, 175–188 (1995).
- [168] Borsuk, K. On the imbedding of systems of compacta in simplicial complexes. *Fundamenta Mathematicae* **35**, 217–234 (1948).
- [169] Ghrist, R. Barcodes: The persistent topology of data. *Bulletin of the American Mathematical Society* **45**, 61–76 (2007).
- [170] Nanda, V. Perseus, the persistent homology software, accessed 11/25/2017 (2017). URL <http://www.sas.upenn.edu/~vnanda/perseus>.
- [171] Bubenik, P. & Dłotko, P. A persistence landscapes toolbox for topological statistics. *Journal of Symbolic Computation* **78**, 91–114 (2017).
- [172] Bubenik, P. Statistical topological data analysis using persistence landscapes. *Journal of Machine Learning Research* **16**, 77–102 (2015).
- [173] Thom, R. *Structural Stability and Morphogenesis: An Outline of a General Theory of Models* (W. A. Benjamin, Reading, Massachusetts, 1975).
- [174] Oltvai, Z. N. & Barabási, A.-L. Life’s complexity pyramid. *Science* **298**, 763–764 (2002).

- [175] Vespignani, A. Modelling dynamical processes in complex socio-technical systems. *Nature Physics* **8**, 32–39 (2012).
- [176] Aguilera, M. Rhythms of the collective brain: metastable synchronization and cross-scale interactions in connected multitudes. *Complexity* **2018**, 1–9 (2018).
- [177] Chan, J. M., Carlsson, G. & Rabadian, R. Topology of viral evolution. *Proceedings of the National Academy of Sciences* **110**, 18566–18571 (2013).
- [178] Yao, Y. *et al.* Topological methods for exploring low-density states in biomolecular folding pathways. *The Journal of Chemical Physics* **130**, 144115 (2009).
- [179] Curto, C. & Itskov, V. Cell groups reveal structure of stimulus space. *PLoS Computational Biology* **4**, e1000205 (2008).
- [180] Dabaghian, Y., Mémoli, F., Frank, L. & Carlsson, G. A topological paradigm for hippocampal spatial map formation using persistent homology. *PLoS Computational Biology* **8**, e1002581 (2012).
- [181] Petri, G. *et al.* Homological scaffolds of brain functional networks. *Journal of The Royal Society Interface* **11**, 20140873–20140873 (2014).
- [182] Saggar, M. *et al.* Towards a new approach to reveal dynamical organization of the brain using topological data analysis. *Nature Communications* **9**, 1399 (2018).
- [183] Giusti, C., Ghrist, R. & Bassett, D. S. Two's company, three (or more) is a simplex. *Journal of Computational Neuroscience* **41**, 1–14 (2016).
- [184] Kramár, M. *et al.* Analysis of Kolmogorov flow and Rayleigh-Bénard convection using persistent homology. *Physica D: Nonlinear Phenomena* **334**, 82–98 (2016).
- [185] Donato, I. *et al.* Persistent homology analysis of phase transitions. *Physical Review E* **93**, 052138 (2016).
- [186] Nicolis, G. & Prigogine, I. *Exploring Complexity* (W.H. Freeman & Company, New York, 1989), first edn.
- [187] Holland, J. H. *Hidden Order: How Adaptation Builds Complexity*. (Perseus Books Group, New York, 1996).
- [188] Bertuglia, C. S. & Vaio, F. *Nonlinearity, Chaos, and Complexity* (Oxford University Press, New York, 2005).
- [189] Semon, R. W. *The Mneme* (Macmillan, New York, 1921).
- [190] Cragg, B. G. & Temperley, H. N. V. Memory : the analogy with ferromagnetic hysteresis. *Brain* **78**, 304–316 (1955).

- [191] Wilson, H. R. & Cowan, J. D. Excitatory and inhibitory interactions in localized populations of model neurons. *Biophysical Journal* **12**, 1–24 (1972).
- [192] Zipser, D., Kehoe, B., Littlewort, G. & Fuster, J. A spiking network model of short-term active memory. *The Journal of neuroscience* **13**, 3406–3420 (1993).
- [193] Canavier, C. C., Baxter, D. a., Clark, J. W. & Byrne, J. H. Nonlinear dynamics in a model neuron provide a novel mechanism for transient synaptic inputs to produce long-term alterations of postsynaptic activity. *Journal of neurophysiology* **69**, 2252–7 (1993).
- [194] Foss, J., Longtin, A., Mensour, B. & Milton, J. Multistability and delayed recurrent loops. *Physical Review Letters* **76**, 708–711 (1996).
- [195] Barnes, C. A., Suster, M. S., Shen, J. & McNaughton, B. L. Multistability of cognitive maps in the hippocampus of old rats. *Nature* **388**, 272–275 (1997).
- [196] Xiong, W., Ferrell, J. E. J. & Ferrell Jr, J. E. A positive-feedback-based bistable ‘memory module’ that governs a cell fate decision. *Nature* **426**, 460 (2003).
- [197] Daido, H. Scaling behaviour at the onset of mutual entrainment in a population of interacting oscillators. *Journal of Physics A: Mathematical and General* **20**, 629–636 (1987).
- [198] Farber, M. Topological complexity of motion planning. *Discrete and Computational Geometry* **29**, 211–221 (2003).
- [199] Holland, J. H. *Adaptation in Natural and Artificial Systems* (MIT Press, Cambridge, Massachusetts, 1992).
- [200] Wagner, G. P. Homologues, natural kinds and the evolution of modularity. *American Zoologist* **36**, 36–43 (1996).
- [201] Alon, U. Biological network: the tinkerer as an engineer. *Science* **301**, 1866–1867 (2003).
- [202] Kashtan, N. & Alon, U. Spontaneous evolution of modularity and network motifs. *Proceedings of the National Academy of Sciences* **102**, 13773–13778 (2005).
- [203] Espinosa-Soto, C. & Wagner, A. Specialization can drive the evolution of modularity. *PLoS Computational Biology* **6**, e1000719 (2010).
- [204] Holland, J. H. *Signals and Boundaries* (MIT Press, Cambridge, Massachusetts, 2012).
- [205] Yamashita, Y. & Tani, J. Emergence of functional hierarchy in a multiple timescale neural network model: A humanoid robot experiment. *PLoS Computational Biology* **4**, e1000220 (2008).
- [206] Payzant, G. *Glenn Gould Music and Mind* (Key Porter Books, 2005).